TÉCNICO LISBOA

# Development of a hybrid-electric propulsive system model for Unmanned Aerial Systems

**David Pfurtscheller**

Thesis to obtain the Master of Science Degree in

## Aerospace Engineering

Supervisors: Prof. Afzal Suleman
Dr. Frederico José Prata Rente Reis Afonso

### Examination Committee

Chairperson: Prof. Fernando José Parracho Lau
Advisor: Prof. Afzal Suleman
Members of the Committee: Dr. José Lobo do Vale

**November 2019**

# Acknowledgments

I would like to thank my parents for their friendship, encouragement and caring over all these years, for always being there for me through thick and thin and without whom this project would not be possible. I would also like to thank my grandparents, aunts, uncles and cousins for their understanding and support throughout all these years.

I would also like to acknowledge my dissertation supervisors Prof. Dr. Suleman and Dr. Afonso for their insight, support and sharing of knowledge that has made this Thesis possible.

Last but not least, to all my friends and colleagues that helped me grow as a person and were always there for me during the good and bad times in my life. Thank you.

To each and every one of you – Thank you.

# Abstract

The growing economic and environmental pressure on aviation applications worldwide demand for innovative concepts to decrease the emission footprint of future aviation vehicles while increasing the performance. Since the beginning of the $21^{st}$ century the research efforts by various public aeronautical agencies and private companies has significantly increased. In this process hybrid-electric propulsion, distributed propulsion and novel aircraft concepts have emerged as technologies with a high potential to fulfil these requirements.

In the aviation sector these concepts are relatively new and therefore the knowledge towards these technologies needs to be deepened to maximize their performance. The hybrid-electric concept is going to be explored in depth with the development of a numerical simulation model in MATLAB for an Unmanned aerial vehicle propulsion system. The components are modeled with analytical and surrogate modeling techniques. Afterwards a validation of the models with experimental data is performed and models with high accuracy are obtained. The propulsion module is managed by a rule-based controller with five operating modes. Furthermore it is equipped with the Ideal Operating Line energy management strategy to maximize the fuel efficiency of the aircraft. The advantages and disadvantages of the hybrid-system are explored in a surveillance mission analysis with the research aircraft QT1 for various propulsion system configurations.

# Keywords

Hybrid-electric propulsion, Unmanned Aerial Systems, Parallel Hybrid System, Ideal Operating Line, Surrogate Model

# Resumo

A crescente pressão económica e ambiental na utilização da aviação a nível mundial exigem conceitos inovadores para diminuir a emissão da pegada ecológica em futuros modelos de aviação enquanto que o desempenho é aumentado. Desde o começo do século XXI, houve um esforço significativo na pesquisa por parte de várias agências aeronáuticas públicas e empresas privadas.Nesse processo a propulsão híbrida-elétrica, propulsão distribuída e novos conceitos de aeronaves emergem como tecnologias com um elevado potencial de cumprir esses requisitos.

No setor da aviação, esses conceitos são relativamente recentes, pelo que o conhecimento sobre essas tecnologias necessita de ser aprofundado de forma a maximizar o seu desempenho. O conceito elétrico-híbrido será explorado em profundidade com o desenvolvimento de um modelo de simulador numérica no MATLAB para um sistema de propulsão de veículo aéreo não tripulado. Os componentes são modelados com base em técnicas de modelos analíticos e modelos de substituição. Posteriormente, é efectuada uma validação dos modelos com dados experimentais e modelos com maior precisão são obtidos. O módulo de propulsão é dirigido por um controlador baseado em regras, com cinco modos operacionais. Para além disso, está equipado com a estratégia de gerenciamento de energia da Linha Operacional Ideal, de modo a maximizar a eficácia do combustível da aeronave. As vantagens e desvantagens do sistema híbrido são exploradas em uma análise de missão de vigilância com a aeronave QT1 para várias configurações do sistema de propulsão.

# Palavras Chave

propulsão híbrida-eléctrica, véıculos aéreos não tripulados, sistema híbrido em paralelo, Linha de operação ideal, *Surrogate Model*

# Contents

# List of Figures

# List of Tables

# Listings

# Nomenclature

| | |
|---|---|
| $\beta$ | exponential Capacity Coefficient |
| $C_T$ | Thrust Coefficient |
| $C_P$ | Power Coefficient |
| $C_f$ | Correction Coefficient |
| $\rho$ | Density |
| $D$ | Diameter |
| $e$ | CV-Error |
| $rpm$ | Revolutions per Minute |
| $n$ | Revolutions per Second |
| $w$ | Rotational Speed |
| $P$ | Power |
| $T$ | Torque |
| $\mu$ | Efficiency |
| $V$ | Voltage |
| $V_0$ | constant Battery Voltage |
| $K$ | Polatrity Voltage |
| $Q$ | maximum Capacity |
| $I_n$ | nominal Battery Current |
| $I_m$ | internal Resistance Current |
| $I_t$ | Battery Current in timestep |
| $I_0$ | no load Current |
| $K_V$ | rpm proportionality Constant |
| $R_m$ | internal Resistance |
| $U_{emf}$ | Electric Motor Force Voltage |
| $U_m$ | Voltage internal Resistance |
| $p$ | Pressure |

# Acronyms

| | |
|---|---|
| **BEMT** | Blade Element Momemtum Theory |
| **BH** | Biharmonic |
| **BLI** | Boundary Layer Injection |
| **BSFC** | Brake Specific Fuel Consumption |
| **BWB** | Blended Wing Body |
| **CfAR** | Center of Aerospace Research |
| **CV** | Cross Validation |
| **DMFC** | Direct Methanol Fuel Cell |
| **EM** | Electric Motor |
| **EMF** | Electric Motoric Force |
| **ESC** | Electronic-Speed-Controller |
| **FDR** | Flight Data Recording |
| **G** | Gaussian |
| **HEPS** | Hybrid-Electric Propulsion System |
| **ICE** | Internal Combustion Engine |
| **IMQ** | Inverse-Multiquadratic |
| **IOL** | Ideal Operating Line |
| **Life** | Lithium Iron |
| **Li-Ion** | Lithium Ion |
| **Li-Po** | Lithium Polymer |
| **Li-S** | Lithium Sulfur |
| **MEA** | More Electric Aircraft |
| **MQ** | Multiquadratic |
| **Ni-Cd** | Nickel Cadmium |
| **Ni-MH** | Metal hybride |
| **PAN** | Polyacrylonitrile |
| **PEMFC** | Polymer Electrolyte Membrane Fuel Cell |
| **RBF** | Radial Basis Function |
| **RMSE** | Root Mean Squared Error |
| **SOFC** | Solid-Oxide Fuel Cell |
| **SUGAR** | Subsonic Ultra Green Aircraft Research |
| **TEG** | Thermoelectric Generator |
| **TMS** | Thermal Management systems |
| **TPS** | Thin-Plate-Spline |
| **UAV** | Unmanned Aerial Vehicles |

# 1

# Introduction

## Contents

## 1.1 Motivation

The awareness of the worldwide threats for societies due to greenhouse warning is bigger than ever before. Thus the political sector and society itself increase pressure to reduce the carbon footprint of mankind. The connection between emissions and global warming has been comprehensively assessed in 1999 [1]. The most critical gases which are emitted in flight are carbon-dioxide $CO_2$ and nitrogen oxide $NO_x$. In the year the 2000 roughly 677 teragram[1] of $CO_2$ were emitted by the aviation sector worldwide, which equals to 2-3% of all $CO_2$ emission made by humans. Till the year 2050 an increase by the factor of 3.6 is expected. This gas has not only the biggest radiative forcing of all emissions but also the longest atmospheric lifetime from at least decades up to millennias in the worst case. Because of this $CO_2$ is considered to be the most important contribution to climate change. The reactive nitrogen oxide is also considered to have a significant impact on global warming because it acts as catalyst to produce ozone $O_3$ at cruise altitudes. In this height nitrogen oxide is more efficient in the ozone production than on the earth surface. [2]

Besides the impact on the environment in 2014 a study from the MIT came to the conclusion of $\approx 16000$ premature deaths worldwide associated with air-travel emissions. [3] This approximation is based on the number of flights for the year 2010 presented in [2]. Not only is this death-toll not acceptable but also the associated health costs of aviation emissions were estimated to be at the same order of magnitude than the climate costs for discount rates of 2% and 3% making the impact in this field also significant. The particles $PM_{2.5}$, which are particles with an aerodynamic diameter smaller than 2.5 $\mu$m, are linked to 87% of all deaths. [3] It was proven that $PM_{2.5}$ is linked to lung cancer as well as both cardiovascular and respiratory (cardiopulmonary) disease. [4] [5] These impacts on the planet and health can also be combined with economical motivation of airlines. In the airline operating cost break-down the fuel costs make up roughly 30% of all expenses. [6] The number of passengers worldwide is expected to double from 2017 to the year 2034. [7] In order to satisfy this high demand the number of planes also has to increase significantly as shown in figure 1.1. The fleet prediction data is based on the 2019 market outlook of the two biggest aircraft manufacturers AIRBUS and BOEING with deviations of only $\approx 5\%$. [8] [9] Due to this data the airlines have to purchase roughly 40000 new airplanes up to the year 2038. The significant fraction of fuel costs, the environmental and health issues and the higher number of flights demand more fuel efficient aircraft concepts.

The performance goals agreed on by NASA for mid-term (2025-2035) and far-term (beyond 2035) aircraft designs which are presented in table 1.2 reflect those necessary upgrades. The concepts are expected to show significant improvements regarding noise, NOx emissions and better fuel efficiency by large numbers compared to the best aircraft of each class from the year 2005. In order to meet these goals drastic changes to aircraft propulsion systems and airframe systems are needed. Especially the

[1] 1 teragram = $10^6$ tons

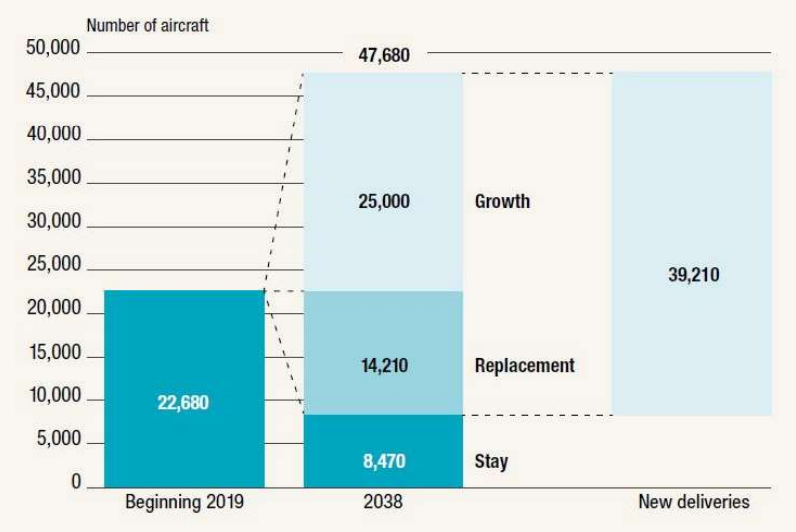


**Figure 1.1:** Evolution of the passenger airplane fleet [8]

electrification of future aviation is expected to unleash big potential not only for the propulsion system but also for an increased design flexibility. [10]

| TECHNOLOGY BENEFITS | TECHNOLOGY GENERATIONS (Technology Readiness Level = 5-6) | | |
|---|---|---|---|
| | Near-term 2015-2025 | Mid-term 2025-2035 | Far-term Beyond 2035 |
| Noise (cumulative below Stage 4) | 22 - 32 dB | 32 - 42 dB | 42 - 52 dB |
| LTO $NO_x$ Emissions (below CAEP 6) | 70 - 75% | 80% | >80% |
| Cruise $NO_x$ Emissions (relative to 2005 best in class) | 65 - 70% | 80% | >80% |
| Aircraft Fuel/Energy Consumption (relative to 2005 best in class) | 40 - 50% | 50 - 60% | 60 - 80% |

**Figure 1.2:** NASA Targeted Improvements in Subsonic Transport System-level Metrics [7]

## 1.2 Objective

The impacts on the environment and human health as well as the economical aspect of airline operations demands performance increased aircraft. Several technologies and concepts which have the potential to achieve those goals are being surveyed in this work. This research effort includes distributed propul-

sion technology, novel airframe configurations and hybrid-electric propulsion for enviromental friendly airtravel. The implementation of novel solutions demands for stepping stones before employing the technology in commercial aviation. Therefore, Unmanned Aerial Vehicles (UAV) are well suited for the first application tests. Due to recent developments and the identified potential during the technology survey the hybridization of aircraft is chosen in this work to be analyzed in detail. Different concepts regarding the architecture of the propulsive system have been proposed by various projects. In this thesis the numerical model of a parallel hybrid propulsion system for a UAV is going to be implemented and validated with experimental data. The powertrain includes computational models for the battery, the engine, the electric motor, the speed controller and the propeller. Afterwards the single models are composed to portray a parallel hybrid propulsion system with an energy management and control strategy. This powertrain system is integrated into an airframe simulation model to perform a mission analysis. Therefore, the efficiency gain can be validated in between different propulsion systems.

## 1.3 Thesis Outline

In **Chapter 1** the thesis motivation of eco-friendly aviation is outlined. Further, the necessary steps to successfully achieve the objective are described.
Afterwards in **Chapter 2** a broad technology spectrum to improve the efficiency of air-travel is gathered and described. This includes solutions from various companies and institutions worldwide.
In **Chapter 3** numerical models are implemented with MATLAB and validated for the various single components of a hybrid-electric propulsion system. Later the component models are integrated into a parallel hybrid-electric propulsion test bench simulation model.
**Chapter 4** represents the integration of the propulsion components into a full UAV propulsion system model including an energy management strategy and control for a parallel hybrid-electric propulsion system.
This propulsion system is extended with airframe characteristics in **Chapter 5** and a full mission analysis of the various propulsion system architectures is performed.
In **Chapter 6** the conclusions of the thesis are stated and potential for future research efforts are outlined.

# 2

# Literature Review

## Contents

The performance goals defined in chapter 1 are milestones in achieving an all electrical commercial aircraft. But due to the high power demand and necessary future developments in various fields these concepts will not be able to enter the market before 2035, considering an optimistic development process, according to [11]. In this chapter an overview of technologies with the potential to fulfill these goals is given. The author has identified the area of hybrid-electric propulsion systems, novel airframe configurations and distributed propulsion as promising research areas to achieve a more sustainable aviation concept. First the hybrid-electric propulsion technology in various architectures and the new challenges regarding power sources, electrical system and thermal management system are outlined. Afterwards, concepts to increase the performance of the system even further like energy harvesting and distributed propulsion are presented. In the last section of the chapter novel airframe configurations and the fuel cell approach are described as an alternative or compelling solution to the previously mentioned technologies. The implementation in small scale systems like UAVs will provide a good stepping stone to increase the performance of those technologies due to the system's simplicity. This work therefore focuses on the performance gain for UAV applications.

## 2.1 Hybrid-Electric Propulsion

The concept of hybrid propulsion systems consists of conventional combustion engines as well as electric motors to power the aircraft and shows great potential for future aviation. This approach also opens up possibilities to implement technologies like distributed propulsion, which are described in sub-section 2.2.2. The different hybrid propulsive system architectures are a serial-, parallel-, power-split- or turbo-electric configuration. The functional schemes of these types are presented in figure 3.1. The powertrain consists of an internal combustion engine (ICE), an electric motor (EM), batteries, motor controller, possibly a mechanical clutch or generator and propellers. [12]. Because these concepts include batteries as an extra weight component the widely spread and proven fuel-fraction method by [13] is not applicable anymore. New methodologies presented by the Politecnico di Milano and the University of Applied Sciences Aachen in [14] and [15] respectively offer preliminary sizing approaches for a small hybrid electric aircraft which could also be applied for large UAVs.

### 2.1.1 Parallel Hybrid Propulsion

The functional scheme of the parallel hybrid propulsion system is presented in figure 2.1a. The higher control complexity of this configuration, due to the need of a mechanical coupling device, compared to the serial system presented in figure 2.1b is obvious. The ICE is directly connected to the propeller in parallel configurations and therefore the ICE could potentially not operate at its most efficient point. To solve this problem a CVT can be introduced, which however brings more difficulty to the control

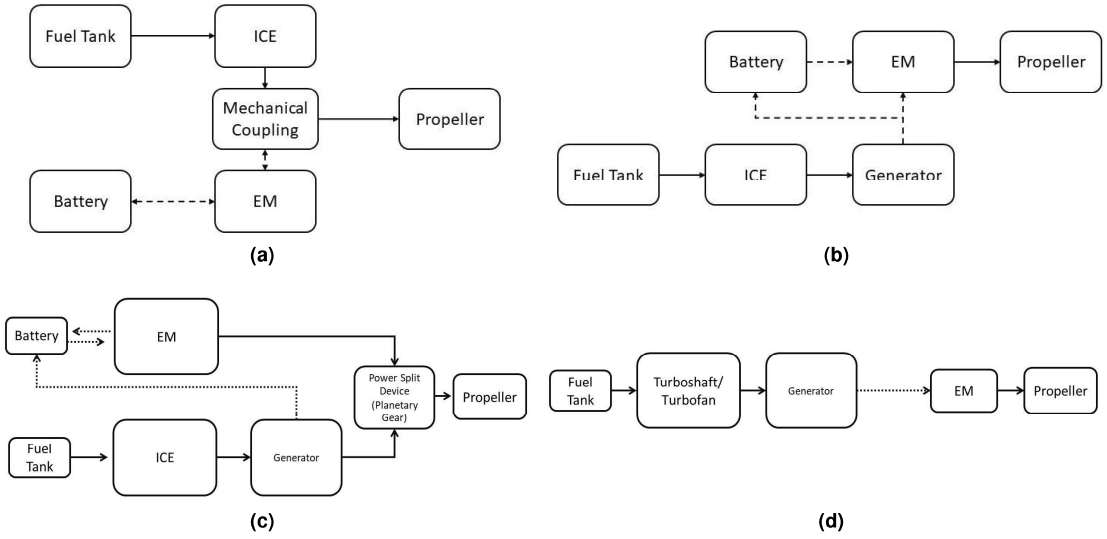


**Figure 2.1:** Functional Scheme for: (a) Parallel Hybrid System (adapted from [16]), (b) Serial Hybrid System (adapted from [16]), (c) Power-Split Hybrid System (adapted from [17]) and (d) Turobelectric Hybrid System (adapted from [18])

strategy. [19] These extra components allow the propeller to be either driven by the ICE alone, the EM alone or both at the same time. Therefore, the EM can also be used as a generator when the ICE drives the propeller and the batteries can be recharged. These different operational modes are thus available to be chosen according to the mission requirements. Further, advantages are the smaller sized ICE and EM as they can operate together and these two components also offer a redundancy which is important in civil and military applications. The disadvantages are the extra mass due to the clutch and the more sophisticated propulsion system control [20]. Still a study by the University of Victoria in British Columbia has found that parallel structures are around 8% lighter than its series counterpart due to the lack of a generator. [16]

The Univeristy of California implemented a parallel hybrid-electric propulsion system (HEPS) in a small UAV and was able to obtain simulation results with significant energy savings when compared to a conventional 4-stroke gasoline powered UAV. [21] Further, parallel systems were implemented also by the University of Colorado [22], the Embry-Riddle´s Eco-Eagle project [23] and are widespread in the hybrid car market. [17]

### 2.1.2 Serial Hybrid Propulsion

The structure of the serial hybrid propulsion system is shown in figure 2.1b. In this configuration the energy is stored in the fuel first which then is converted to mechanical energy in the ICE. In the next step the generator converts this energy into electricity, which then powers the battery. At last the EM again

converts the electricity to torque for the propeller. The efficiency of series hybrid systems is comparably low due to three three energy conversion steps involved in the powertrain. [16] Furthermore, because the EM is directly connected to the propeller and the only power source this component needs to be sized according to the maximum power demand and is therefore going to be heavy. Also this architecture needs a generator to convert the energy stored in the fuel to electric energy for the EM. This introduces a weight penalty onto the system which has a large impact especially on small UAVs. [20] Advantages of this configuration include the more easy control of such systems compared to a parallel hybrid propulsion system. To operate in electric only mode is fairly easy from the control side as no complex uncoupling of the ICE from the powertrain is necessary. Moreover the propeller is not coupled to the ICE as well the therefore the ICE can operate permanently at its optimal efficiency.
Due to the weight penalty and power conversion losses the series hybrid configuration is therefore not suitable for Micro and nano-Air Vehicles as shown in [24] and [25]. While for UAVs this configuration seems not to be suitable SIEMENS AG, Diamond Aircraft and EADS developed the DA36 E-Star motor glider with a serial HEPS and presented it in 2011. According to the project it was possible to cut emissions and fuel consumption by 25% with the HEPS. [26] Further aerial vehicles with a serial-hybrid propulsion in development currently include the AIRBUS E-FAN, XTI Tri-Fan 600 and the Zum Um. [23]

### 2.1.3 Power-split

The Power-Split or Series-parallel Hybrid configuration, presented in figure 2.1c, employs a planetary gear to transfer the power generated by the ICE and/or the EM to the propeller. Therefore, no direct connection between the powerplants and the mechanical drivetrain exists. The planetary gear enables the configuration to save more fuel because it combines the various power sources more efficient. [17] While providing this advantage the planetary gear also increases the complexity of the design and control at the same time. This system is being implemented in hybrid cars but no known UAV employs it due to the strict weight constraints. [20]

### 2.1.4 Turboelectric Propulsion

The Turboelecctric propulsion technology in contrast to the other presented hybrid propulsion concepts, does not rely on batteries as energy storage. Instead a turboshaft/turbofan is employed to drive the electric generator(s), which then power(s) the individual electric motors as shown in figure 2.1d. This concept exist as a partial (turbofan) or fully (turboshaft/ICE) turboelectric configuration. While in the fully turboelectric version the total thrust is provided by electric propulsion in the partial version a gas turbine driven turbofan is used to provide extra thrust. As in the serial hybrid configuration the engine's and the propeller's rotational speed are decoupled and therefore both components can be operated at their

optimal speeds. [27] This configuration is especially studied for large regional N+3/N+4[1] concepts like the NASA N3X and ESAero. Due to the high power demand of these aircraft further investment into the design and cooling mechanism of the electric components is highly important. [30]

### 2.1.5 Rechargeable Battery Technology

The concept of hybrid-electric propulsion systems in particular and the goal of energy sustainable aviation in general increases the demand for new energy storage concepts. The high specific energy density of conventional gasoline of about 13000 Wh/kg is a big challenge for replacement technologies. In UAV applications rechargeable batteries and fuel cells, outlined in sub-section 2.3.2, are the most employed technologies. A comprehensive review of various energy storage concepts like compressed air energy storage, superconducting magnetic energy storage, hyrdogen energy storage and thermal energy storage is given in [31]. The evaluation of the energy source for future aviation is based on key parameters such as energy density, energy per unit volume, and specific energy as well as energy per unit mass. [32] The battery stores energy in chemical form and then uses a chemical reaction to convert it to electric energy. [31] The most widely spread Lithium based battery types are summarized in table 2.1. These batteries can be geometrically designed and scaled according to the requirement. Besides the Lithium technology also batteries based on Nickel Metal hybride (Ni-MH), Nickel Cadmium (Ni-Cd) and Alkaline exist. These technologies present a lower energy density and are therefore not relevant for aeronautic applications. So far the Lithium Polymer (Li-Po) was the most interesting type, due to the high energy density and low weight (see table 2.1), especially for applications with weight restraints as is the case in UAVs. The application of the Lio-ion and Li-Po batteries shows achievable energy densities between 522 - 864 kJ/Kg (145 - 240 Wh/kg). But these values are still two orders of magnitude lower than typical hydrocarbon fuels  43MJ/kg (13000 Wh/kg). [32] In the mid 90s the development of Lithium Sulfur batteries (Li-S) started. The theoretical specific energy value for this type is 2600 Wh/kg. This assumes a total reaction between the Lithium and Sulfur to obtain $Li_2S$. [32] A specific energy between 1800 - 2160 kJ/kg (500 - 600Wh/kg) should be achievable. But so far only a value of 1260kJ/kg (250 Wh/kg) was demonstrated in the Zephyr 7 in 2010. [33]

| Battery technology | Energy Density |
|---|---|
| Lithium Polymer (LiPo) | 250 - 730 Wh/L |
| Lithium Ions (Li-Ion) | 250 - 676 Wh/L |
| Lithium Iron (Life) | 220 Wh/L |
| Lithium Sulfur (Li-S) | 2600 Wh/kg |

**Table 2.1:** Available battery technology adapted from [32](approximation). Accurate conversion is not possible due to unknown amount of Lithium and Polymer in battery

[1] The *N+* abbreviation stand for a generation of aircraft in the future (these definitions are valid for the data the thesis is written) N+3: production start $\approx 2035$ [28];N+4: production start $\approx 2040$ [29]

| Battery technology | Energy Density |
|---|---|
| Lithium Air | 1700 Wh/kg (expected) |
| Metal Air | 110 - 420 Wh/kg |
| Sodium Sulfur | 150 - 240 Wh/kg |

**Table 2.2:** Future energy storage concepts

The research activity in the field of advanced battery technology is very high due to a demand across various industries. Therefore, different types of energy storage systems are explored. A brief summary of the most promising technologies is presented in table 2.2. Possible technologies include the metal Air and the sodium sulfur based systems. But all these concepts have not yet exceeded the specific energy of Lithium based batteries. [34] However in the last ten years the Lithium-Air technology started emerging and showing great potential in the battery market. Theoretically the specific energy of such a battery is 11600 Wh/kg and therefore very close to the value of gasoline 13000 Wh/Kg. But the practical value for Lithium-Air based batteries will be far less. The average tank-to-wheel ratio for the US-fleet is around 12.6%, which leads to an effective specific energy of 1700Wh/Kg. In order to achieve this value for Lithium-Air based batteries only 14.5% of the theoretical value is necessary. Through further research this values is assumed to be achievable in the near future. [35]
Additionally to the specific weight of the batteries further aspects need to be considered when sizing the component. In order to account for the weight of the battery structure and the management system a weight penalty of 30% is imposed on the specific power. Further, the maximum discharge rate to not decrease battery life significantly is 90%. These factors will increase the battery weight. [36]

### 2.1.6 Electrical System

In future concepts employing HEP or fully turboelectric systems the electrical architecture decision will be strongly coupled with performance, weight and flight safety. The energy storage, generator, rectifier, motor, inverter, bus, motor controller and fault current limiter are the key elements of electric propulsion systems. The electric power demand for future aviation concepts will significantly vary according to the assigned task. While very high power applications like the NASA N3-X (300 passengers) are estimated to use around 5MW, concepts for smaller aircraft with only around 150 passengers like the NASA STARC-ABL the power requirement will be situated in the megawatt class. This difference will lead to a significant different structure of the electrical system. In the following section a brief characteristics of the key design considerations will be given. [23]
Motors and generators can be summarized as electrical machines because they have the same general principle. For this component synchronous and asynchronous machines exist which both can employ either an alternating or direct current. The power-to-weight ratio of electrical machines for the year 2030 can be approximated to be in between 10 to 15 kW/kg with an efficiency of 96%. This value is justi-

fied based on research targets by Airbus and NASA. [37] [36]. Also electric machines with a power to weight ratio of 22kW/kg were partially tested by Electrodynamics. [30] A ratio of 5.2 kW/kg was already achieved in a SIEMENS project for a one person airplane. [38].

The high power demand of heavy duty applications will lead to significant thermo-management problems due the high amount of waste heat. Therefore, superconducting architectures are considered for applications like the NASA N3-X while conventional conductors are prioritized for applications around 1MW or less. [39] Superconducting materials show zero resistance at low operating temperatures (30-60K) and therefore increase efficiency. [23] High power generators based on a superconducting field and conventional armature were already tested by few companies but no fully superconducting machine has ever been implemented due to alternating current losses and the high cost of superconducting material. [40] Furthermore, the cooling requirement to operate a superconductivity machine is immense. [23]

In the distribution buses the choice for either an alternating or direct current has to be made. The literature currently favors DC power distribution especially if batteries are involved but also for turboelectric power systems. Even tough DC distribution suffers significant losses due the necessary alternating to direct current conversion in both ends they have the advantage of eliminating the synchronization of the phases of multiple generators and motors. The electrical system has a higher efficiency for higher voltages but a weight and safety penalty due the risk of electrical arcing at high altitude needs to be considered. The Paschens Law states that an air gap insulation is safe under 327V. Because electrical propulsion concepts are forecasted to need a low kilo volt range new lightweight insulasive materials are necessary. [23] The electrical system and components of the NASA NX-3 project are very interesting for future aerial vehicles considerations, due to the advanced state of their research concept regarding the electrical components of future aviation, and are presented in [40].

### 2.1.7 Thermal Management Systems

As summarized in the previous sections the electrification of aircraft is the key development to meet the performance and emission goals of future aviation. Therefore, the electrical architecture is strongly coupled with weight and performance characteristics. Regarding the propulsion systems the impact is going to be the biggest. [23] Due to the large power-demand of all electric or hybrid electric commercial planes the generated waste heat of electric propulsion systems is significant. In most state of the art aviation vehicles the turbine exhales nearly all waste heat into the atmosphere opposite to future aircraft concepts where the EMs are located inside the airplane. This can lead to system failures due to high temperatures. The result of recent studies leads to the conclusion that a half-megawatt motor can produce as much heat as a barbecue ($\approx 27.5kW$). [41]

This waste heat is generated mainly by the electrical components of the propulsive system. [23] Therefore, a sufficient cooling system needs to be developed. The Thermal Management system (TMS) for an

airplane presented in figure 2.2 consists out of coolant, ducts, coolant pumps, reservoirs and radiators. The NASAs project X-57 TMS weight for example is estimated to be around 5% of the total electronics including the batteries. [36] A strong coupling between the propulsive system and TMS exists. The weight of the TMS will increase the overall weight of the aircraft and therefore increase drag. The design process should focus on increasing the efficiencies closer to the propulsor as this could reduce the size of the other components. Generally the parts can be either air-cooled or liquid cooled. The liquid version shows higher power and torque densities on the other hand this method also needs extra components like pumps. [41]

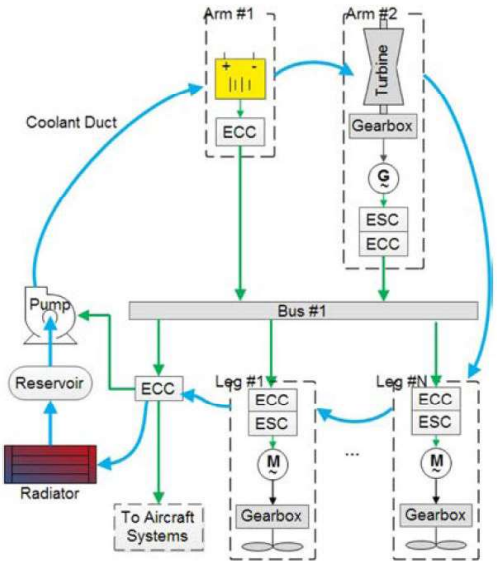


**Figure 2.2:** TMS and propulsive system architecture coupled [41]

In order to decrease the cooling drag of the radiators, ducted versions can be used as already described in the 1930s in [42]. Potentially well-designed versions could even provide a positive net thrust. [43] Additionally to the cooling process the management of the excess heat could provide opportunities as well. Some of this heat could be redistributed through the aircraft to supply anti-icing, cabin heating, battery temperature control and pre-heating fuel. The most critical phase for the TMS is the time-frame of the highest power demand on the electric components which is likely to occur during "Take-off" and early climb stages. A framework for the sizing of a TMS was created by ESAero and is presented in [41].

## 2.2 Potential Improvements and Synergies

### 2.2.1 Energy Harvesting

In the energy harvesting research area the conversion of light, thermal, solar and kinetic energy into a usable form of energy is being studied. The ultimate goal is the independence of aircraft components from other power sources. [44]

#### 2.2.1.A Thermal energy

Roughly 40% of the fuel energy is emitted through exhaust gas in the form of thermal and kinetic energy. The temperature of the exhaust gases of an airplane usually reaches up to 800 ℃ and shows a significant temperature gradient to the ambient air. Therefore, the temperature difference is a prime source for energy harvesting. This temperature gradient can be converted to electric energy using a Thermoelectric generator module (TEG). So far in real life fuel efficiency has only been increased by 3% with the application of this technology. The very important weight constraint in aviation makes the implementation of such systems hard, as large liquid based cooling systems are not possible. The focus has to be on air based cooling systems for the TEG. [16]

#### 2.2.1.B Potential Energy

In this approach the gravitational potential energy of the aircraft at the end of the cruise is the target for the harvesting technology. During descent this energy can be converted to electric energy through windmilling propellers and stored in the batteries. In a study conducted by Airbus and the University of Toulouse [45] the best power management strategy during descend for a regional hybrid powered plane with a technology level of the year 2035 was studied. Therefore, four different operational modes for the propellers during descent are defined. The settings are folded, feathered (propellers can rotate parallel to airflow), transparency ( propeller can rotate but neither thrust nor drag is created) and wind turbine. Only in the wind turbine mode energy is recovered. The drag force on the aircraft varies with the operational mode and the baseline is assumed to be in folded status. A drag penalty is applied on the wind turbine and feathered mode. Afterwards, in a parametric study in which the rate of descent and the energy recovering factor is varied the conclusion arises that the aircraft should descend with the optimal speed for the L/D-ratio and either folded or transparency setting for the propellers. Therefore, the windmilling strategy shows no potential for further implementation. [45]

#### 2.2.1.C Braking energy

In this approach the dissipated kinetic energy during the landing segment should be harvested through the braking system of the aircraft. But due to the short time-frame of this phase the potential energy harvesting tool would need to be able to withstand very high power flows, which would lead to a heavy and complex device. An Airbus study for a regional twin-turbo propeller aircraft came to the conclusion that only 0.19% of the total energy consumed during a 200nm mission could be recovered. This would only equal 2kg of fuel burned. Therefore, this option is not considered to be valuable. [45]

#### 2.2.1.D Aeroelastic energy

The principle of harvesting aeroelastic energy is based on the theory that a harvester in a flow field will get excited by the flow and therefore undergo large limit-cycle oscillations. These oscillations can be converted into electric energy using piezoelectric and/or electromagnetic transducers. According to aerodynamic phenomena like vortex-induced vibrations, flutter, buffeting and galloping different energy harvesting concepts can be employed. It is highly important to monitor each phenomena well to guarantee structural soundness of the airplane. [44] In a study conducted by the University of Sheffield the voltages in the order of 10 to $10^2$ volts and $10^2$ to $10^4$ watts were obtained with a 24.5 meter wingspan of a notional civil jet aircraft. However issues like weight increment present significant challenges due to the weight of piezoelectric materials being 3 times higher than the the weight of a common aircraft structure aluminium alloy. Further, the material combination of composites with piezoelectric layers are known to have a brittle nature. A possibility for further research could be the piezoelectricity in polymers like the polyacrylonitrile (PAN). [46]

### 2.2.2 Distributed Propulsion

First a clear definition of distributed propulsion is necessary. Because any aircraft with more than one propulsor could be classified as a distributed propulsion aircraft. This however would include a very broad range of vehicles and therefore according to NASA the definition can be narrowed down to *"Distributed propulsion in aircraft application is the spanwise distribution of propulsive thrust stream such that overall vehicle benefits in terms of aerodynamic, propulsive, structural, and/or other efficiencies are mutually maximized to enhance the vehicle mission"*. [10] The field of distributed propulsion is therefore a multidisciplinary research area which includes propulsion system concepts, airframe design concepts and the electrification of the aircraft to mention a few. This approach is highly interesting to accomplish the goal of a greener and more efficient aviation in the future. [47]
According to NASA´s definition concepts like Jet Flaps, Cross-Flow Fans, Multiple Discrete Engines, Blended Wing Body design and Distributed Multi-Fans Driven by a core engine can be counted as dis-

tributed propulsion aircraft. [10] The Jet Flaps technology exhausts a thin and high velocity jet sheet at the trailing edge of the wing in order to significantly increase lift and pitching moment. These deflected jets could be used to replace conventional control surfaces and reduce the complexity of an airplane. However similar to real flap deflections the jet deflection also induces drag penalty. [48] The Cross-Flow Fan is a propulsor, powered by gas generators, which is integrated at the trailing edge of the wing. The aim is to inject the boundary layer of the upper and lower wing surface, energize it and expel it downstream to produce thrust. The exhaust flow also reduces the wake deficit by producing a wake filling effect. [49] Because of the low performance of the fan and the difficulties regarding the installation within the wing structure this concept was never put into practice for commercial aviation. The Multiple Discrete Engine approach is employed in conventional state of the art aircraft. In these designs multiple independent propellers, turbojets or turbofans are distributed along the wingspan. The multi-fan concept has only one or very few common core engines which provide power to all propulsors. The fans can be either driven by a gear system, a gas generator or electrical. This concept preserves the advantage of the superior efficiency of large core engines. [10] The aircraft presented in the figures 2.3 up to 2.5 employ this concept. The Cambridge-MIT concept (see figure 2.3) has a typical blended wing body design and employs a total of 9 distributed fans in three nacelles. Because the propulsors are placed close to the tail boundary layer ingestion can be used. This technology can increase the propulsive efficiency by reducing the ram drag. [50] The ESAero ECO 150 (see figure 2.4) is a turboelectric concept in which two turboshaft engines power generators for the spanwise distributed electrical fans. [51] In the Maxwell X-57 project from NASA two different types of propellers are employed. The cruise propellers are located at the wingtips to make use of the wingtip vortices and provide the main thrust. The high lift propellers are distributed along the wingspan (as illustrated in figure 2.5) to increase the lift through the blowing effect during take-off and landing. Thus the take-off distance and the necessary wing area can be decreased. In comparison to a conventional reference aircraft it was possible to reduce the wing area by $\approx$ 66%. [52] While the NASA Maxwell X-57 concept is expected to fly in the near future the other presented configurations are all N3+ aircraft with a market entrance around the year 2035. More information about key characteristics of the ESAero ECO 150 and other future concepts are presented in table B.1 in the Appendix.

**Figure 2.3:** Cambridge-MIT Institute design using multiple fans driven by a single core engine [10]

**Figure 2.4:** ESAero ECO 150 [51]

**Figure 2.5:** NASA Maxwell X-57 [53]

At the moment distributed powered fans have a high chance to become the main propulsive system for aircraft till N+3 concepts (up to the year 2035). These concepts are coupled with either a HEPS or fully turboelectric propulsion system. [47] In order to achieve the set goals efficient energy storage technologies and a significant increase in generating capacity is necessary. A state of the art more-electric aircraft (MEA) has an onboard power consumption of roughly 1.5 MW [54] while a commercial distributed propulsion aircraft concept can reach values of up to 50 MW. [55]

## 2.3 Alternative and/or Complementing Solutions

### 2.3.1 Novel Configurations

The conventional tube plus wing aircraft design is close to reaching its performance limit. Therefore, different design possibilities are necessary to satisfy the environmental requirements of future aviation, carry a large number of passengers over long ranges, reduce direct operating costs and increase aerodynamic efficiency. [56] In this section the blended-wing-body (BWB) and strut-braced wing configurations are highlighted.

The BWB concept which is similar to the design presented in the figure 2.3 is a promising approach for these new requirements. [56] The design presents good lift over drag ratios and therefore better fuel efficiency. The engines could be embedded into the fuselage and reduce fuel burn further by ingesting the boundary layer (BLI). [39] Because of the simplicity of this design, where the fuselage is included in a big wing, it offers great potential for manufacturing as no complex joints between fuselage and wings are

**Figure 2.6:** BOEING Sugar High [23]

needed. Another advantage are the simple hinged trailing-edge control surfaces. This could lead to a substantial reduction of parts (≈30%) which could significantly reduce the production cost. This design is also ideal for a family of airplanes, as the stretching needed to apply for a wide range of passengers is done spanwise. Therefore, the wing area automatically increases with higher payload weight. Once considered "show-stopper" issues of this design concept have been either solved or reduced to technical challenges. In the appendix in table B.2 problems or areas of risk which can be applied to BWB design are presented. [50]

The strut-braced wing concept was first mentioned by Werner Pfenninger in the early 1950s. This design presented special challenges due to a highly coupled aerodynamical and structural performance. The full potential could not be reached in these early days also due to low computational power and techniques. During the Subsonic Ultra Green Aircraft Research (SUGAR) program by BOEING and NASA the configuration was re-examined. One design variation of this project is presented in figure 2.6. The characteristic struts beneath the wing provide the advantage of structural support to the high aspect ratio wing. Furthermore, the thickness to chord ratio can be reduced and therefore the take-off weight can be significantly decreased. [57] The SUGAR High concept was able to achieve a 39% fuel reduction in a simulation for a 900nm mission when compared with a B737 class aircraft. The BOEING study still identified areas with possible improvements potentially saving of up to 58% in fuel consumption. This design could be coupled with battery gas turbine hybrid propulsion architecture to increase efficiency even further. The biggest design challenge for this concept is to control the weight of the wing while making it aerodynamically effective. [58]

While these concepts provide big potentials they also present significant challenges as already mentioned which need to be addressed. The studies included technologies which are not fully developed

yet as well. The Design tools are still in a very early stage for these aircraft configurations and depend mostly on empirical models and therefore further research in this area is definitely necessary. [56] The aerodynamic interactions with the structure need to be investigated further, detailed finite element models and aeroelastic tests for validation are necessary. [58]

### 2.3.2 Fuel Cells

Fuel Cells are an alternative to rechargeable battery technology described in sub-section 2.1.5 to power the propulsion system of an aircraft. Opposite to heat engines fuel cells use an electrochemical reaction to directly produce power from the stored chemical energy. The power production is only limited by the ability to supply fuel to the cell. [59] The fuel cell produces electric energy trough the chemical reaction between the fuel, which can be hydrogen or methanol for example, and oxygen. The oxygen for the reaction can be sourced from air-intakes while the hydrogen is stored onboard. [32] For UAV applications three main fuel cell types exist: the polymer electrolyte membrane fuel cell (PEMFC), the direct methanol fuel cell (DMFC) and the solid-oxide fuel cell (SOFC). The low operating temperatures of the PEMFC and DMFC make these types especially interesting for UAV applications. The characteristics of the three fuel cell types are presented in table 2.3. Due to good efficiency, low cost and low operating operating temperature of the PEMFC this cell type shows the greatest potential of these three. [60]

| | Fuel | Efficiency | Temp [℃] | Specific power (W/kg) | captial cost [$/kW] |
|---|---|---|---|---|---|
| PEMFC | Hydrogen | 40 - 60 | 30 - 100 | 400 - 1000 | 100 |
| DMFC | Methanol | 20 - 30 | 20 - 90 | 50 - 200 | 200 |
| SOFC | Hydrocrabon | 25 - 50 | 500 - 1000 | $> 800$ | - |

**Table 2.3:** Fuel cell types applied in small UAVs [61] [62] [59]

Hydrogen has not only a low density of only 0.089 $kg/m^3$ at standard room temperature but also a low boiling point of -252.9℃. These characteristics complicate storage significantly. In order to improve the gravimetric and volumetric efficiency three different storage concepts are currently employed in UAVs. Hydrogen can be stored as a compressed gas, in liquid form or as chemical hydrogen. The utilization of pressurized tanks for a compressed gas is the simplest and most frequently used method for UAVs. Storing gases at high pressures is not only associated with safety problems but also presents a significant challenge in the design process. [60] The complexity of the storage devices and the constellation of the tanks along the aerial vehicle are presented in [63]. Due to the restrictions of the pressurized tanks the structural flexibility during the design process decreases significantly. Another crucial technical and operational challenge is presented by the availability of the required fuel and infrastructure to refill the UAV at remote locations. [59] Small energy output per second is a challenge especially during power intensive segments like Take-off, Climb and windy operating conditions. [32] [59] Often fuel cells find applications in combination with some sort of energy harvesting technology. Together these systems

can obtain energy densities of up to 400 Wh/kg and have been were employed in very long endurance and wide wing UAVs like the Heliplat. [32]

Currently fuel-cell-based propulsion systems for small UAVs are an active research area. Still further developments in the field of hydrogen storage and refilling, impact of altitude on the performance of the fuel cell, water management for non-humidified operation and load leveling need to be achieved to realize a robust operational vehicle with widespread use. [59] A preliminary design methodology for a fuel-based hybrid-electric UAV is presented in [64].

# 3

# Numerical Model for the Hybrid Powertrain

## Contents

This chapter introduces a numerical MATLAB model for hybrid propulsion system components. In the thesis "*Design and Development of a Hybrid Electric Propulsion System for Unmanned Aerial Vehicles*" by Machado [65] at the University of Victoria a hybrid test bench was developed and experimental data recorded. In figures 3.1a and 3.1b the test bench and the distribution of the components, which are briefly described in table 3.1, are presented. The detailed specifications of each component are described in the according sections. Therefore the propulsion models created in this thesis can be evaluated with the provided measurement series. Thus, it is possible to obtain models with high accuracy which can be implemented into any airplane concept to efficiently compare the different propulsion system architectures. First, the *Framework* in which the component models are embedded is explained followed by the development of a Propeller, Battery, EM and ICE model. Afterwards the single components are integrated into a parallel hybrid propulsion system and the operating strategies EM only, ICE only, Dash and Regernaritve Brake modes are validated.

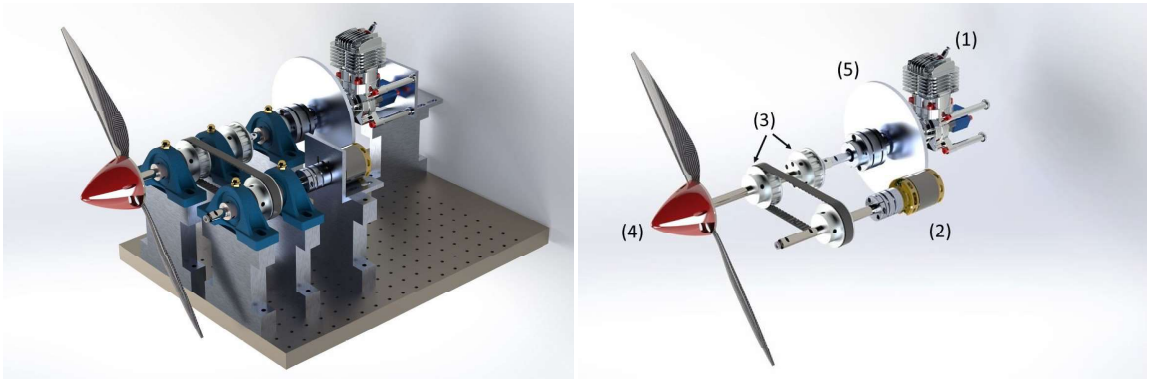


**(a)** **(b)**

**Figure 3.1:** CAD rendering of Hybrid Test Bench at CfAR: (a)overview [65], (b)components [65]

| Type | Name | Numbering |
|---|---|---|
| Engine | Desert Aircraft DA35 (2 Stroke) | 1 |
| Motor | AXi 4130/20 GOLD LINE V2 | 2 |
| Mechanical Coupling | Timing Belt + Align RC one-way bearing | 3 |
| Propeller | 19´ x 10´ fixed pitch (unknown brand) | 4 |
| Mechanical Capacitor | Flywheel (unknown brand) | 5 |
| Battery | Lithium Polymer | not portrayed |

**Table 3.1:** Components of Hybrid Test Bench

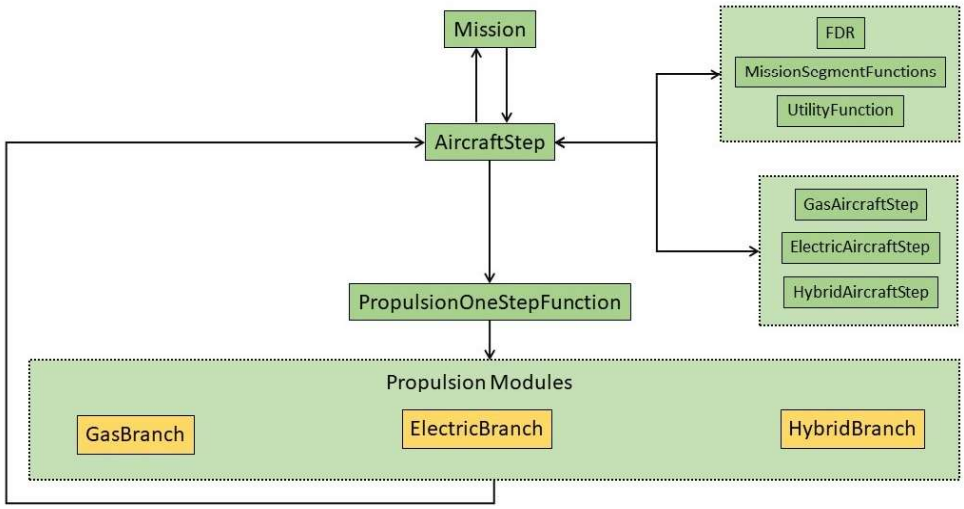


**Figure 3.2:** Flowchart for the Framework of the hybrid propulsion UAV

## 3.1 Framework

The Framework in which the hybrid propulsion system module is embedded is an adaption of a project by the Center of Aerospace Research (CfAR) from the University of Victoria. The code is structured as a modular system and single parts of the Framework can easily be exchanged. Therefore, the separate models can be simply updated and the performance of different propulsion systems can be evaluated quickly. The *Framework* employs an object oriented programming approach. The objects are structured into one super-class the *"Aircraft-Class"* and three subclasses the *"GasAircraft"*, *"ElectricAircraft"* and the *"HybridAircraft - Class"*. In the super-class, which is determined in the *AircraftStep* file, aircraft characteristics like lift, drag and dynamics (*MissionSegmentFunctions*) such as velocity, cruise, climb/descent and launch are defined. Furthermore this file includes *UtilityFunctions* to compute for example the air density $\rho$ according to the current altitude and a Flight-Data-Recording (FDR) system. The subclasses specify the according propulsion type characteristics which are described in detail in the section 4.3. [66]

The flowchart for the numerical model is presented in figure 3.2. The starting point of each simulation is the *"Mission"* file. In this function the propulsion type is chosen and the mission is defined. In the next step the *AircraftStep* is called, here the FDR is started and the flight characteristics are determined with the *MissionSegmentFunctions* and the *UtilityFunctions* for the selected aircraft characteristics. Further, this file calls the corresponding propulsion module, set in the *Mission* file, with the *PropulsionOneStepFunction*. This module generates the output of the propulsion module and afterwards feeds back the information to the *AircraftStep* function. After the timestep is completed the process starts again in the *Mission* file.

## 3.2 Powertrain Component Models

The first step in the Framework development for a complete hybrid propulsion system is the formulation and evaluation of both independent branches: electrical and combustion. In addition to these two branches of the hybrid propulsion model, both battery and propeller models are presented in separate sub-sections prior to the electrical and combustion branches. The assessment of the electrical model is performed with a simple experimental setup in which the motor is directly connected to a propeller. On the other hand, the combustion model is compared with data provided by the manufacturer. These independent models are going to be combined into the hybrid system in a subsequent section.

### 3.2.1 Propeller Model

The starting point of each propulsion branch of the hybrid system is the propeller model. In this section of the simulation model the required thrust, which is determined by the flight phase and airplane characteristics, is converted into the power required at the propeller shaft. Furthermore also the necessary rotational speed of the propeller is determined. The model consists of only one file the *"propModel"* function.

In most of the available literature either Blade-Element-Momemtum-Theory (BEMT) or simple mathematical models for the thrust and power coefficient like in [67] are employed to model the propeller. [68] In this work, the first step is the verification of static experimental setups for which the BEMT method is not applicable. Therefore, a simple mathematical model with the thrust and power coefficients is selected for the propeller. The main performance characteristics of the propeller are shaft power and produced thrust. These variables can be expressed in non-dimensional terms via the thrust and power coefficient $C_T$ and $C_P$, respectively the equations 3.1 and 3.2 define those variables. In the formulas *n* represents the rotations per second, $\rho$ stands for air density and *D* is the propeller diameter in meter. [67]

$$C_T = \frac{Thrust}{\rho * n^2 * D^4} \tag{3.1}$$

$$C_P = \frac{Power}{\rho * n^3 * D^5} \tag{3.2}$$

Each propeller has its own set of $C_T$ and $C_P$ values as they depend on pitch, diameter and shape of the blades. [68] The model in this work needs a database similar to the ones presented in [69] for various propellers as input. In this database the $C_T$ and $C_P$ are stored over different rotational speeds. Out of these datapoints a curve is created with MATLAB function *fit* and the *"spline"*option. The first approximation curves for the two coefficients are presented in figure 3.3 and 3.4.

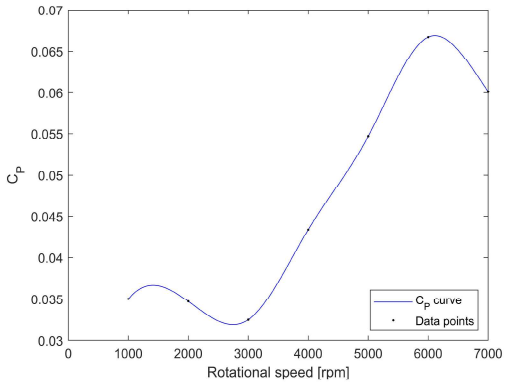


**Figure 3.3:** $C_P$ curve for a ACP 19'x10'E propeller

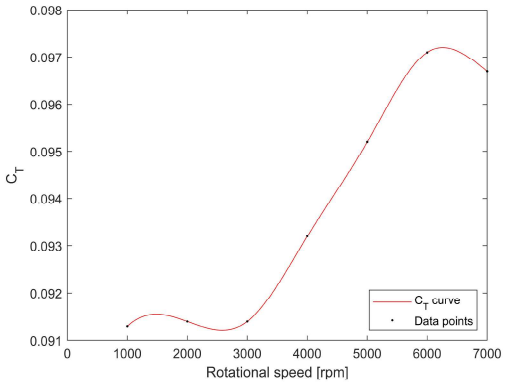


**Figure 3.4:** $C_T$ curve for a ACP 19'x10'E propeller

The propeller used by Leonardo in [65] is not exactly specified and only few details like diameter and pitch are known. Therefore, the already presented ACP propeller was used as a first approximation as it has the same diameter and pitch. To validate this approximation the actual $C_T$ and $C_P$ curves are computed with the formulas 3.1 and 3.2 from the experimental data presented in the appendix in table B.5. The results are presented in figures 3.5 and 3.6. The power coefficient neither shows a similar trend nor is the magnitude acceptable over the whole rpm range. The $C_T$ curve is closer to the form of the ACP propeller but still significant deviations in terms of magnitude and rpms are present. Therefore, this approximation is not considered to be sufficient.

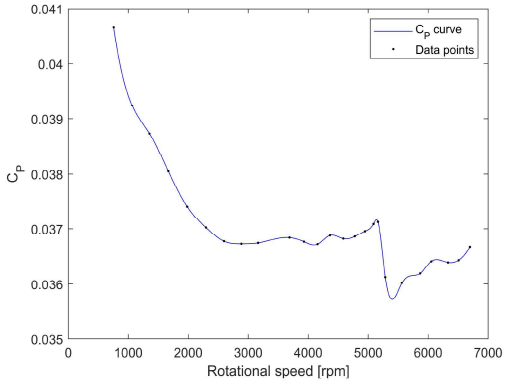


**Figure 3.5:** $C_P$ curve for propeller of experiment

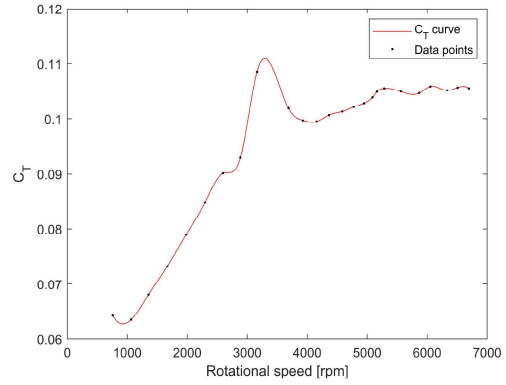


**Figure 3.6:** $C_T$ curve for propeller of experiment

Because no appropriate propeller data exists and the approximation shows no acceptable results the simulation model will be operated with the experimental curves. In other projects the according curves for the employed propeller can easily be fed into the model. The accuracy of the model is not going to be influenced by this decision.

The theoretical background information presented earlier in this section is now applied to the function

*"PropModel"*. The flowchart of this function is presented in figure 3.7. In the $1^{st}$ step the minimum and maximum operating rpm are defined in a rpm vector. Further, the $C_T$ curve presented in figure 3.6 is loaded. From this step onwards the loop starts with selecting the current rpm setting. Then the according $C_T$ value is obtained from fitted curves. The thrust for the current rpm and $C_T$ is computed with equation 3.1. In the last step, the relative error, with the required thrust, of the prediction is computed. If the error is small enough the rpm is selected and the responding values for $C_T$ and $C_P$ are determined. These values are then passed on to the next model of the propulsion system further upstream.

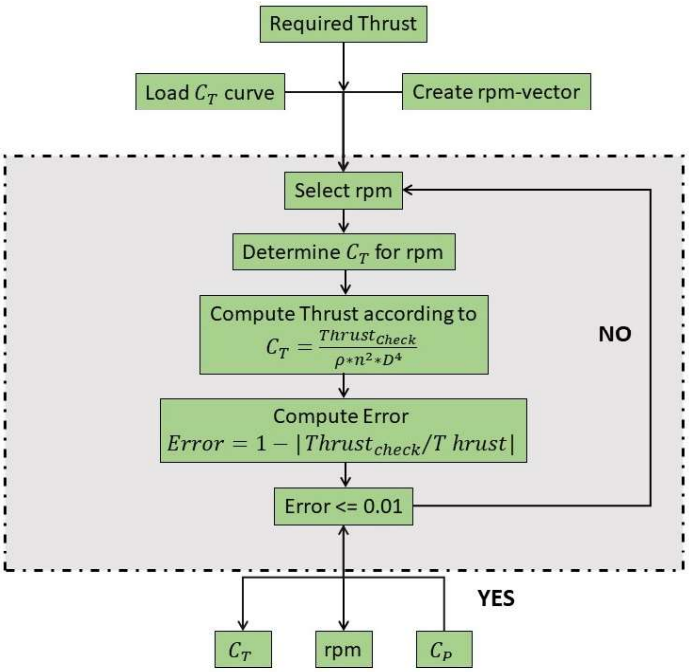


**Figure 3.7:** Flowchart of rpm determination function

### 3.2.2 Battery Model

The battery model from a research project of CfAR [66] is chosen for this work. The theory of this model is based on a MATHWORKS project in which the charge and discharge characteristics of various battery types are studied. [70] A Lithium-Polymer(Li-Po) battery will be implemented as these energy sources are still the most wide spread technology in UAVs and the same type is utilized in [65] by Leonardo, whose results should be validated.

The charge and discharge curve of this battery type are described by equations 3.3 and 3.4. In charge mode the nominal battery current $I_n$ is greater than 0 and in discharge it is smaller than 0. [70] Through 1A discharge experiments at CfAR the exponential voltage coefficient A, exponential capacity coefficient $\beta$ and the polarity voltage K are determined. Further, the variable Q stands for the maximum capacity

of the battery, $I_t$ is battery current during the timestep, $V_0$ is the constant battery voltage and $V$ is the output voltage of the battery.

- $Charge\ (I_n < 0)$:

$$V(I_t, I_n) = V_0 - \frac{K * Q * I_n}{I_t + 0.1Q} - \frac{K * Q * I_t}{Q - I_t} + A * exp(-\beta * I_t) \tag{3.3}$$

- $Discharge\ (I_n > 0)$:

$$V(I_t, I_n) = V_0 - \frac{K * Q * I_n}{Q - I_t} - \frac{K * Q * I_t}{Q - I_t} + A * exp(-\beta * I_t) \tag{3.4}$$

The battery model was not developed in this work and therefore only a brief introduction is given, a more detailed description is found in [66].

### 3.2.3 Electrical branch

The electrical branch is composed by a battery, an electronic-speed-controller (ESC) and a motor. The function *"ElectricPropulsionOneStep"* defines the complete branch. The key performance parameters for this part of the model, which need to be determined, are the current drawn from the battery, the voltage level of the battery and the throttle setting of the EM. Machado [65] recorded experimental values for these variables with a simple propeller test and therefore the Framework can be validated with those experimental values.

The flowchart of the function is presented in figure 3.8. In the first steps, the propeller model is included to determine the necessary rpm of the propeller according to the required thrust with the *"propModel"* function. The same function also obtains the thrust and power coefficients for the given rotational speed. Afterwards, the EM model starts with the determination of the motor efficiency in the *"EMDatabase"* file. This efficiency is necessary as an input to the equations of the equivalent circuit stored in the *"ElectricPropulsionEquations"* file. In this function the torque, voltage and current of the EM are determined in cooperation with the *"BatteryModel"*. In the last step, the State of Charge (SoC) is computed again with the *"BatteryModel"* function. The details of each function are going to be discussed in more depth later in this section.

The starting point for the electric branch is the propeller model which is described in detail in sub-section 3.2.1. The outputs of this model are the rpm, the thrust-coefficient $C_T$ and the power-coefficient $C_P$. The power at the propeller can be determined with equation 3.2. In equation 3.5 the rotational speed is converted from rpms to rad/s.

$$w_{shaft} = \frac{2 * \pi}{60} * rpm \tag{3.5}$$

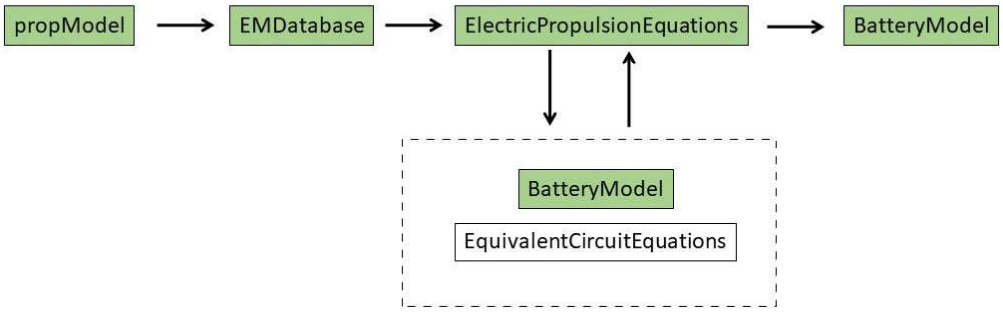


**Figure 3.8:** Flowchart of EctricPropulsionOneStep function

After this step, it is possible to obtain the torque at the propeller with equation 3.6.

$$P_{shaft} = T_{shaft} * w_{shaft} \tag{3.6}$$

The friction losses along the power flow path between propeller and EM are accounted for with 3% of losses as a first approximation (based on [71][1]). Therefore, it is possible to obtain the torque at the EM $T_{EM}$ with equation 3.7. [71]

$$T_{EM} = T_{shaft} * 0.97 \tag{3.7}$$

In order to determine the current of the motor the efficiency of the EM is necessary. This value depends on the supplied voltage and the requested torque. Two datasheets of the manufacturer, presented in the appendix of [65], are the starting point for obtaining the efficiency. These two sheets present the efficiency according to two voltage levels of 25V and 20V and the required torque. The scattered points of both datasets are fitted with a polynomial function of the $4^{th}$ degree. The results of this fitting process are presented in figure 3.9. The root mean squared errors for both functions has a very low error and the R-squared attribute also presents good values very close to 1 as shown in table 3.2. The function *"EMdatabase"* first obtains the efficiency for both voltage levels from the presented curves. Then it interpolates depending on the voltage levels according to equation 3.8, if the efficiency for this torque request is higher at 25V, or 3.9 if the efficiency for the demanded torque is higher at 20V.

$$\eta_{EM} = \frac{Voltage - 20}{25.2 - 20} * (\eta_{EM25V} - \eta_{EM20V}) + \eta_{EM20V} \tag{3.8}$$

[1] In this reference the propeller shaft efficiency is estimated with a strain test bench at 99%. Because of the stated inaccuracy of the measurement method for the friction coefficient an extra safety factor is considered. For the purpose of this work and the relatively small influence of the mechanical friction in this experimental setup the approximation is considered accurate enough with 97%. To increase accuracy the author suggest additional on the mechanical friction focused experimental tests and afterwards an optimization process.

$$\eta_{EM} = \frac{Voltage - 20}{25.2 - 20} * (\eta_{EM20V} - \eta_{EM25V}) + \eta_{EM25V} \tag{3.9}$$

Even if the voltage level drops below 20V this datasheet is still the base for the efficiency modeling due to the lack of available data by the manufacturer. This aspect of the model needs to be improved especially because the efficiency has considerable fluctuations depending on voltage levels at high torque request. Also the datasheet lacks data for torque requests smaller than 0.3 N.m. Therefore the efficiency in these ranges should be carefully assessed.

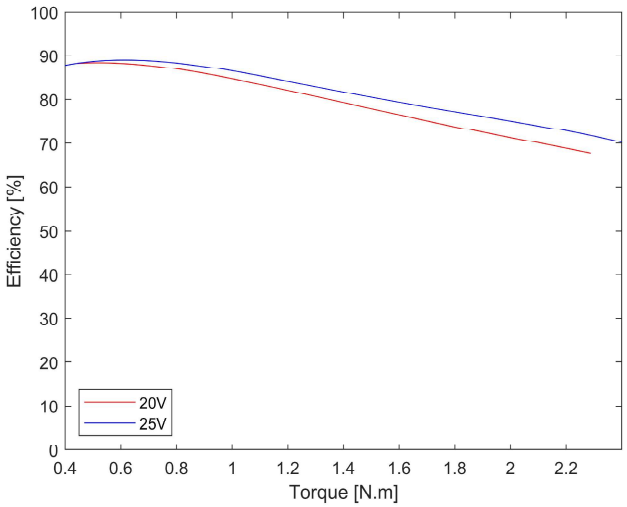


**Figure 3.9:** Efficiency curves of EM over the torque

| Voltage | R-squared | RMSE |
|---|---|---|
| 20 | 0.9999 | 6.0267e-04 |
| 25 | 0.9995 | 1.3230e-03 |

**Table 3.2:** Fit characteristics of curves

Now the EM itself needs to be modeled. More information about brushless and brushed DC motors is presented in [72]. The equations modeling the EM will be stored in the function *"ElectricPropulsionEquations"*. It is a common practice today to model brushless and brushed DC motors with a simple equivalent circuit. To fully characterize it the classic motor constants (the rpm proportionality constant $K_V$, the no load current $I_0$ and the internal resistance $R_m$) are necessary. [73] The equivalent circuit with the specifying variables and its values for the employed AXI 4130/20 motor are presented in figure 3.10 and in table 3.3. [73] [74]

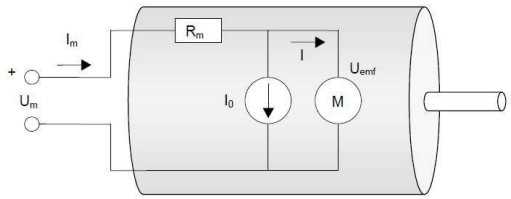


**Figure 3.10:** Equivalent circuit of DC motor [73]

| Detail | Value | Unit |
|---|---|---|
| $K_V$ | 305 | [RPM/V] |
| $R_m$ | 99 | [m$\Omega$] |
| $I_0$ | 1.1 | [A] |
| max Power | 1650 | [W] |
| max efficiency | 90 | [%] |
| max Current | 55 | [A] |

**Table 3.3:** Characteristics of AXI 4130/20

The rotational speed of the shaft is directly connected to the electric-motoric-force (EMF) Voltage $U_{emf}$.

This Voltage is the difference of the supplied Voltage $U_m$ and the voltage drop across the internal resistance as presented in equation 3.10.

$$U_{emf} = U_m - I_m * R_m \tag{3.10}$$

The product of the rotational proportionality constant with the EMF-Voltage results in the rotational speed of the EM shaft as presented in equation 3.11.

$$w_{shaft} = K_V * (U_m - I_m * R_m) \tag{3.11}$$

The torque output of the motor $T_{EM}$ can be computed according to 3.12 and depends on the current flow through the motor.

$$T_{EM} = \frac{I_m - I_0}{K_V} \tag{3.12}$$

The equations 3.11 and 3.12 need to be adjusted to integrate the throttle variable. The torque of the EM is produced by the current at the windings of the EM. To compare the results of the model with the measurements of the experiment a correlation between this value and the battery current needs to be established. The same applies to the voltage. The ESC, inbetween the battery and the EM, controls the rotational speed of the EM by reducing the voltage level according to the throttle setting. [75] Therefore, the voltage level is smaller at the EM than at the battery for throttle settings below 100%. Due to power conservation laws between the battery and the EM, the current needs to be increased by the same factor. The relations presented in the equations 3.13 and 3.14 can be derived.

$$I_m = \frac{I_{battery}}{Throttle} * \eta_{EM} \tag{3.13}$$

$$U_m = U_{battery} * Throttle \tag{3.14}$$

The equations 3.13 and 3.14 are inserted into 3.11 and 3.12 to obtain the formulas 3.15 and 3.16, which characterizes the torque and the rotational speed of the EM in terms of battery current and voltage as well as throttle setting. The determination of the SoC of the battery is now possible.

$$T_{EM} = \frac{\frac{I_{battery}}{Throttle} - I_0}{K_V} \tag{3.15}$$

$$w_{shaft} = K_V * (U_{battery} * Throttle - \frac{I_{battery}}{Throttle} * R_m) \tag{3.16}$$

The equations 3.15 and 3.16 are coupled with the battery model in the *"ElectricPropulsionEquations"* function. The torque of the EM ($T_{EM}$) is known at this point through the equation 3.7 and the already obtained efficiency. The rotational speed of the system is determined by the *"propModel"* function. This leaves 3 equations with the 3 unknowns (Throttle, $I_{battery}$ and $V_{battery}$). This system of non-linear

equations can be solved with the MATLAB function *"fsolve"*. The function requires initial guesses $X_0$ for the 3 unknowns. The system of equations is then solved iteratively until the error defined by 3.17 becomes lower than a threshold value of $10^{-5}$.

$$error = \begin{bmatrix} V_{battery} - V_{batterycalc} \\ rpm - (V_{battery} * Throttle - \frac{I_{battery}}{Throttle} * R_m) * K_V \\ T_{em} - ((\frac{I_{battery}}{Throttle}) - I_0)/(KV * 2 * \frac{pi}{60}) \end{bmatrix} \tag{3.17}$$

In the post processing of this branch the SoC of the battery is determined with the *"batteryModel"* function. This step is necessary as only by now the correct current drawn from the battery is known.
The evaluation of the model is performed with the results of an EM-Propeller test bench as shown in figure 3.11. In this configuration the EM is directly connected to the propeller shaft. As already stated, the evaluation parameters are the battery current, battery voltage and the throttle setting of the EM.

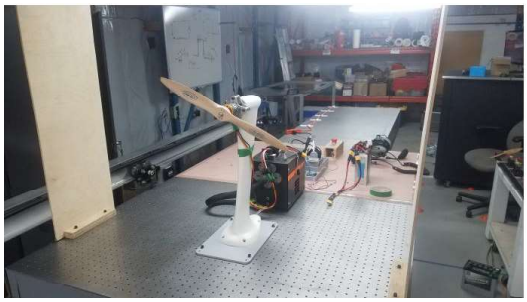

**Figure 3.11:** Electric motor Test configuration [65]

The $C_T$ and $C_P$ values of the propeller are important inputs for the model as stated in sub-section 3.2.1. The experimental curves are employed in order to achieve good accuracy in the results.
The Framework is going to be evaluated with the propeller test data (presented in table B.5 in the Appendix). The performance parameters for the assessment of the simulation model are the current of the motor $I_{motor}$, the current drawn from the battery $I_{battery}$, the voltage level of the battery $V_{battery}$, the throttle setting of the EM, the torque at the shaft of the EM $T_{shaft}$ and the rpm prediction of the propeller. The relative errors (negative error stands for overprediction) for each test point are presented in the table 3.4. The results for the rpm prediction and the torque of the shaft $T_{shaft}$ are depicted in figures 3.12 and 3.13 respectively. As stated in sub-section 3.2.1, the *"propModel"* function achieves very close results to the experimental ones with a maximum error of only 5% at low rpm settings. The torque prediction which is directly connected to the rpm value through the equations 3.2 and 3.6 has a maximum error of 10% due to the rpm error at this point. Besides this extremum, the simulation shows a good correlation with a neglectable error around 1% - 3%.

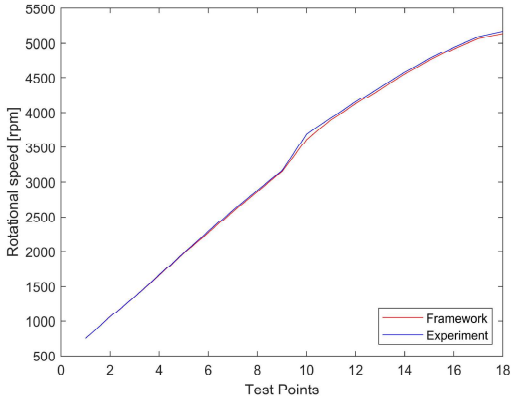


**Figure 3.12:** Rotational speed over the test points

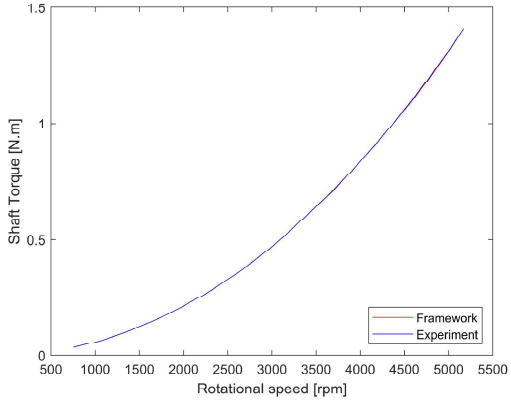


**Figure 3.13:** Shaft power at the propeller over rotational speed

The current and the throttle curves of the EM are presented in the graphs 3.14 and 3.15 respectively. A greater throttle setting leads to a higher amount of current being drawn from the battery and as a consequence the battery will deplete faster. Therefore, these two variables influence the SoC of the battery and have a big impact on the operating mode and remaining time of the mission. The throttle simulation achieves results with a varying error within -1% and 4%, which are deemed satisfying. But the current of the motor shows a significant error for low rpm settings with a maximum value of 29%, which quickly drops and stabilizes (around 7% to 9%). The torque value up to 2000 rpm is below 0.2 N.m, which is lower than the starting data (0.3 N.m) from the characterization of the motor efficiency curve as presented in [65]. Therefore, one possible reason could be the overprediction of the motor efficiency as it leads to higher currents at the EM.

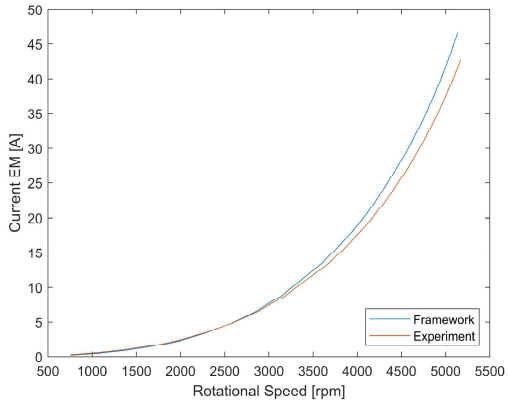


**Figure 3.14:** Current flow of the AXI 4130/20 over rotational speed

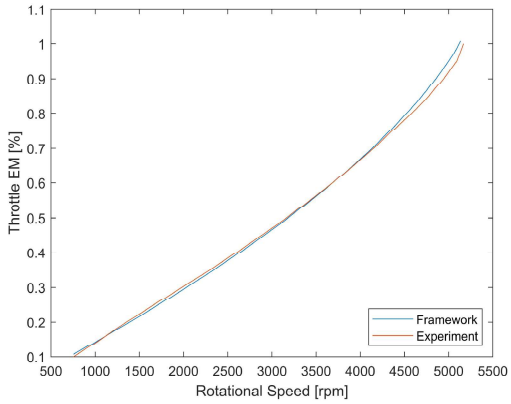


**Figure 3.15:** Throttle values of the AXI 4130/20 over rotational speed

The last two studied parameters are the voltage level and current drawn from the battery. These two variables are compared with measurements at the ESC, as these should present similar values. In the

experiments, it was only possible to measure the changes in these two parameters from 35% of throttle onwards. The trends of both curves are in agreement, as can be observed in figures 3.16 and 3.17. While the current presents a significant error at 35% throttle, which reduces as the rpm increases. The voltage of the battery only presented minor errors and is therefore deemed a good approximation.

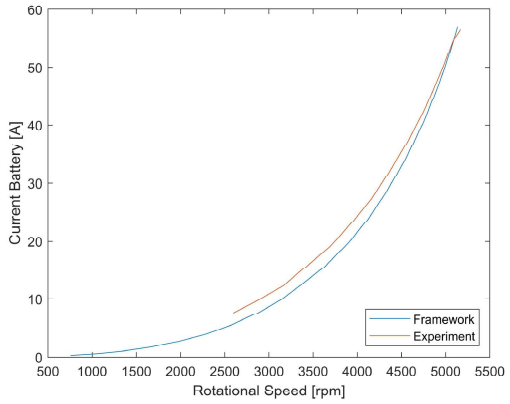


**Figure 3.16:** Drawn current from the battery over rotational speed

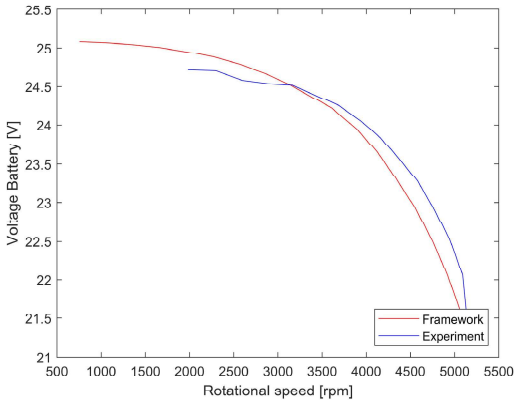


**Figure 3.17:** Voltage level of the battery over rotational speed

| | | Prediction Error | | | | | |
|---|---|---|---|---|---|---|---|
| Test Point | Throttle Setting[%] | Throttle | Current Battery | Voltage Battery | Current Motor | Torque | RPM |
| 1 | 10 | -7% | - | -1% | 21% | -2% | 0% |
| 2 | 15 | -1% | - | -1% | 16% | -2% | 0% |
| 3 | 20 | 3% | - | -1% | 12% | -1% | 0% |
| 4 | 25 | 4% | - | -1% | 9% | -1% | 0% |
| 5 | 30 | 3% | - | -1% | 5% | -1% | 0% |
| 6 | 35 | 3% | - | -1% | 4% | 0% | 1% |
| 7 | 40 | 3% | 28% | -1% | 2% | 0% | 1% |
| 8 | 45 | 2% | 24% | -1% | -1% | -1% | 1% |
| 9 | 50 | 1% | 19% | 0% | -3% | -1% | 0% |
| 10 | 55 | 3% | 19% | 0% | 0% | 2% | 2% |
| 11 | 60 | 1% | 15% | 0% | -5% | 0% | 1% |
| 12 | 65 | 0% | 12% | 1% | -6% | 0% | 1% |
| 13 | 70 | 0% | 11% | 1% | -7% | -1% | 1% |
| 14 | 75 | -1% | 8% | 2% | -8% | -1% | 1% |
| 15 | 80 | -2% | 6% | 2% | -9% | -1% | 0% |
| 16 | 85 | -2% | 4% | 2% | -9% | -1% | 0% |
| 17 | 95 | -3% | 2% | 2% | -9% | -1% | 0% |
| 18 | 100 | -1% | -1% | 0% | -9% | -1% | 1% |

**Table 3.4:** Prediction errors of the simulation

The issues still present in the mode, like the sharp inclination of the motor current for high throttle settings and the poor discretization of the EM efficiency, should be studied in more detail. More experiments with a test bench just for the EM are necessary to fully map its performance. So far, also the friction losses of the propeller - EM connection as well as the propeller efficiency are just accounted for with a simple efficiency factor. In spite of these issues, the model shows good correlation for the performance parameters. Therefore, the implementation of the electric branch into the Framework is considered to

be valid and feasible.

### 3.2.4 Combustion branch

Besides the electric branch the simulation model needs to cover the combustion engine. The function *"GasPropulsionOneStep"* defines this part of the simulation mode. The evaluated performance parameters are the power of the engine, throttle setting, brake-specific-fuel-consumption (BSFC) and the fuel flow. The engine employed in the *Hybrid Test Bench* is, as presented in table 3.1, a Desert Aircraft - 35cc two-stroke engine. These engine types are widespread in the light weight UAV market because of their great power-to-weight ratios. [65] More in depth information about 2-stroke engines and their theoretical background can be found in [76]. A SIMULINK model for this engine type with a turbocharger was developed by Turrson in his master thesis [77]. The numerical model needs to include the combustion chamber, air-intake and exhaust manifold. The different combustion chamber´s types and the possible modelling techniques present significant challenges. [77]
The focus of this thesis lies on the realization of the whole hybrid propulsion Framework rather than single units and therefore a different approach to model the 2-stroke engine is pursued. If the modeling of certain process deems itself to be extensive, Surrogate or Black-Box Models are utilized. Such occasions often arise in engineering applications like in computational fluid dynamics or finite elements methods. In these models, the real functions are replaced by models which try to emulate their physics. The model can be based on linear functions, decision trees, artificial neural networks, radial based functions (RBF) or Kriging regressions to mention the most important methods. These methods can construct a prediction model out of experimental data. [78] Engine datasheets for the power output and the BSFC depending on the throttle and rpm setting of the engine are available. This data is presented in the tables B.3 and B.4 in the appendix and is going to be the basis of the surrogate model. [65] In this work, the surrogate model is studied to be realized by either Kriging regressions or the RBF method.

#### 3.2.4.A Kriging Method

The Kriging method models values by Gaussian processes. In the most simple form the equation 3.18 states the basis of the model. Here $\beta_0$ represents a linear regression of the data which models the drift of the process mean over the domain. The second parameter is the error term $\epsilon$ from the linear regression. [79]

$$y = \beta_0 + \epsilon \tag{3.18}$$

The deviation from the linear regression is assumed to be a Gaussian process with zero mean and a covariance distance matrix V defined in equation 3.19. This matrix forces the response surface through

| Name | Correlation Matrix R | |
|---|---|---|
| Gaussian | $e^{-\theta\|d\|}$ | |
| Exponential | $e^{-\theta d^2}$ | |
| Linear | $max\{0, 1-\theta\|d\|\}$ | |
| Spherical | $1-1.5*\xi+0.5*\xi^3$ | $\xi = min\{1, \|\theta/d\|\}$ |
| Cubic | $1-3*+2\xi*\xi^3$ | $\xi = min\{1, \|\theta/d\|\}$ |

**Table 3.5:** Spatial correlation functions of the Kriging method [80]

the data points by weighting the correlation of the nearby points. [79] Here *s* represents the design sites and x the current position.

$$V(s,x) = \sigma^2 * R * (x-s) \tag{3.19}$$

The smoothness of the response surface is influenced by the spatial correlation function R. Possible correlation functions are presented in table 3.5. The spline function is another popular correlation method which varies according to the current region and is explained in [80] in more detail. In table 3.5, *d* represents the difference between the design site *s* and the current position *x*. An optimization algorithm determines the process variance $\sigma^2$ and the regression parameter $\beta^*$, which are the most consistent with the experimental data. These two parameters depend on the correlation parameter $\theta$ and therefore also set this value. The Kriging method is very flexible to approximate many different and complex response functions and it can provide a confidence interval, but the method gets computationally expensive if the data is high dimensional. [79] [81]

The MATLAB toolbox *Dacefit* from the Technical University of Denmark is utilized in this work for the Kriging surrogate model. The toolbox and the included functions are described in depth in [80].

#### 3.2.4.B Radial Basis Functions

The Radial Basis Functions method approximates multivariable functions with linear combinations of terms based on a single variable basis function, the RBF. This function is radially symmetric about its center. The basic RBF interpolant is stated in equation 3.20. In this equation $\psi_j(x)$ is some radial function, $\lambda_i$ is the expansion coefficient and $x$ represents a set of data points. The expansion coefficient is defined by the interpolation condition that $f(x)$ equals the corresponding data value of $x_j$. [82]

$$f(x) = \sum_{j=1}^{n} \lambda_i * \psi_j(x)(|x - x_j|) \tag{3.20}$$

Typical RBFs are summarized in table 3.6. Nowadays, the RBF method is very popular to accurately interpolate multidimensional data. The advantages of the RBFs are the simplicity to implement the method and its low complexity, that does not increase as the dimensions of the problem increase. On the other hand, the determination of the expansion coefficients is computationally extensive. The approach

| Type of basis function | $\psi(r)(r > 0)$ |
|---|---|
| Gaussian (G) | $e^{(\epsilon r)^2}$ |
| Inverse multiquadratic (IMQ) | $\frac{1}{\sqrt{1+(\epsilon r)^2}}$ |
| Multiquadratic (MQ) | $\sqrt{1+(\epsilon r)^2}$ |
| Thin Plate Spline (TPS) | $r^2 \log r$ |
| Biharmonic (BH) | r |

**Table 3.6:** Commonly used radial basis functions [82]

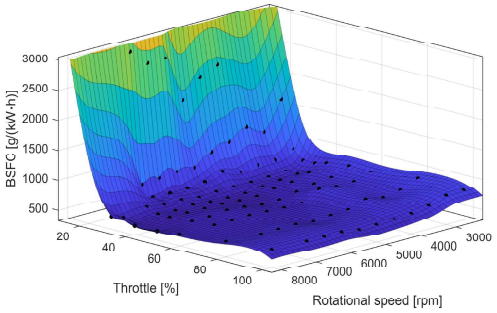


**Figure 3.18:** 3D curve fit for the BSFC data of DA-35 depending on rpm and throttle

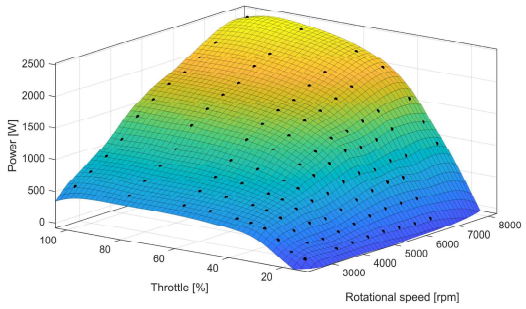


**Figure 3.19:** 3D curve fit for the power data of DA-35 depending on rpm and throttle

is applied in pattern recognition, medical imaging and image warping for example. [82]

In this work the RBFs are simulated with a MATLAB package provided by the Technical University of Riga. [83]

#### 3.2.4.C Surrogate Model evaluation

In the thesis by Leonardo, fuel flow measurements were performed for an ICE only test bench. During the experiments the fuel flow rate was not directly recorded with a flow meter, but through weight measurements at the fuel tank with a load cell over time. The results present a curve with a $\approx 14\%$ decrease of fuel flow rate over the increase of throttle from $50\%$ to $60\%$. [65] This outcome could be strongly influenced by imprecision of the measurement tool as normally the throttle setting controls the valve of the fuel pipe. This connects bigger throttle settings with a more open fuel flow valve. Due to the doubts regarding the accuracy of the measurements the two surrogate model methods will be evaluated on the data set of the manufacturer.

The input data of the surrogate model needs to be organized to ensure a high accuracy. This includes: employing appropriate data splitting techniques, checking the distribution of the experimental points and possibly excluding regions of extreme values. [84] In figures 3.18 and 3.19 the *BSFC* and *Power* experimental data for the DA-35 engine are presented.

The regions for a throttle setting between 14.9% and 20% present significant increase in inclination of the plot, especially for the BSFC model. This behaviour however, is only modeled with very few data

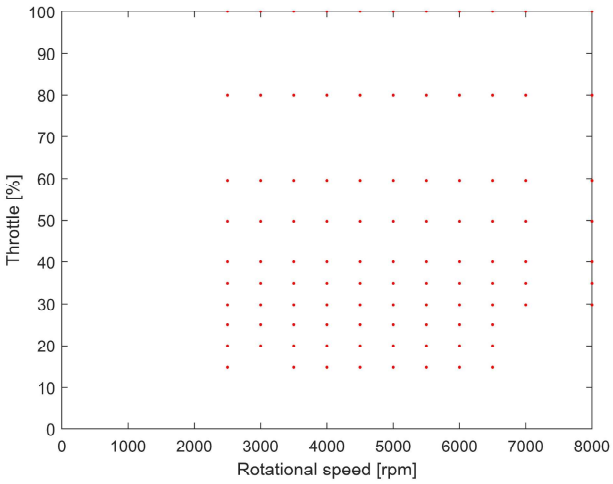


**Figure 3.20:** Distribution of the experimental test points

points as presented in figure 3.20, in the throttle direction, considering the changes in the results values ($\Delta z$). Due to this behaviour, the first considered data point of the model will be at throttle = 20% and rpm = 5000 to exclude these poorly mapped extreme regions and guarantee a satisfying accuracy of the model. Further the figure 3.20 presents the missing data points for a throttle setting of 70% and 90%. This lack of data will decrease the performance of the model in these regions too. The missing experimental data for a rpm setting of 7500 will have the same effect.

To split data sets the Cross-Validation (CV) method is often employed in machine learning processes to ensure a good generalization and avoid over-fitting of the model. The two most commonly applied CV methods are the Hold-Out CV and K-Fold CV. The Hold-Out CV will be applied in this work due to the simplicity of the implementation and its efficiency. The data splitting approach for the CV methods influences the bias[2] and variance[3] of the model and therefore its performance. Various splitting techniques like simple random sampling, systemic sampling or the more complex CADEX exist. Due to the uniformly distributed and low dimensional data set of the engine, the simple random sampling will be efficient and sufficient enough. [84] In [86] the prediction sum of squares vector *PRESS* is suggested as a performance parameter to make a decision between different surrogate model methods. This variable is an estimator for the root mean squared error (RMSE) and therefore a performance parameter of the model accuracy. The variable is defined in equation 3.21 in which *e* represents the the CV error and *p* is the total number of test points. A special version of the Hold-Out CV the leave-one-out CV is employed to obtain this error. In this approach, only one data point is left for the testing of the model and the error at this point is therefore the CV-error *e*. [86]

[2] bias is the tendency of the model to over- or under estimate the results [85]
[3] variance is the dependence of the estimated parameters on the training data [85]

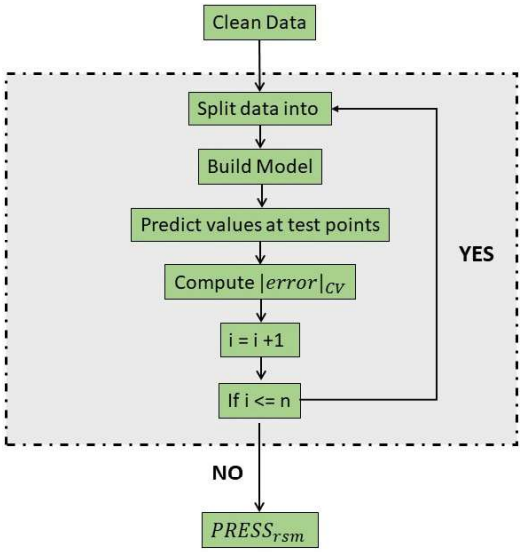


**Figure 3.21:** Flowchart of the $PRESS_{rsm}$ estimation

$$PRESS_{rsm} = \sqrt{\frac{1}{p} * e^T * e} \tag{3.21}$$

The evaluation of the different surrogate modeling techniques is performed according to the flowchart portrayed in figure 3.21. In the first step, the data is cleaned from the extreme values as already mentioned. Afterwards, the data is split with a simple-random-sampling technique according to the leave-one-out method. The training data set is used to build a surrogate model. The prediction for the test point is performed on the model and the CV error is computed. This process is repeated till $i$ equals the length of the data set $n$. At the end, the $PRESS_{rsm}$ can be obtained according to equation 3.21. This process is applied for both the Kriging and the different RBF methods.

The evaluation results are presented in table 3.7. Besides the $PRESS_{rsm}$ parameter also the computation times are measured. The RBF outperforms the Kriging method by a magnitude of $10^3$ for this parameter. On the other hand, the Kriging techniques provides much better results for both the Power and the BSFC model. Therefor, and because the computation time of the Kriging model is still low (taking only 4.42 seconds for $n$ iterations) this surrogate modeling technique is chosen to be implemented for the ICE model.

| | Kriging | RBF-TPS | RBF-MQ | RBF-IMQ | RBF-BH | RBF-G |
|---|---|---|---|---|---|---|
| Power | 23.62 | 87.34 | 85.71 | 479.15 | 94.86 | 583.30 |
| BSFC | 35.19 | 63.58 | 70.99 | 98.93 | 71.23 | 114.29 |

**Table 3.7:** $Press_{rsm}$ for the various surrogate model techniques for the Power and BSFC data sets

#### 3.2.4.D Formulation of the propulsion function

The chosen Kriging surrogate model can now be implemented into the combustion branch propulsion function *"GasPropulsionOneStep"*. This propulsion module consists of the *"propModel"*, *"CreatePowerModel"*, *"PowerPrediction"*, *"CreateBSFCModel"* and the *"BSFCPrediction"* function. The flowchart of the function is presented in figure 3.22. The two functions *"CreatePowerModel"* and *"CreateBSFCModel"* are standalone files and only have the experimental data of the DA-35 as an input. The final surrogate model is obtained in an identical scheme for the power and BSFC branch. Both times the data is split according to the leave-M-out method, the model is created and the prediction error is estimated with the test data set. The iterative process is performed as long as $i < n$, where *n* stands for the length of the data set. This step is necessary as the data splitting is done randomly and no control over the process is possible. Afterwards the set with the smallest error is chosen as the final model training set. The throttle setting of the combustion engine needs to be obtained prior to the BSFC determination. The surrogate power model is fed into the *"PowerPrediction"* function together with the rpm, determined by the *"propModel"*, and the current throttle setting from the throttle vector according to the position of the loop. An error is computed for each loop position and the throttle setting with the minimal error is chosen afterwards. This value together with the rpm and BSFC model are inputs for the *"BSFCPrediction"* function to determine the current BSFC value.

This structure of the *"GasPropulsionOneStep"* function is tested over 25 cycles to ensure that the randomness of the process is considered. The relative errors of the prediction regarding the throttle and BSFC values are presented in figures 3.23 and the 3.24. The throttle setting has a maximum over prediction of $\approx 12\%$ and a maximum under prediction of $\approx 8\%$. The BSFC approximation has an error interval from $\approx -9\%$ (over prediction) to $\approx 11\%$. The causes of these errors are the already mentioned poor distribution and low number ($\approx 100$) of design sites. The performance of the model could be significantly increased if additional experiments are performed on the ICE to obtain more data points. While these error values are not negligible, the model accuracy is still deemed feasible to be implemented into the whole UAV Framework. In the last step of the function, the fuel flow of the engine can now be obtained with equation 3.22 as all parameters are known by now. [76]

$$BSFC = \frac{\dot{m}_{fuel}}{Power} \tag{3.22}$$

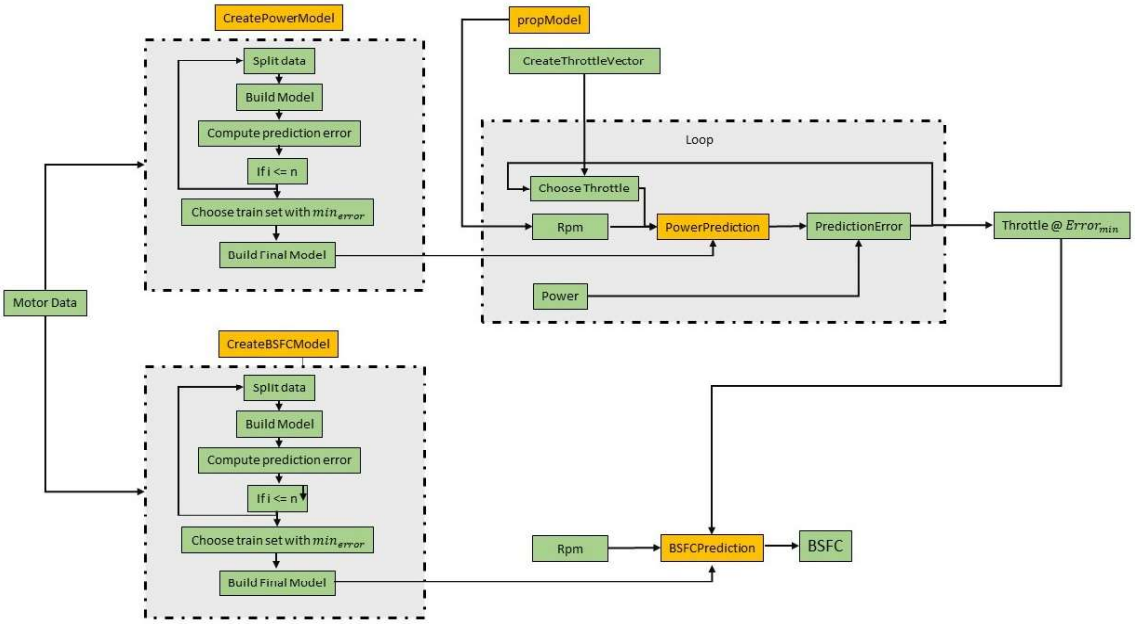


**Figure 3.22:** Flowchart of the *"GasPropulsionOneStep" function*

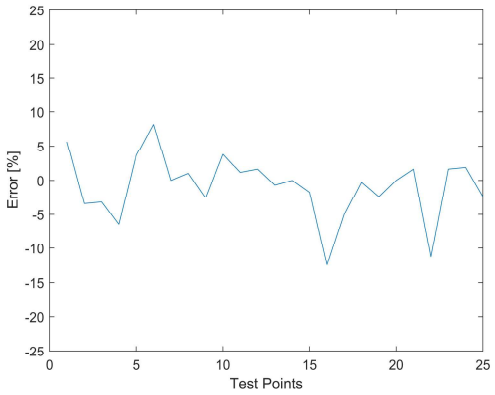


**Figure 3.23:** Relative error of the surrogate for the throttle prediction

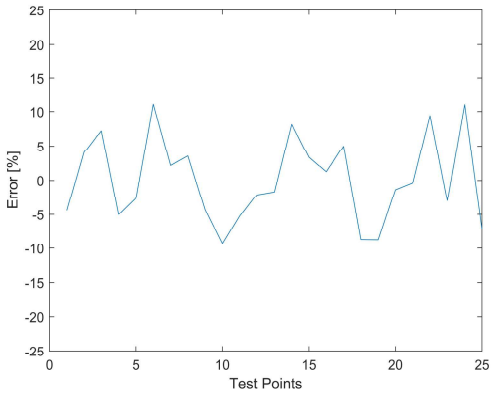


**Figure 3.24:** Relative error of the surrogate for the BSFC prediction

| Component | Efficiency [%] |
|---|---|
| Flywheel | 90 - 93 [87] |
| One-way-bearing | 95 [88] |
| Mechanical Coupling | 95 - 98 [89] |

**Table 3.8:** Efficiency approximations for hybrid propulsion components

## 3.3 Parallel Hybrid Test Bench evaluation

The single branches of the hybrid propulsion system described in the previous sections are now combined according to the test bench portrayed in figure 3.1a. The figure 3.25 illustrates the schematic layout of the hybrid test bench. The solid lines represent mechanical connections and dashed lines electrical connections.

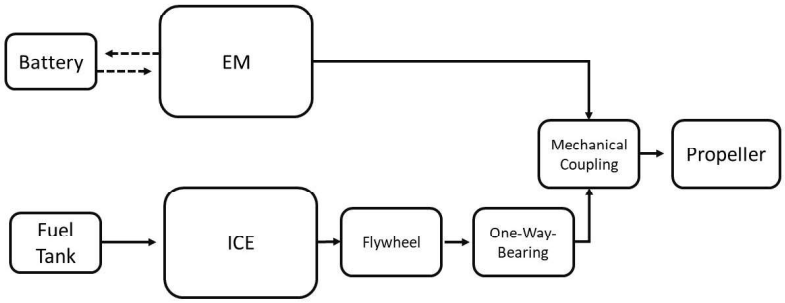


**Figure 3.25:** Components of the parallel Hybrid propulsion test bench

In the evaluation process, the EM only, ICE only, Dash and Regenerative brake modes are studied. Afterwards, it is possible to develop and integrate the complete propulsion module into the aircraft *Framework*. The extra components *Flywheel*, *One-way-bearing* and *Mechanical Coupling* are modeled as simple efficiency according to table 3.8.

### 3.3.1 EM only Mode

The first evaluated operational strategy of the parallel hybrid test bench is the stealth or EM only mode. For this process the throttle and current of the EM are studied. The structure for this system architecture is the electric motor model described in sub-section 3.2.3. The simulation results are assessed with the test results presented in [65], which are attached in table B.6 in the appendix.
The results of the simulation are visualized in figure 3.26 and 3.27, while the relative error for each

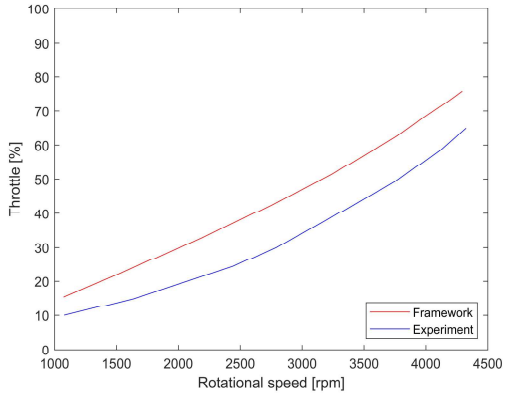


**Figure 3.26:** Throttle setting of the EM over the rotational speed for the *EM only* mode

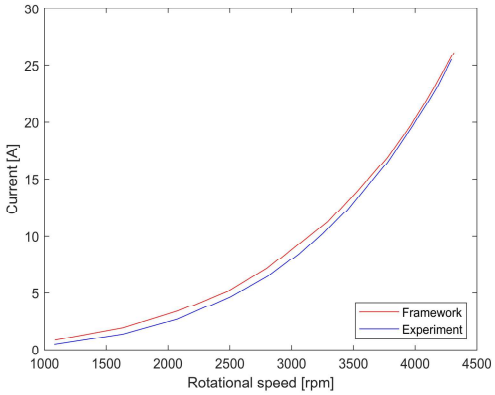


**Figure 3.27:** Current of the EM over the rotational speed for the *EM only* mode

test point is presented in table 3.9 in the appendix. In the analysis the test points above a rotational speed of 4650 rpm are, because afterwards the throttle setting increases significantly with only minor changes in rotational speed, discarded. This behaviour could be based on a malfunction of the ESC as explained in [65]. The modeling of this special scenario is deemed impracticable. The simulation of the throttle setting presents a similar trend to the experimental results. But the curve has an identical magnitude as for the propeller test bench, stated in figure 3.15, while in the *Hybrid Test Bench* the EM is able to draw more current from the battery for the same throttle setting. Due to this behaviour, the throttle settings is over predicted for all test points. The absolute error between the two curves is almost constant around $\approx 10\%$. In a second approach, the throttle was predicted with the definition in equation 3.25. [90] The maximum torque of the EM ($T_{max}$) depends on the rotational speed and voltage. The base for the definition are the manufacturer datasheets in the appendix of [65]. The results of this method are presented in figure B.1 and B.2 in the appendix. The outcome does not show any potential in comparison with the experimental data and is deemed to have a poor quality.

The trend of the current prediction is almost identical to the experimental results. While for small rotational speeds and throttle settings the relative error is fairly high around 40% it decreases fast with an increase in torque demand. From a rotational speed of $\approx 2500$ upwards the error is never above 10%. The greatest error range does not affect the SoC significantly, due to the small amount of current drawn from the battery. Additionally, the EM is the most efficient in the *Hybrid Test Bench* at high throttle settings and therefore the operating range of the EM should be set in this region. [65] The operating regions with the biggest impact on the SoC present accurate simulation results for the current. The prediction quality for this variable considering the mentioned circumstances is deemed good.

In overall, the *EM only* mode of the simulation *Framework* provides satisfying results despite some non-neglectable errors. The error for the throttle prediction could be eliminated with a correction factor to

| Thrust [N] | Throttle | Current |
|---|---|---|
| 1.36 | -53.61% | 41.18% |
| 3.60 | -58.80% | 28.08% |
| 6.45 | -54.03% | 20.89% |
| 10.04 | -49.60% | 14.45% |
| 13.23 | -44.03% | 9.89% |
| 17.32 | -35.90% | 8.92% |
| 21.60 | -28.85% | 10.64% |
| 23.97 | -23.55% | 12.23% |
| 26.54 | -24.69% | 3.64% |
| 29.12 | -21.68% | 3.17% |
| 31.92 | -19.27% | 3.16% |
| 34.55 | -16.32% | 2.22% |
| 37.52 | -14.63% | 1.12% |
| 40.67 | -13.94% | 0.57% |
| 40.98 | -8.17% | -0.04% |
| 41.11 | -2.69% | -0.26% |
| 43.38 | -1.40% | -1.44% |

**Table 3.9:** Relative error of the simulation for the corresponding required thrust values

ensure better quality for this performance variable. The ranges with significant challenges in the current prediction are considered to be of minor importance due to the operational conditions of the UAV. The complexity to model the interactions of the various components in the *Hybrid Test Bench* already start to emerge in this mode.

### 3.3.2 ICE only Mode

In this section, the performance of the *Framework* is evaluated for the *ICE only* mode of the test bench. The main performance characteristics in this process are the fuel flow measurement and the throttle setting of the ICE. As outlined in sub-section 3.2.4.C, the fuel flow results of the engine in [65] are not considered to be accurate due to the decrease in fuel flow with a higher throttle value. A new measurement series was performed at CfAR with a bigger fuel tank. Through this upgrade the quality of the fuel flow measurement could be increased as the operating duration of the engine is extended. Therefore, oscillations in rotational speed and power output could be equalized with an averaging strategy. The results for this measurement series are presented in table B.7 in the appendix.

In figure 3.22, the flowchart for the combustion branch is presented. This chart is the basis for the evaluation process. The surrogate model described in sub-section 3.2.4 is based on a raw power measurement table. Therefore, these values need to be corrected to the altitude and temperature which the UAV is flying in as presented in equation 3.23 according to the *SAE J1349 standard*. A simplified version of the correction factor is defined in equation 3.24. In the formula $p_a$ and $T_a$ stand for the ambient pressure and air temperature, while $p_0$ and $T_0$ are reference values. [91] These reference values are set at $p_0 = 0.99$bar and $T_0 = 302.4$K.

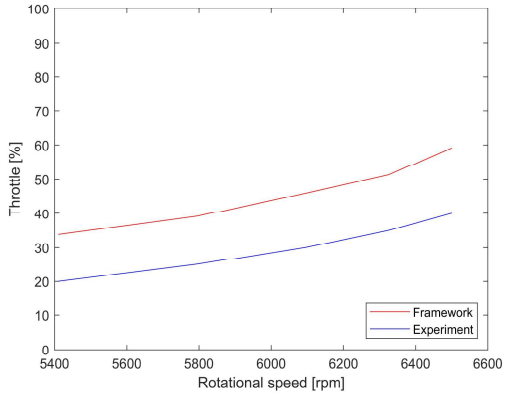


**Figure 3.28:** Throttle setting of the ICE over the rotational speed for the *ICE only* mode

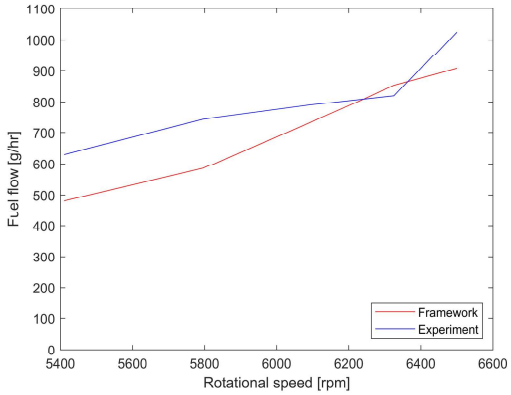


**Figure 3.29:** Fuel flow of the ICE over the rotational speed for the *ICE only* mode

$$P_{raw} = \frac{P_{shaft}}{C_f} \tag{3.23}$$

$$C_f = \frac{p_a}{p_0} * \frac{T_0}{T_a}^{0.5} \tag{3.24}$$

The ambient conditions are computed according to the standard atmosphere. [92] The power flow along the branch needs to consider the three efficiencies presented in table 3.8. The results of the simulation are presented in table 3.10 and shown in figures 3.28 and 3.29. The throttle setting presents a constant absolute error of roughly $\approx 15\%$. By inspection of the data in table B.4 the manufacturer was not able to operate the engine at throttle values smaller than 14.9%. At CfAR the pin controlling the throttle valve of the DA35 was adjusted to guarantee workable conditions also for lower settings. The linearity of the error combined with this adjustment could explain the error of the *Framework*.

Regarding the second parameter, the fuel flow, it is possible to identify different regions of accuracy. For rotational speeds below $\approx 5700$rpm, the curves present the same trend with a relative error of $\approx 28\%$. While the *Framework* predicts an increase in inclination afterwards, the experimental results suggest the opposite behaviour. The error though starts decreasing down to values between 4 to 10%. It is important to note that the fuel flow measurement was performed outside. While precautions were taken to not operate the engine on extremely hot or windy days the environmental influences could still have a big impact on the test results. The surrogate model on the other hand is based on data from experiments in a controlled indoor environment. Therefore, the deviations between the two results are natural.

Overall, the ICE only mode predictions of the *Framework* are considered to be satisfying in comparison to the measurement series performed at CfAR. The database for the surrogate model would need to be corrected with a linear factor to account for the performed throttle pin adjustment. Due to the high complexity of the combustion process the results, with a peak error of 30% for the fuel flow which decreases

| Thrust | Rpm | Throttle [%] | Power [Nm] | Fuel Flow [g/hr] |
|---|---|---|---|---|
| 56.96 | 5410 | 33 | 1028.66 | 481.65 |
| 64.96 | 5795 | 39 | 1260.37 | 585.32 |
| 72.61 | 6095 | 46 | 1478.04 | 733.13 |
| 77.69 | 6325 | 51 | 1649.66 | 853.64 |
| 82.50 | 6500 | 59 | 1796.74 | 907.65 |
| 85.33 | 6615 | 66 | 1895.59 | 1044.81 |

**Table 3.10:** Results of the ICE only simulation of the Hybrid Test Bench

| Dash | | Regenerative Brake | |
|---|---|---|---|
| ICE Thottle | EM Throttle | ICE Thottle | EM Throttle |
| | 0% | | 0% |
| | 10% | | -10% |
| | 20% | | -20% |
| 40% | 30% | 60% | -30% |
| | 40% | | -40% |
| | 50% | | -50% |
| | 60% | | -60% |

**Table 3.11:** Throttle settings for the *Dash* and *Regenerative Bake* modes of the *Hybrid Test Bench*

for high rotational speeds, are still considered to be acceptable for the *Framework* implementation.

### 3.3.3 Dash and Regenerative Brake mode

The evaluation of the *Dash* and *Regenerative Brake* modes is the last step in the assessment of the *Framework* with results from the *Hybrid Test Bench*. These modes present the most complex operating strategies due to the interactions between the two power sources. For both modes the ICE throttle setting is set at a predefined value, while the EM throttle value is swept from low to high values. The focus of this assessment is again on the current and throttle setting of the EM and the throttle of the ICE as no measurement for the fuel flow exist. The experimental results are presented in the appendix in tables B.8 and B.9.The throttle setting combinations evaluated in this section are presented in table 3.11.
In order to operate these modes, the two already described modules *"ElectricPropulsionOneStep"* and *"GasPropulsionOneStep"* are employed. At the start of the process, the necessary torque output of the propeller for the thrust request is computed with an intermediate calculation through the *"ElectricPropulsionOneStep"* function. The first operating point represents the torque supplied by the ICE as the EM throttle is 0%. In the other test points, additional required/excessive torque is provided/absorbed by the EM depending on the mode (*Dash* and *Regenerative Brake respectively*). The delta torque at the propeller $\Delta Torque_{Prop}$ and at the EM $Torque_{EM}$ do not follow the same trend for the experimental results as presented in figure 3.30. The behaviour indicates the oscillation of the ICE torque output even for a constant throttle over the rpm. This will influence the accuracy of the results as the ICE torque is constant in the simulation file.

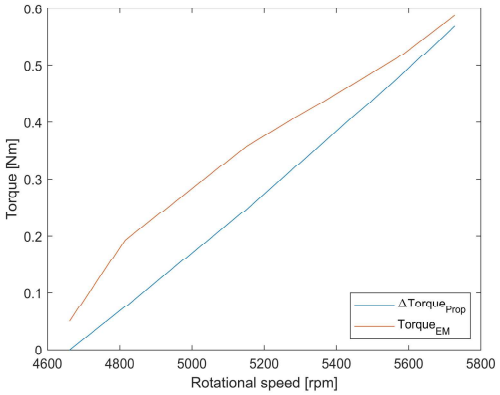


**Figure 3.30:** Torque over the rotational speed of the *Dash* mode

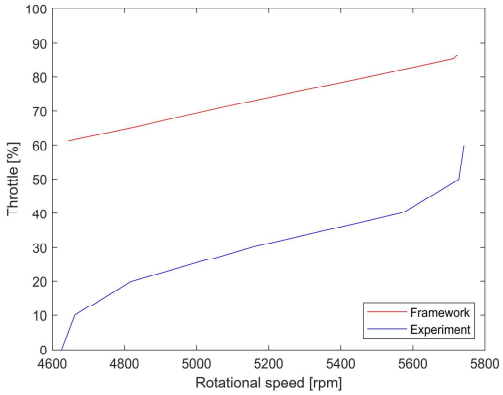


**Figure 3.31:** Throttle of the EM over the rotational speed for the *Dash* mode with equivalent circuit

Through the coupling of the ICE and the EM in the *Hybrid Test Bench*, the equivalent circuit as described in equation 3.16 for the EM is not applicable anymore. In this equation the rotational speed of the shaft is directly connected to the throttle setting of the EM. Therefore, the system neglects the extra provided torque of the ICE and fiercely overpredicts the EM throttle value. In figure 3.31 the results for the throttle setting are presented, if this relation would still be employed. Through the high rotational speed of the system, the simulation model would predict the throttle setting around $\approx 60\%$ at the first test point. But at this stage the ICE provides all the power. Therefore, this approach is deemmed unsuccessful.

Due to this behaviour the structure of the *"ElectricPropulsionOneStep"* function is changed to better match the results of the *Hybrid Test Bench*. In the new version, the current is obtained with equation 3.12. Furthermore the throttle setting can be determined according to Greisner in [90] with equation 3.25.

$$Throttle = \frac{Torque}{Torque_{max}} \tag{3.25}$$

The according throttle prediction is presented in figure 3.32. In this graph two predictions are illustrated: first are the results according to equation 3.25; and second are the throttle results corrected according to the throttle error briefly mentioned at the end of sub-section 3.3.1. This corrected version preforms worse for the *Dash* mode and is thus neglected. From the figure the incapability of the model to predict the exponential regions for low and high throttle values is obvious. For the first test point a high error of 60.73% is obtained while it drops to more acceptable deviations around 5-14% for the later operational points. The range from $\approx 5700$ rpm upwards could though be affected as already mentioned by a malfunction of the ESC. Therefore, this region proves itself very hard to model.

The results for the current of this approach are presented in figure 3.34. The prediction curve directly follows the obtained torque at the EM ($T_{EM}$), illustrated in figure 3.33, as expected. The simulation is

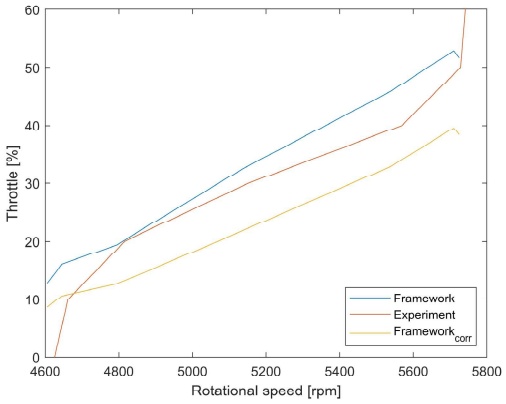


**Figure 3.32:** Throttle of the EM over the rotational speed for the *Dash* mode

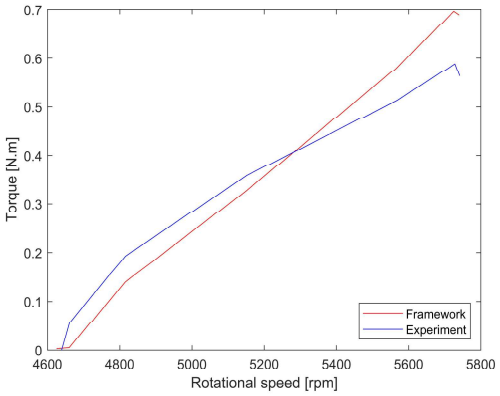


**Figure 3.33:** Torque of the EM over the rotational speed for the *Dash* mode

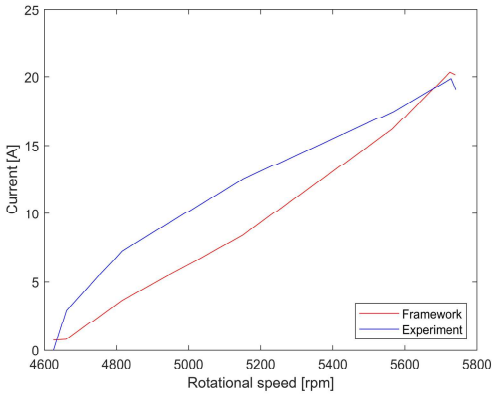


**Figure 3.34:** Current of the EM over the rotational speed for the *Dash* mode

not capable to model the non-linear increase in torque for throttle settings below 20-30% of the EM. This behaviour suggests the incapability of the EM to efficiently provide power to the system for low throttle settings. Therefore, a higher amount of current is drawn from the battery as explained in sub-section 3.3.1. This incapability results in a relative error around 40 - 50% for the non-linear region. The error marginalizes down to values between +5 to -5% for higher throttle settings. As already mentioned these operational settings will affect the SoC of the battery the most and the accuracy in these regions is therefore the most important characteristic of the prediction.

Overall, the results for the *Dash* mode need tuning but the various influences as the changing torque output of the ICE and malfunction of components make the reproduction of the experimental results very difficult. Further, the regions of ineffective operations for the EM should be explored in more detail. Still, the model provides an appropriate approximation of the experimental tests and can be implemented in the UAV *Framework* with care. To conclude, an overview of the relative errors for each operational point

| $Throttle_{EM}$ | Prediction Error | |
|---|---|---|
| | Throttle | Current |
| 10% | 60.73% | 50.95% |
| 20% | 2.91% | 44.74% |
| 30% | 8.22% | 17.98% |
| 40% | 14.86% | 2.19% |
| 50% | 5.86% | 0.53% |
| 60% | 13.79% | -6.23% |

**Table 3.12:** Relative error for the throttle and current prediction of the EM in *Dash* mode

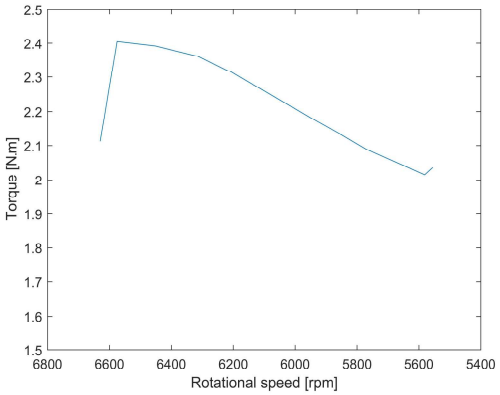


**Figure 3.35:** Experimental torque output of the ICE over the rotational speed for the *Regenerative Brake*mode

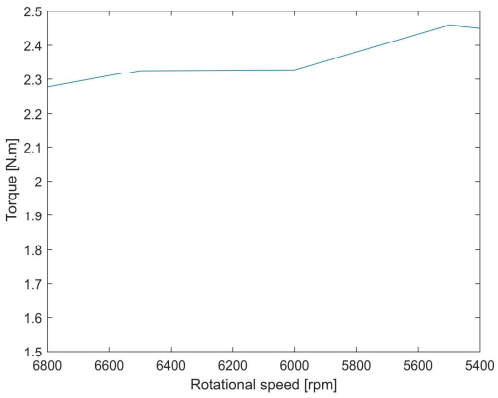


**Figure 3.36:** Torque output of the ICE over rotational speed according to DA-35 Database

of the experimental are presented in table 3.12.

After *Dash* also the *Regenerative Brake* mode needs to be validated. The according operational settings for both power sources are displayed in table 3.11. The variation in torque output of the ICE over the rotational speed is bigger for this mode than in *Dash*. This behaviour of the ICE is proven in [65] and presented in figure 3.35 as a results from post-processing of the measurement variables. Further, the torque according to the database of the DA35 for a throttle setting of $\approx 45\%$ over the same rotational speed range shows a very different characteristic as stated in figure 3.36. As already stated earlier in this work, the throttle value of $\approx 45\%$ is chosen due to the adjustment of the throttle pin in relation to the database at the ICE. Therefore, neither the recreation of the experiment with a constant torque of the first operating point nor a constant throttle setting for the ICE seems to provide good input data and the mode is going to be validated with a simplified simulation.

In this process the experimental results for the torque of the EM ($T_{EM}$) are chosen as inputs of the system to neglect the variations of the ICE. The focus is on the current of the EM, voltage of the battery and the throttle setting of the EM. In figure 3.37 the increase of the battery voltage from high to low rpm settings is presented. The magnitude of the results show variations due to different starting voltages.

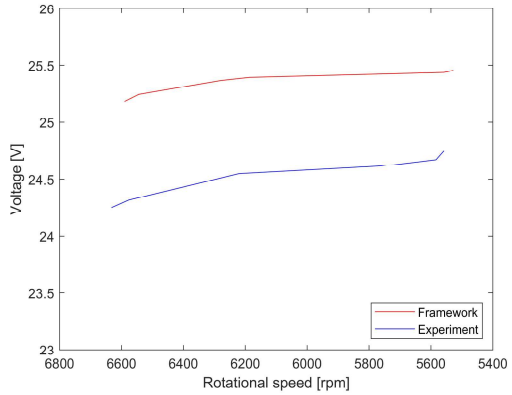


**Figure 3.37:** Battery voltage over the rotational speed for the *Regenerative Brake* mode

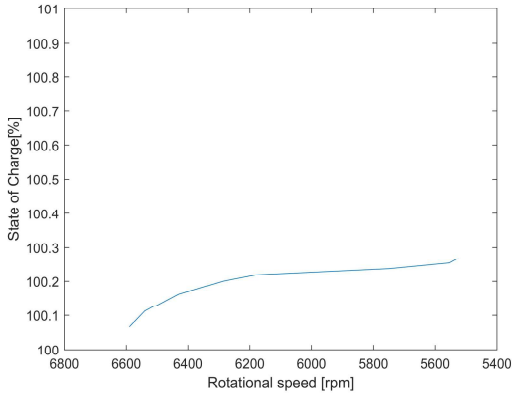


**Figure 3.38:** SoC of the battery over the rotational speed for the *Regenerative Brake* mode

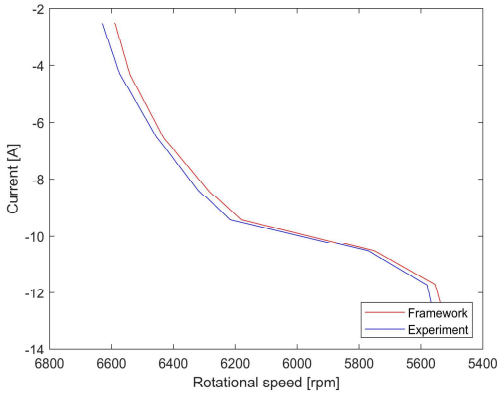


**Figure 3.39:** Motor Current over the rotational speed for the *Regenerative Brake* mode

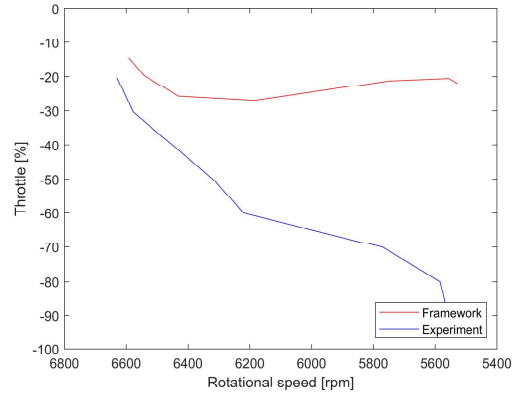


**Figure 3.40:** Throttle of the EM the rotational speed for the *Regenerative Barke* mode

But the trends of the curves present an accurate solution, which is the most important outcome for this parameter. The increase in voltage also leads to a rise of SoC as shown in figure 3.38. Therefore, the *Regenerative Brake* mode is clearly operating correctly as the battery is being charged.

In figure 3.39 the current curves of the EM are presented for this experimental structure. The trend of the simulation results and also the magnitude shows a good correlation with a maximum relative error of only $\approx 10\%$. This result is expected as the current directly depends on the torque of the EM ($T_{EM}$) and this variable is fed into the model. On the other hand the throttle prediction according to Greisner, presented in figure 3.40, does provide very poor results. The throttle setting increases very slowly before it starts to decrease and later stabilizes around 20%. The presented behaviour is due to the fast increase in maximum available torque with the decrease in rotational speed as presented in figure B.1 in the appendix. The slow increase of the EM torque ($T_{EM}$) presented in table B.9 leads to low throttle

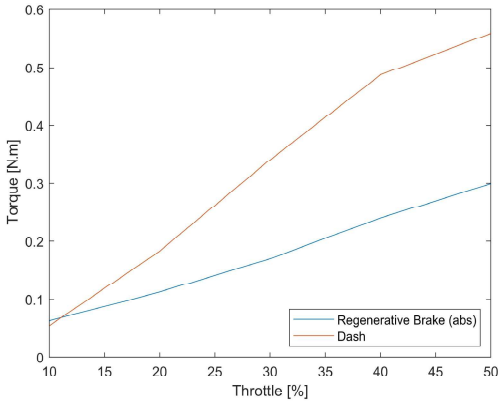


**Figure 3.41:** Torque of the EM over the throttle setting for the two hybrid modes

settings.

In the *Dash* mode the EM is able to draw more current for the same throttle setting than in the *Regenerative Brake* mode. This behaviour leads to higher torque outputs of the EM as presented in the experimental data based figure 3.41. [65] Higher torque outputs result in higher throttle settings as shown in equation 3.25. The throttle definition according to Greisner achieves accurate results in the *Dash* but not the *Regenerative Brake* mode due to this characteristic.

In the evaluation process of the *Regenerative Brake* mode the challenges already mentioned in the *Dash* mode simulation continue. The changing torque output of the ICE is more drastic and leads to a necessary simplified simulation to achieve results with good quality. The two important performance characteristics, the current of the EM and the voltage of the battery, are predicted correctly. On the other hand, no satisfying simulation results regarding the throttle setting of the EM for the *Regenerative Brake* mode was obtained. This variable needs further investigation but it does not influence the performance of the UAV model and is only an analysis variable. Therefore, the decision to continue the *Framework* with the current state simulation is justified.

# 4

# Parallel Hybrid UAV Simulation Model

## Contents

In this chapter, the complete simulation model for a parallel hybrid propulsion system, based on the component models of chapter 3, is developed. In the first step, an energy management strategy and the propulsion system controller is designed. This controller is then combined with the component models to obtain the whole propulsion system module. The propulsion module can be implemented into any aircraft configuration with the CfAR *Framework* described in section 3.1 for evaluation purposes.

## 4.1 Energy Management Strategy

The implemented energy management strategy for the hybrid propulsion system should maximizes the performance of the UAV while increasing fuel economy and decreasing the emissions of the UAV. In the design phase of the strategy various considerations need to be taken into account. These include, the optimal operating point of the engine, the minimum engine speed, engine turn-on turn-off frequency, proper battery capacity and maximum battery charge current. [93] Propulsion system controls can be classified in the two distinct groups of *rule-based strategies* and *advanced control algorithms*. In the work by Wall in [94] an extensive review of various control strategies is presented. The simple rule based control has been successfully implemented in both automobile and UAV systems. Strategies like fuzzy control and artificial neural networks correspond to more sophisticated approaches which have the potential to increase fuel efficiency and the performance of the power train. [21] Especially the fuzzy control logic has gained popularity in the last few years and shows great potential to increase fuel efficiency. This strategy was implemented by researches in various projects for example [95] [96]. In this work, the rule based control approach is chosen due to the already successful implementation and its reliability.

Parallel hybrid propulsion system can be designed with and without an engine transmission. The hybrid test bench presented in figure 3.25 follows the definition of [16] and simply couples the two power flow paths with a mechanical device (presented in sub-section 4.1.1). The more sophisticated approach is presented in figure 4.1 and is according to [97]. In this design, a transmission is included to decouple the rotational speed of the propeller and the engine (presented in sub-section 4.1.2). Therefore, the engine can operate at its most efficient point for the power request. An energy management strategy for both designs will be explored in this section.

### 4.1.1 Classic parallel hybrid

The classic configuration has no transmission and therefore this hybrid system is lighter and less complex. But through the missing component the rotational speed of the propeller and the engine are identical. Further, the propeller rotational speed is set by the required thrust for the current flight phase. Therefore, it is not possible to operate the engine at its most efficient point as the power output of the

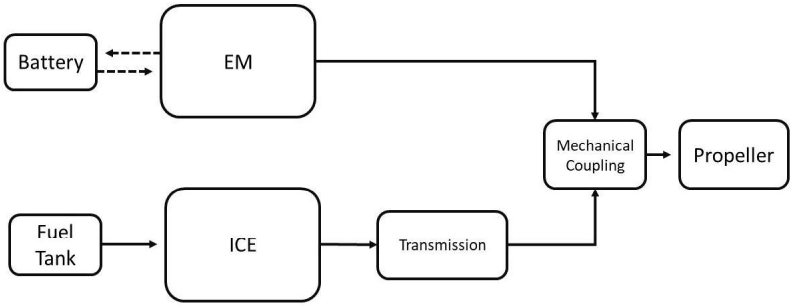


**Figure 4.1:** Function scheme of a parallel hybrid with an engine transmission

| | Power$_{ICE}[W]$ | Power$_{EM}[W]$ | Fuel Flow [g/s] |
|---|---|---|---|
| Baseline (red) | 536.16 | 0 | 0.0871 |
| Discharge(green) | 502.65 | 33.51 | 0.0847 |
| Charge(yellow) | 578.05 | -41.88 | 0.0904 |

**Table 4.1:** Results for the engine map presented in figure 4.2

ICE, and its speed are prescribed and so the supplied torque is set. The operating point of the ICE on the engine map is therefore determined and can not be varied in terms of rotational speed. In this work, there will be no energy management strategy implemented for the classic configuration.

Still, the author developed a concept on how to manage the energy sources with the help of a *smart controller* which will be briefly outlined in this section. For the energy management system an online optimization process is necessary. Therefore, a cost-function is designed which includes the following parameters: rotational speed, SoC of the battery, power request, remaining fuel load and the current BSFC region. In this concept, the rotational speed is still set by the propeller but the torque output of the engine can be varied according to the cost function. This is especially interesting in regions with a significant change in the BSFC value of the operating point with only small changes in torque output. In figure 4.2 an example, in which the red point represents the power request by the propeller, is provided for this control strategy. Due to a high remaining fuel load, a low SoC and a more efficient operating point for a higher torque output, the engine could exceed the power request and start charging the battery (yellow operating point). On the other hand, the controller could lower the torque output as the fuel load of the UAV is low but the SoC of the battery still high (green operating point). The results, presented in table 4.1, could lead to the choice of the charging strategy as the fuel flow only increases by $\sim 4\%$ while the power output increases by $\sim 8\%$. The concept is still in an very early stage but the author believes it has potential to achieve a more efficient energy management for this parallel configuration.

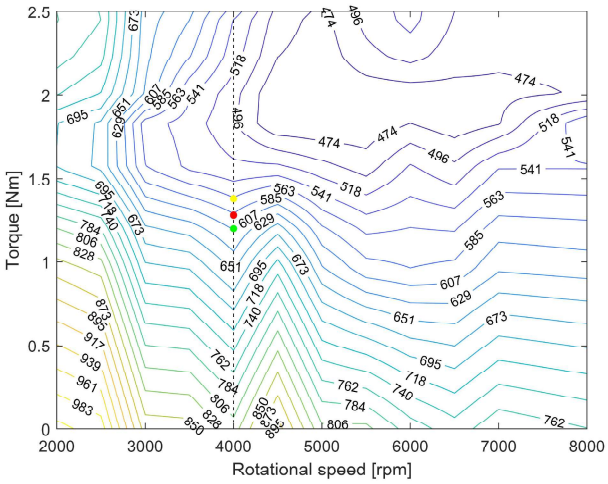


**Figure 4.2:** Engine Map for the DA-35 engine (25 BSFC contours) and smart controller operating points

### 4.1.2 Engine transmission parallel hybrid

The propulsion system is structured as presented in figure 4.1 and has a higher complexity due to the transmission as an extra component. But it also provides the advantage of decoupling the engine and propeller rotational speed. Therefore, it is possible to apply the *Ideal Operating Line (IOL)* theory as an energy management strategy.

The engine transmission is modeled as a continous variable transmission with 95% efficiency. [98] The IOL of an engine is the smooth line made up of all points which represent the torque and rpm combinations at which the fuel consumption is minimal for different power levels. Theoretically, this strategy would enable the best performance of the ICE while being operated at its most efficient point. [17] The data points provided in the table B.3 are not sufficient to perform an IOL analysis. Therefore, additional data is obtained with the surrogate models described in sub-section 3.2.4. For this purpose, the surrogate models are run with a rpm and throttle vector from 2500 to 8000rpm and from 20 to 100%, respectively. The extra data enables the determination of the IOL. Thus an engine map, which analyzes the performance of the ICE in terms of rpm and its torque output, is necessary. The operating points with a constant BSFC value are plotted as contour lines on the map as presented in figure 4.4. Further constant power lines for various rpm and torque settings are obtained as visualized in figure 4.3. The number of contour lines in figure 4.4 and 4.3 is reduced compared to raw data for illustration purposes.

The intersection between each constant power line and the corresponding lowest possible BSFC contour is a IOL data point. In figure 4.5 all IOL points are plotted on the engine map. In this figure also the number of BSFC contour lines is reduced for presentation purposes while the intersections are computed with a more dense mesh. In flight phases of low power demands like cruise or loiter the engine is most

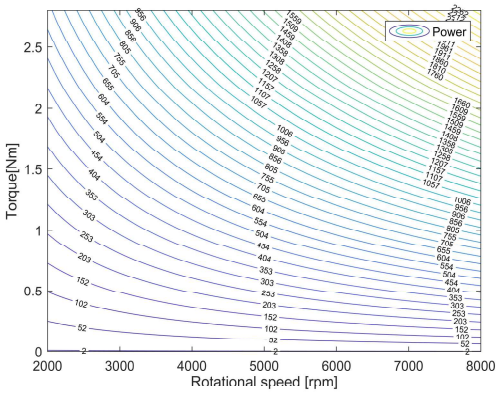


**Figure 4.3:** Power as a function of rpm and torque for the DA35 engine

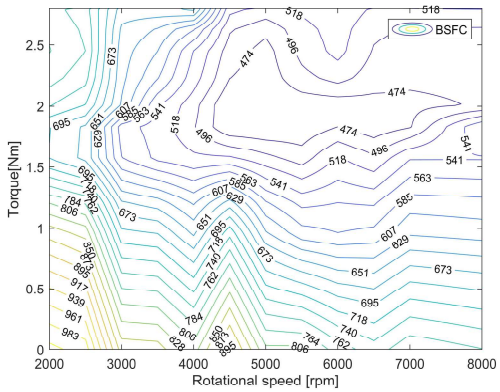


**Figure 4.4:** BSFC as a function of rpm and torque for the DA35 engine

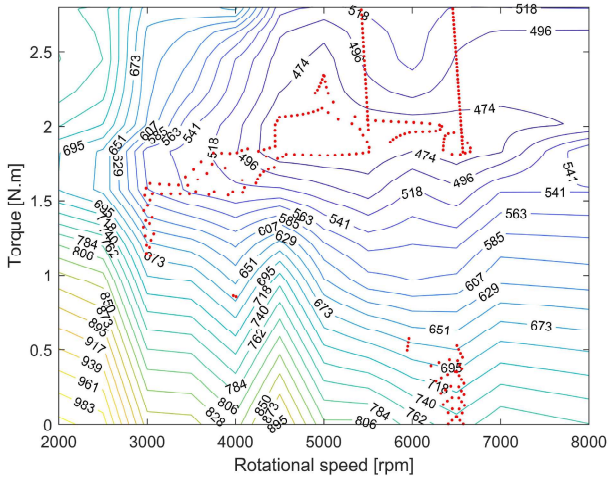


**Figure 4.5:** IOL data points from the constant power and constant BSFC graphs

efficient for high rotational speeds and low torque settings (Torque $<=$ 0.7Nm). In climb on the other hand the power demand is high and the engine will be operated at higher torque outputs (Torque $>$ 0.7Nm). The greater the power request the greater the rotational speed will be in this region. Various researches fit a polynomial regression through the scattered points to obtain a smooth IOL. [17] [65] But the distribution of the data points for the DA-35 engine would at least require two different regressions. Those two regressions still provide poor fitting quality with a R-Squared value of $\approx 35\%$ for the low power and $\approx 60\%$ for the high power region. Therefore, this approach is deemed not feasible and the interpolation method is applied to identify the operational point depending on the power request by the engine. This step is performed in the *IOLEngine* function with the power request as the only input to obtain the torque, speed and BSFC value for the power request.

| Mode | ICE | EM | Current |
|---|---|---|---|
| Normal | $P_{opt}$ | $P_{req} - P_{opt}$ | $> 0$ |
| Fuel saving | $0.8 * P_{opt}$ | $P_{req} - 0.8 * P_{opt}$ | $> 0$ |
| Dash | $P_{EMmax} - P_{req}$ | $P_{EMmax}$ | $> 0$ |
| Charge | $P_{opt}$ | $P_{req} - P_{opt}$ | $< 0$ |
| Stealth | - | $P_{total}$ | $> 0$ |

**Table 4.2:** Characteristics for the operating modes of the UAV propulsion system

| SoC | Value [%] |
|---|---|
| Optimal | 60 - 85 |
| Min | 15 |
| Max | 95 |

**Table 4.3:** Operating limits for the SoC of the battery

## 4.2 Controller Design

The propulsion system controller is an integral component of a hybrid electric vehicle. It manages the various propulsive components (the EM, ICE and battery) in order to achieve maximum vehicle efficiency. [17] The unit is coupled with the energy management strategy developed in section 4.1 and the various component models described in section 3.2. The controller is an adaptation from a simulation model developed at CfAR. [66]

The controller is identical for both parallel hybrid propulsion configurations described in the previous section besides the non IOLs existing points of the engine in the non transmission version. The *"parallelHybridMode"* file defines the controller and is called through the *"parallelHybridModeSelect"* function. The controller is rule based with the predefined operating modes *Dash*, *Normal*, *Fuel saving*, *Stealth* and *Charge*. The key characteristics of each operating strategy are summarized in the table 4.2. The optimal power request $P_{opt}$ is based on the mean power demand for an electric only mission while the required power of the flight phase is presented with $P_{req}$. The optimal variable is integrated to avoid acceleration and deceleration processes of the engine. In the description, a positive current symbolizes a discharging process while during a negative current the SoC of the battery increases. The battery should be operated considering the limits and ranges presented in table 4.3, which are already embedded in the controller. If the maximum or minimum battery charge levels are exceeded the unit could be damaged or not enough power is available for a necessary emergency landing due to ICE failure. The flowchart of the control process is presented in figure 4.6. It is a closed loop and starts for each time-step at the top of the decision tree. The decision parameters for the mode choice are the required power for the flight segment $P_{req}$, the optimal power request $P_{opt}$ and the SoC of the battery. The paths with two arrows symbolize a continuous test loop to guarantee the condition is still fulfilled. The *Dash* mode represents the highest power output, as presented in table 4.2, and energy consumption of the UAV for segments with aggressive climb angles for example. In the *Normal* operating strategy the ICE

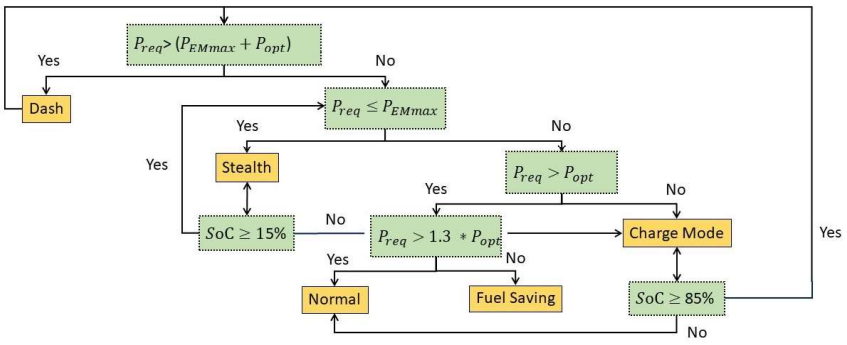


**Figure 4.6:** Flowchart of the parallel hybrid propulsion controller

runs at the optimal power request $P_{opt}$ and the remaining necessary power is supplied by the EM. If the demanded power is lower than 1.3x the optimal power request, the engine is decelerated to only operate at 0.8x the optimal power request in the *Fuel saving* mode. Therefore, this mode is significantly more fuel efficient than the *Normal* mode. The *Stealth* mode is the most eco-friendly as only the EM powers the UAV. All four strategies lead to a decrease of the SoC varying in magnitude on the according mode. The last strategy, the *Charge* mode is feasible if the ICE operated at the optimal power request exceeds the power requirement $P_{req}$ and the SoC of the battery is below the maximum charge level. Then the extra supplied power of the engine will be converted by the EM into electric energy to charge the battery.

## 4.3 Propulsion Module

The complete propulsion module for the parallel hybrid propulsion system consists of the two functions the *"parallelHybridModeSelect"* and the *"parallelHybridMode"*. These two files are implemented into the whole aircraft *Framework*. The flowchart to simulate this type of propulsion system for one time-step is presented in figure 4.7.

The initial inputs for the module are the required thrust for the current flight segment as well as the aircraft characteristics defined in the according class. Afterwards, in an intermediate step the *"propModel"* function defines the rotational speed of the propeller and the required power for the current flight segment. Therefore, the controller in the *"parallelHybridMode"* file can choose the mode the UAV should be operated in according to the power requirement. In section 4.2 the five operating modes *Dash*, *Normal*, *FuelSaving*, *Stealth* and *Charge* are already explained. The structure of the four modes with engine involvement is identical and therefore will only be described once. The *"IOLEngine"* function determines the torque output $T_{IOL}$, the rotational speed of the engine $rpm_{engine}$, the BSFC value for the operating point and therefore also the fuel flow $FF$. This result is then used as an input to the *"gasPropulsionOneStep"* file to determine the throttle setting $Thr_{ICE}$ for the necessary required power. The remaining

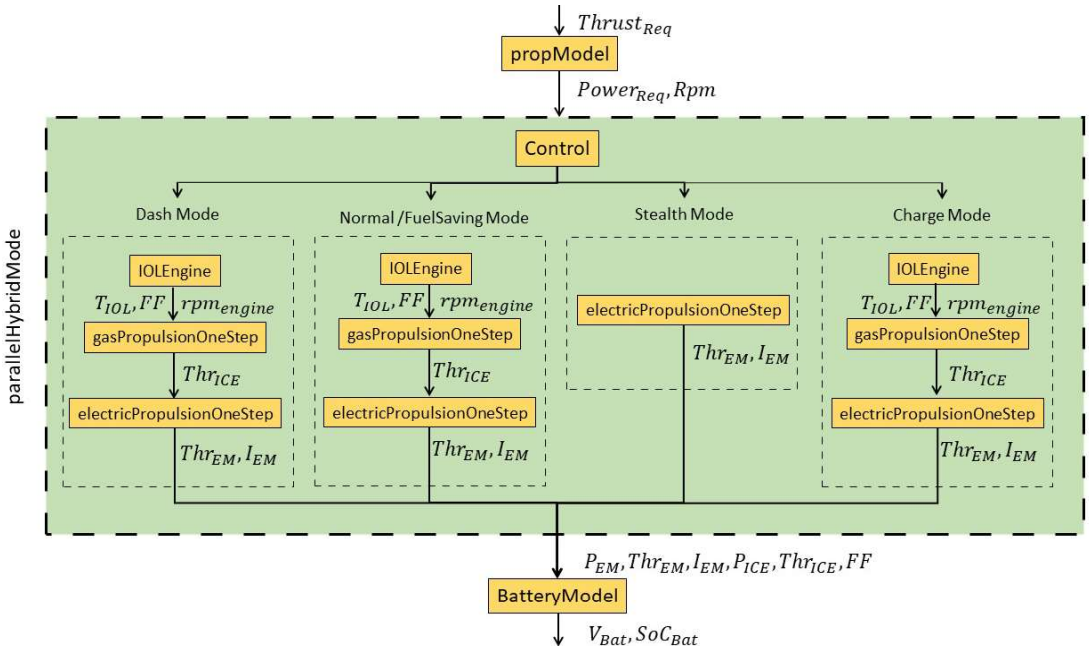


**Figure 4.7:** Flowchart of the *parallelHybridModeSelect* function

necessary torque is the input for the *"electricPropulsionOneStep"* function to determine the according performance parameters for the EM. If the control does select the *Dash* mode the power required by the ICE is determined with equation 4.1, where $P_{EMmax}$ represents the maximum available power by the EM. The stealth mode represents the most simple operating strategy as only the EM powers the UAV and therefore *"electricPropulsionOneStep"* function is sufficient to model the propulsion system. In all modes, the *"BatteryModel"* is included to compute the SoC of the battery according to the current flow during the timestep.

$$P_{ICE} = P_{req} - P_{EMmax} \tag{4.1}$$

# 5

# Mission Performance Analysis

## Contents

| | Value | Unit |
|---|---|---|
| Flight altitude | 300 | [m] |
| Target distance | 50 | [km] |
| Climb angle | 2-15 | [°] |
| Descent angle | - 5 | [°] |

**Table 5.1:** Surveillance mission characteristics

In this chapter the different propulsion system architectures developed previously are going to be evaluated as part of a mission analysis. Therefore, this chapter represents the final step in the performance analysis of the propulsion system models. First, a realistic verification mission for the UAV is designed. Afterwards, the aircraft characteristics of the UAV configuration are provided. These were already determined in a separate research effort at CfAR. In the last step, the performance of the EM only, ICE only and Hybrid propulsion strategy are going to be studied for the mission. The results outline the advantages and disadvantages of each propulsion configuration.

## 5.1 Mission Profile

UAVs with small Take-off weights are widely employed for surveillance and intelligence missions in both the civil and the military sectors. In the military frame enemy targets should be identified and hostile airspace can be patrolled without risking lifes of soldiers. [99] While in the civil sector these mission could include traffic or agricultural surveillance. [100] [101] Due to this wide spread mission type and the aircraft characteristics of the research UAV by CfAR, described in section 5.2, the performance analysis of the propulsion system architecture will be completed with a surveillance mission. This mission type requires a long endurance and range of the aircraft.

The mission profile of a surveillance mission is modeled with five flight segments. First, the aircraft climbs to the prescribed altitude and then dashes out to the target region. Once the UAV reaches this location it starts collecting information, while loitering above the target. As soon as the energy level of the UAV is below a set value, which guarantees a safe journey back to the base, it stops the loiter segment and dashes back. In the last phase, the aircraft descents to the airfield. No operational restraint for any segment will be set in this analysis. The key characteristics of the baseline mission are presented in table 5.1.

The mission is defined in the MATLAB script *"SurveillanceMission"*. This script includes three MATLAB functions to model each flight segment. These functions are implemented in the superclass file *"AircraftStep"* and the characteristics are presented in table 5.2. All functions are operated with a function specific predefined timestep $\Delta_{time}$. The equations of motion for the aircraft during the climb segment are described with a steady, unaccelerated climbing flight according to [102]. Further, the segment is characterized by the climb angle "$\gamma_{climb}$" and the altitude step $\Delta_{altitude}$. As soon as the UAV reaches

| Function name | Inputs | Stopp criteria |
|---|---|---|
| *climb_gamma* | $\gamma_{climb}$,$\Delta_{altitude}$, $\Delta_{time}$ | $UAV_{alt} >= Mission_{alt}$ |
| *cruise_distance* | $Target_{dist}$ $\Delta_{time}$ | $UAV_{dist} >= Target_{dist}$ |
| *cruise_capacity* | $Dash_{capaicty}$ $\Delta_{time}$ | $UAV_{cap} <= Dash_{cap}$ |

**Table 5.2:** Surveillance mission segment functions with the inputs and the termination criteria

| Geometry | | | Weights | | | Aerodynamics | | |
|---|---|---|---|---|---|---|---|---|
| Wingspan | 3.506 | [m] | Empty Mass | 16.34 | [kg] | $C_{Lcruise}$ | 0.65 | [-] |
| Wingarea | 0.9298 | [$m^2$] | Payload mass | 3.50 | [kg] | $C_{Lloiter}$ | 0.83 | [-] |

**Table 5.3:** Geometrical, weight and aerodynamical characteristics of the QT1 UAV

the operational altitude from table 5.1 the $climb\_gamma$ function is terminated and the dash segment starts. In this segment, the aircraft flight characteristics are defined with an even unaccelerated flight according to [102]. The target distance $Target_{dist}$ is besides the timestep the only input into the function and if it is exceeded by the covered distance $UAV_{dist}$ also terminates this segment. The loiter flight phase is defined in the *"cruise_capacity"* function and is based on the same flight mechanics than the dash phase. The aircraft attributes can be different between these two phases though (see section 5.2). The segment will be active as long as the input $Dash_{capaicty}$, representing the energy consumption in the dash-to-target phase, is smaller than the remaining energy level of the aircraft $UAV_{cap}$. The following two return-to-base segments are modeled with the *"cruise_distance"* and the *"climb_gamma"*, where the climb angle is now -5 to simulate descent. During the descent phase the energy consumption in the model is zero.

## 5.2 Aircraft Configuration

In order to carry out a performance analysis besides the mission profile also the employed aircraft needs to be defined. For this purpose, the *QT1* UAV developed at CfAR , presented in figure 5.1, will be employed in this work. The early phase of the project at CfAR justifies the approximation of the aircraft with key aspects. The most influential geometrical, weight and aerodynamical characteristics for the performance of the aircraft are summarized in table 5.3. To asses the climb segment sufficient enough the variation of the lift coefficient $C_L$ over the angle of attack $\alpha$ is modeled and presented in figure 5.2. The drag coefficient $C_D$ can then be computed depending on the lift coefficient $C_L$ with the relation visualized in figure 5.3. The drag coefficient influences the required thrust and therefore the necessary power output of the aircraft. The weight of the propulsion system is not included in the empty weight estimate and will be defined according to the propulsion system architecture in section 5.3. Besides this component all the characteristics are the same to guarantee comparability of the results.

**Figure 5.1:** CAD of QT1 UAV developed by CfAR

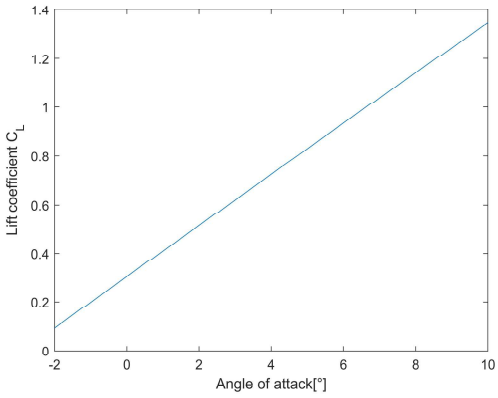


**Figure 5.2:** Lift coefficient $C_L$ versus the angle of attack $\alpha$ for the QT1 UAV

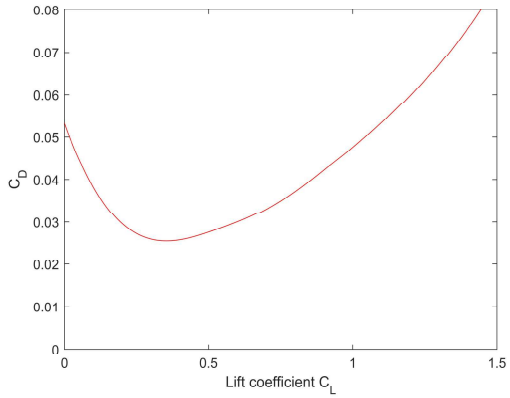


**Figure 5.3:** Drag coefficient $C_D$ versus the Lift coefficient $C_L$ for the QT1 UAV

| | | Electric | Gasoline | Hybrid |
|---|---|---|---|---|
| Fuel mass | [kg] | - | 3.4 | 1.4 |
| Battery capacity | [A.h] | 40 | - | 10 |
| Take-off weight | [kg] | $\sim 26$ | $\sim 26$ | $\sim 26$ |

**Table 5.4:** UAV configurations for the performance analysis

## 5.3 Performance Evaluation

In this section, the performance of the different propulsion system architectures is going to be evaluated with the aircraft characteristics from section 5.2 and the set mission profile. In total three propulsion system strategies for UAVs are going to be studied: the electric only, gasoline only and the hybrid structure.

The assessment of the results requires the definition of performance parameters. These parameters for the mission described in section 5.1 are going to be the maximum endurance (longest loiter time) for the baseline mission, maximum climb angle and the maximum dash distance with a predefined loiter time. The aircraft characteristics from section 5.2 are not including any propulsion system specifications. In order to provide comparability of the simulation results the Take-off weight of each type needs to be similar. Therefore, one configuration for each propulsion type is defined and presented in table 5.4. The hybrid version is going to evaluated twice according to the two energy management strategies developed in section 4.1.

First, the baseline mission is analysed in terms of maximum loiter time and maximum climb angle for the different propulsion system technologies. The climb angle has an insignificant ($<\approx 3\%$) impact on the loiter time for all propulsion systems as the length of the climb segment in comparison to the whole mission is low with a maximum value of 1% for the smallest climb angle of the *Electric* version. But the *Electric* UAV can not manage climb angles higher than 9.25° due to the insufficient maximum power output of the EM. While the gasoline and hybrid version can easily achieve climb angles up to 20°. At the start of the loiter time analysis , the optimal power request $P_{opt}$ of the hybrid propulsion system controller needs to be defined. First, this value is based on the mean power request during the *Electric* mission. In the mission analysis it is swept to find the $P_{opt}$ corresponding to the longest endurance for each hybrid configuration. The *Hybrid1* represents the classic, while the *Hybrid2* is the more sophisticated parallel hybrid propulsion system including a transmission as described in section 4.1. The results for the optimal power request sweep between 112 and 270 Watts are presented in the figures 5.4 and 5.5. The scattered data points of each configuration are fitted with a polynomial regression to obtain the optimal power request which provides the longest endurance. Therefore, a polynomial regression of the $3^{rd}$ and of the $5^{th}$ is chosen for the *Hybrid1* and *Hybrid2* configuration respectively. The *Hybrid1* has less variation in the loiter time results of the sweep parameter. But the quality of the fit is poor as presented by the low R-squared value. The fitting could be significantly improved with an optimization process

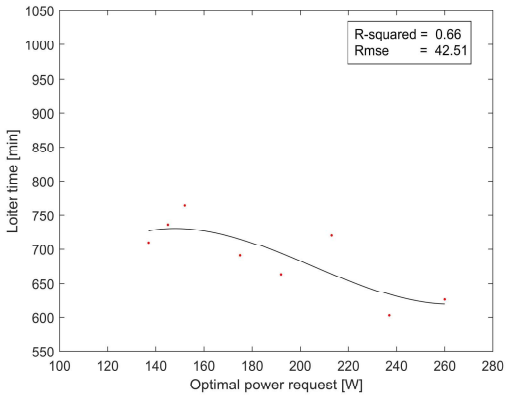


**Figure 5.4:** Loiter time of the *Hybrid1* system over the optimal power request $P_{opt}$ of the controller

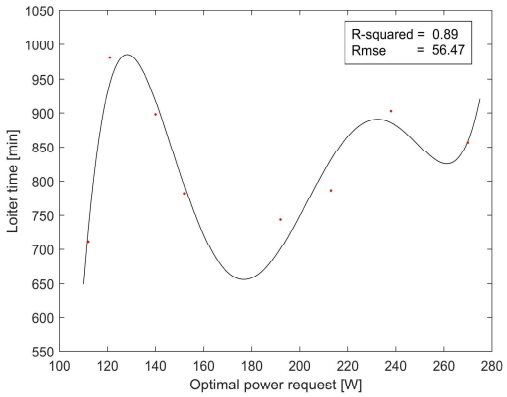


**Figure 5.5:** Loiter time of the *Hybrid2* system over the optimal power request $P_{opt}$ of the controller

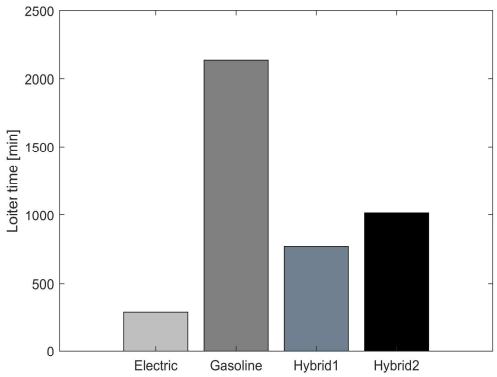


**Figure 5.6:** Maximum achievable loiter time in the baseline mission for each configuration

| Propulsion Configuration | Loiter time [min] |
|---|---|
| Electric | 287 |
| Gasoline | 2133 |
| Hybrid1 | 764 |
| Hybrid2 | 997 |

**Table 5.5:** Results of maximum loiter time analysis for baseline mission

focusing on the $P_{opt}$ parameter. Due to time limitations and the computation time of the complete mission analysis the current fit is deemed acceptable. Further research should though focus on this aspect. On the other hand, the *Hybrid2* configuration shows an acceptable fitting quality. The data points with a optimal power request of 152 (*Hybrid1*) and 121Watts (*Hybrid2*) are chosen as the controller variable for this mission.

At this stage, each propulsion system configuration is fully determined and the maximum endurance analysis can be performed. The maximum achievable loiter time for each configuration is presented in figure 5.6 and table 5.5. The *Electric* propulsion system achieves by the far the shortest loiter time with 287 minutes. This is only roughly 13% of the *Gasoline* version. The hybrid system employing the IOL strategy outperforms the classic version by $\approx 24\%$. This results represents 48% of the loiter compared with the *Gasoline* version with only 40% of the fuel mass. The trends of this analysis are continued in

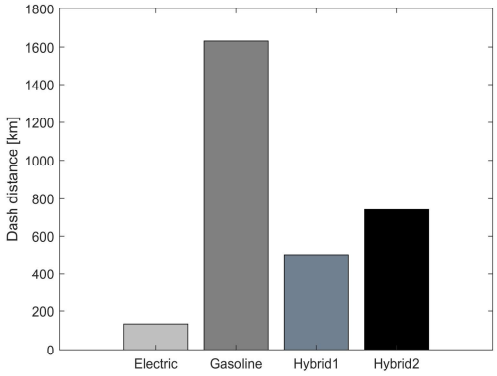


**Figure 5.7:** Maximum dash distance with a loiter time of 120min for each configuration

| Propulsion Configuration | Dash distance [km] |
|---|---|
| Electric | 132 |
| Gasoline | 1630 |
| Hybrid1 | 501 |
| Hybrid2 | 745 |

**Table 5.6:** Results of maximum dash distance analysis with 120min of loiter time

the maximum dash distance simulation presented in figure 5.7 and table 5.6. In this experiment, the loiter time is set with 120 minutes and the maximum target distance for each configuration should be obtained. The *Electric* has the lowest and the *Gasoline* configuration the highest range. The hybrid version employing the IOL strategy has great potential as the fuel mass reduction is relatively higher than the drop in operation range.

In the mission analysis, the main performance parameters, endurance and range characterizing a surveillance mission, are being tested for each propulsion system configuration. While the *Electric* version shows by far the smallest range and endurance it could still be employed for short endurance and small range intelligence gathering mission. This propulsion configurations has the big advantage of operating totally carbon emission free and with a substantial lower noise profile compared to the combustion version. Between the two *Hybrid* versions, the results show the higher performance of the parallel hybrid configuration using a transmission. The great advantage of the *Hybrid* propulsion systems is the possibility to operate the UAV in *Stealth* mode and to reduce the carbon footprint. The classic configuration could achieve better results if the smart controller outlined in sub-section 4.1.1 is implemented. Further, the optimization of both parallel hybrid configuration regarding the optimal power request $P_{opt}$ of the controller could further increase the performance. So far, the *Hybrid2* versions is a good alternative to the gasoline only version as the decrease in performance is smaller than the savings in fuel. The transmission of the configuration is only modeled with an efficiency,as no experimental results exist to validate a transmission model, an no weight penalty is included. Therefore, experiments on a parallel hybrid test bench including a transmission are necessary to increase the accuracy of the model. In [103] a possibly for the UAV applicable continuous variable transmission is developed with a weight of 610g. The performance impact of the transmission weight will be small as it only represents $\approx 2\%$ of the Take-off weight. To conclude, this analysis was carried out for a specific UAV the QT1 by

CfAR but to obtain the optimal fit between the aircraft characteristics and the propulsion system both specifications would need to be considered in a more broad mission analysis.

# 6

# Conclusion

## Contents

## 6.1 Achievments

In the aviation sector the demand and awareness for more economic and emission efficient vehicles is growing. In order to meet these goals public aeronautical agencies like NASA announced performance targets for future aerial vehicles. The aim of this thesis is the identification and exploration of promising concepts to meet these goals and achieve greener aviation.

The literature review conducted in Chapter $2$ presents various technologies and the associated challenges to lower emissions for aviation while providing better performance. Hybrid-electric propulsion, distributed propulsion and novel airframe configurations were identified as promising concepts for future aerial vehicles. The potential of the hybrid-electric propulsion system, the availability of experimental data and the possibility to implement the technology in the stepping stone platform such as an UAV lead to the choice of this technology to be explored in depth by the author. Therefore, a numerical model of the propulsion system was developed to investigate and compare, to conventional propulsion systems, the potential of the hybrid-electric concept in detail. Through the experimental results of a previous researcher it was possible to obtain and validate the propulsion model with high accuracy. The knowledge provided in this chapter could also be the starting point for further research in the field of green aviation with a different focus.

The numerical hybrid-electric propulsion model needs to include the standalone component models of the EM, ICE, propeller and battery. Because the model is validated with static experimental data the common Blade-Element-Momentum-Theory does not apply and a static propeller model is necessary. The model is based on the propeller thrust coefficient $C_T$ and therefore needs this discretization as an input. During the process the propeller was operated with the $C_T$ and power coefficient $C_P$ curves obtained from the experimental results as the employed propeller is unknown. This does not decrease the accuracy of the model since the curves can simply be exchanged accordingly. The EM was modeled through the widespread approach of an equivalent circuit. The two described models were validated with an EM-propeller test rig. In the evaluation of the models the lack of an ESC model and the approximation of the mechanical friction in the setup with an efficiency needs to be recognized. Considering these aspects the models present results of acceptable quality for the performance parameters (throttle, current, rpm and voltage). Due to the complexity of the combustion process and the focus of the thesis, the ICE model was established using the surrogate modeling technique. The necessary database for this approach is provided by the manufacturer. Radial Basis Function and Kriging models were investigated for the ICE. Even with the greater computation time the Kriging model provides results of higher quality and was therefore chosen to be implemented. The verification of the ICE model was performed on the manufacturer data as no other standalone measurements are available. The final surrogate achieves results with a maximum error varying between -12% and +13% for the according performance parameters BSFC and throttle prediction, which are directly linked to the power output and fuel flow of the engine.

These values are acceptable considering the complexity of the process.

The validation of the hybrid operational modes *EM only*, *ICE only*, *Dash* and *Regenerative Brake* in the frame of a parallel hybrid test bench was the next step. Therefore, the correct arrangement of the standalone models plus the test bench specific extra components, including the flywheel, the one-way bearing and the mechanical coupling (all modeled with simple efficiencies), are necessary. The correlations between the simulation and the experimental results show significant variations between the different operating strategies. The interaction between the power sources (EM and ICE) has a big influence on the simulation results. Already in the *EM only* mode even with a turned-off ICE this becomes obvious. The current prediction of the EM has a good trend and small relative errors for higher torque demands. In the hybrid test bench the EM is able to draw more current for the same throttle setting than in the EM-propeller test rig though and therefore the throttle is overestimated with a constant absolute error of $\approx 10\%$. In the *ICE only* operating mode the throttle prediction also has an constant absolute error, but this behaviour can be attributed to an adaptation of the throttle pin performed at CfAR. The simulation has a prediction error between 4% (high rotational speed) and 28% (low rotational speed) for the fuel flow of the ICE. Furthermore, the prediction trend is accurate until a rotational speed of $\approx 5700$ rpm, afterwards the behaviour of the simulation and experiment is different. The test environment (outside and inaccurate equipment) could induce measurements errors and explain the surrogate deviations. In the last two modes *Dash* and *Regenerative Brake* the two power sources influence each other the most. No fuel flow measurements for these operating strategies are available therefore only the current and throttle of the motor and the battery voltage are evaluated. The trend of the current prediction is not correct for the exponential regions (low and hight throttle values) but presents acceptable results otherwise. A satisfying throttle prediction of the EM for these operating strategies, even with several different approaches, was not obtained. The modeling of the battery voltage is considered of good quality as the trends of simulation and experimental results are in agreement. Since throttle is a surveillance parameter, it does not influence the performance of the UAV. The influential parameters show acceptable results, in the most likely operating regions, and therefore the model is considered to provide accurate results despite the above mentioned errors. Still further research effort should be conducted for these operating strategies.

After the validation of the test modes a standalone parallel hybrid propulsion module was developed. This module includes a propulsion controller and an energy management strategy. The controller introduces the optimal power request $P_{opt}$ as mode decision variable. This parameter should avoid constant acceleration/deceleration of the engine and save fuel. A sweep of $P_{opt}$ was performed to obtain the maximum performance of the propulsive system. While the classic parallel hybrid configuration includes no energy management strategy, for the sophisticated parallel hybrid (including an engine transmission) the IOL theory was implemented. The surrogate models provide the necessary data to obtain the IOL.

This complete propulsion module was then embedded into a research UAV by CfAR to compare the performance of different propulsion configurations in a mission analysis. Therefore, a surveillance mission, as similar UAV configurations are widely employed in these mission types, was designed. The key aircraft characteristics (e.g $C_L$ and $C_D$) were introduced and for each propulsion type one configuration with varying energy (fuel and capacity) levels, but with the same Take-off weight were defined. The performance parameters are the maximum achievable loiter and maximum dash distance. The conclusion of this analysis shows the potential of the sophisticated parallel hybrid configuration as it was possible to achieve 48% of the loiter compared to a conventional gasoline propulsion system with only 40% of the fuel. Furthermore, the sophisticated parallel configuration outperforms the classic parallel configuration by $\approx 24\%$. The maximum dash distance analysis presents the same trend.

## 6.2 Recommendations for future work

The author identified five areas as further research possibilities: additional experimental tests, the tuning of the parallel hybrid propulsion module, the implementation of a more sophisticated energy management strategy, performance analysis for various mission types and the formulation of a serial hybrid propulsion module.

The **additional experiment campaign** would provide data to increase the performance of various components simulations and is the base for the tuning of the models. The performance of the ICE surrogate could be significantly increased with a higher number and better distribution of design sites. In order to obtain these datapoints the ICE needs to be tested with a dynamometer. The EM model accuracy could be increased with a more dense efficiency curve mapping over the voltage level in a EM only test bench. So far these values are approximated due to the lack of data only with efficiency curves for 20V and 25V. Regarding the complete parallel hybrid test bench two additional test scenarios could improve the accuracy of the model. First strain measurement devices could be implemented into the test bench to record the mechanical friction. This could replace the mechanical efficiency approximation according to the literature. In the second approach more data points for the *Dash* and *Regenerative Brake* mode should be obtained. In a measurement series the throttle of the ICE needs to be kept at a constant value for various throttle positions (ICE throttle: 10%, 20%,..) while at the same time the EM throttle is swept from low to high values. First the torque variation of the engine, at constant throttle, over the change in rotational speed could be identified. Further, even more important, is the mapping of the interactions between the two power sources over a broad rpm range. Therefore, regions in which a certain component is operating inefficiently are identified more clearly. The controller then could avoid those operating

points and increase the overall efficiency of the propulsion system.

In the second research possibility the data out of the additional measurement series is employed to obtain models of higher quality and **tune the propulsion module**. Especially the accuracy in the exponential regions for the *Dash* and *Regenerative Brake* could be increased with the data from the extra tests on the hybrid test bench. The additional data could provide a relation between the throttle setting of the EM, the rotational speed of the system and the drawn current from the battery. Furthermore, a clutch model needs to be developed for the sophisticated parallel hybrid configuration. Due to the lack of experimental data so far a simple efficiency represents this component. An optimization process could be applied targeting the optimal power request $P_{opt}$ of the propulsion module. At the current state only a broad analysis of this parameter was conducted. An extensive in depth analysis could further increase the performance of the hybrid propulsion system.

The **energy management system** is the third area in which the author beliefs significant performance increases can be achieved. The developed IOL strategy was chosen, due to its reliability and already successful implementation, but in recent publications the potential of sophisticated control (fuzzy control in [95] [96]) approaches for the energy management system of hybrid propulsion system is proven. After inspecting the results of these studies the author suggests to target this energy management type for the UAV.

The **performance evaluation in a mission analysis** is another area for additional research possibilities. In this work only one mission type (surveillance) was analyzed, but a final assessment of the hybrid propulsion system capabilities is only possible if various mission profiles are analyzed. These extra simulations need to include scenarios with different focus like maximum achievable dash speed and multiply short climb segments (terrain following) for example.

The formulation of a simulation propulsion module for a **serial hybrid configuration** according to the structure presented in figure 2.1b is the last field the author outlines for further investigation. This module would need to include models for the EM, battery, ICE, generator and propeller. In serial configuration no interactions between the components exist and the control is less complex. Therefore, the implementation of the developed standalone models for the EM, the ICE, the propeller and the battery is possible. Only a simulation model for the generator and a propulsion system control needs to be developed. The implemented IOL energy management strategy could also be employed for this hybrid-electric configuration. The performance of the serial hybrid configuration will be significant different in the mission analysis compared to the parallel concept, due the higher weight penalty (generator). A great advantage could be the possibility to couple the concept with distributed propulsion.

# Bibliography


[1] J. Penner, D. Lister, D. Griggs, D. Dokken, and M. Mcfarland, "Summary for policymakers: Aviation and the global atmosphere," *A special report of IPCC Working: Published for the Intergovernmental Panel Climate Change*, 1999.

[2] J. Hupe, B. Ferrier, T. Thrasher, C. Mustapha, N. Dickson, T. Tanaka, P. Novelli, S. Brand, R. Sceponaviciute, S. Ananthanarayan *et al.*, "Icao environmental report: 2013 destination green-aviation and climate change," *ICAO Environmental Branch, Montreal, Canada*, 2013.

[3] S. H. L. Yim, G. L. Lee, I. H. Lee, F. Allroggen, A. Ashok, F. Caiazzo, S. D. Eastham, R. Malina, and S. R. H. Barrett, "Global, regional and local health impacts of civil aviation emissions," *Environmental Research Letters*, vol. 10, no. 3, p. 034001, feb 2015.

[4] C. A. Pope III, R. T. Burnett, M. J. Thun, E. E. Calle, D. Krewski, K. Ito, and G. D. Thurston, "Lung Cancer, Cardiopulmonary Mortality, and Long-term Exposure to Fine Particulate Air Pollution," *JAMA*, vol. 287, no. 9, pp. 1132–1141, 03 2002.

[5] C. A. P. III and D. W. Dockery, "Health effects of fine particulate air pollution: Lines that connect," *Journal of the Air & Waste Management Association*, vol. 56, no. 6, pp. 709–742, 2006.

[6] I. Economic, "Airline fuel and labour cost share," 2010, https://www.iata.org/whatwedo/Documents/economics/Airline_Labour_Cost_Share_Feb2010.pdf, Last accessed on 27.10.2019.

[7] NASA, "Aeronautics: Strategic Implementation Plan," Washington, DC, United States, Tech. Rep., 2017.

[8] AIRBUS, "Global market forecast: Cities, airports and aircraft 2019 - 2038," 2018, https://www.airbus.com/content/dam/corporate-topics/strategy/global-market-forecast/GMF-2019-2038-Airbus-Commercial-Aircraft-book.pdf, Last accessed on 27.10.2019.

[9] BOEING, "Boeing commercial market outlook 2019–2038," 2018, https://www.boeing.com/resources/boeingdotcom/commercial/market/commercial-market-outlook/assets/downloads/cmo-sept-2019-report-final.pdf, Last accessed on 27.10.2019.

[10] H. D. Kim, “Distributed propulsion vehicles,” in *27th Congress of the International Council of the Aeronautical Sciences*, Nice, France, 2010.

[11] R. Jansen, C. Bowman, A. Jankovsky, R. Dyson, and J. Felder, “Overview of nasa electrified aircraft propulsion (eap) research for large subsonic transports,” in *53rd AIAA/SAE/ASEE Joint Propulsion Conference*, Atlanta, GA, United States, 2017.

[12] J. Ausserer and F. Harmon, “Integration, validation, and testing of a hybrid-electric propulsion system for a small remotely piloted aircraft,” in *10th International Energy Conversion Engineering Conference*, Atlanta, GA, United States, 2012.

[13] D. Raymer, *Aircraft Design: A Conceptual Approach*, 6th ed. Washington, D.C., United States: American Institute of Aeronautics and Astronautics, Inc., 2018.

[14] C. E. Riboldi, “An optimal approach to the preliminary design of small hybrid-electric aircraft,” *Aerospace Science and Technology*, vol. 81, pp. 14 – 31, 2018.

[15] D. F. Finger, C. Braun, and C. Bil, “An initial sizing methodology for hybrid-electric light aircraft,” in *Aviation Technology, Integration, and Operations Conference*, Atlanta, GA, United States, 2018.

[16] J. Matlock, S. Warwick, P. Sharikov, J. Richards, and A. Suleman, “Evaluation of energy efficient propulsion technologies for unmanned aerial vehicles,” in *CSME International Congress*, Toronto, Canada, 2018.

[17] J. Hung and L. Gonzalez, “On parallel hybrid-electric propulsion system for unmanned aerial vehicles,” *Progress in Aerospace Sciences*, vol. 51, pp. 1 – 17, 2012.

[18] C. L. Bowman, J. L. Felder, and T. V. Marien, “Turbo- and hybrid-electrified aircraft propulsion concepts for commercial transport,” in *AIAA/IEEE Electric Aircraft Technologies Symposium (EATS)*, Cincinnati, OH, United States, 2018.

[19] A. B. Francisco, “Implementation of an ideal operating line control stratgey for hybrid electric vehicles,” Ph.D. dissertation, University of California, Davis, CA, United States, 2002.

[20] W. Lu, D. Zhang, J. Zhang, T. Li, and T. Hu, “Design and implementation of a gasoline-electric hybrid propulsion system for a micro triple tilt-rotor vtol uav,” in *6th Data Driven Control and Learning Systems (DDCLS)*, Chongqing, China, 2017.

[21] F. G. Harmon, A. A. Frank, and J.-J. Chattot, “Conceptual design and simulation of a small hybrid-electric unmanned aerial vehicle,” *Journal of Aircraft*, vol. 43, no. 5, pp. 1490–1498, 2006.

[22] U. of Colorado, “Hyperion, the hybrid propulsion bwb-uas,” 2018, https://www.uasvision.com/wp-content/uploads/2011/03/Hyperion.pdf, Last accessed on 27.10.2019.

[23] B. J. Brelje and J. R. Martins, "Electric, hybrid, and turboelectric fixed-wing aircraft: A review of concepts, models, and design approaches," *Progress in Aerospace Sciences*, vol. 104, pp. 1 – 19, 2019.

[24] L. Petricca, P. Ohlckers, and C. Grinde, "Micro-and nano-air vehicles: State of the art," *International journal of aerospace engineering*, vol. 2011, pp. 1–17, 2011.

[25] M. Harmats and D. Weihs, "Hybrid-propulsion high-altitude long-endurance remotely piloted vehicle," *Journal of Aircraft*, vol. 36, no. 2, pp. 321–331, 1999.

[26] D. Aircraft, "Diamond aircraft proudly presents the world's first serial hybrid electric aircraft da36 e-star," 2019, https://www.diamondaircraft.com/en/about-diamond/newsroom/news/article/diamond-aircraft-proudly-presents-the-worlds-first-serial-hybrid-electric-aircraft-da36-e-star/, Last accessed on 27.10.2019.

[27] B. Schiltgen, A. Gibson, M. Green, and J. Freeman, "More electric aircraft: Tube and wing hybrid electric distributed propulsion with superconducting and conventional electric machines," *SAE Technical Paper*, vol. 2013, pp. 01–23, 2013.

[28] J. L. Felder, "Nasa n3-x with turboelectric distributed propulsion," in *IMechE Disruptive Green Propulsion Technologies*, London, United Kingdom, 2014.

[29] M. K. Bradley and C. K. Droney, "Subsonic ultra green aircraft research phase ii: N+ 4 advanced concept development," BOEING, Tech. Rep., 2012.

[30] E. National Academies of Sciences, Medicine *et al.*, *Commercial aircraft propulsion and energy systems research: reducing global carbon emissions*, 1st ed. Washington, DC, United States: National Academies Press, 2016.

[31] T. Mahlia, T. Saktisahdan, A. Jannifar, M. Hasan, and H. Matseelar, "A review of available methods and development on energy storage; technology update," *Renewable and Sustainable Energy Reviews*, vol. 33, pp. 532–545, 2014.

[32] J. Sliwinski, A. Gardi, M. Marino, and R. Sabatini, "Hybrid-electric propulsion integration in unmanned aircraft," *Energy*, vol. 140, pp. 1407 – 1416, 2017.

[33] X.-Z. Gao, Z.-X. Hou, Z. Guo, and X.-Q. Chen, "Reviews of methods to extract and store energy for solar-powered aircraft," *Renewable and Sustainable Energy Reviews*, vol. 44, pp. 96–108, 2015.

[34] T. Mahlia, T. Saktisahdan, A. Jannifar, M. Hasan, and H. Matseelar, "A review of available methods and development on energy storage; technology update," *Renewable and Sustainable Energy Reviews*, vol. 33, pp. 532–545, 2014.

[35] G. Girishkumar, B. McCloskey, A. C. Luntz, S. Swanson, and W. Wilcke, "Lithium- air battery: promise and challenges," *The Journal of Physical Chemistry Letters*, vol. 1, no. 14, pp. 2193–2203, 2010.

[36] R. Jansen, C. Bowman, and A. Jankovsky, "Sizing power components of an electrically driven tail cone thruster and a range extender," in *16th AIAA Aviation Technology, Integration, and Operations Conference*, Washington, D.C., United States, 2016.

[37] S. Fletcher, M.-C. Flynn, C. E. Jones, and P. J. Norman, "Hybrid electric aircraft : state of the art and key electrical system challenges," *The Transportation Electrification eNewsletter*, vol. 2016, no. 9, 2016.

[38] SIEMENS, "Hybrid-electric propulsion," http://www.siemens.com/press/en/feature/2015/corporate/2015-03-electromotor.php?content%5b%5d=Corp, Last accessed on 27.10.2019.

[39] J. L. Felder, G. V. Brown, H. DaeKim, and J. Chu, "Turboelectric distributed propulsion in a hybrid wing body aircraft," in *20th International Society for Airbreathing Engines (ISABE)*, Gothenburg; Sweden, 2011.

[40] M. J. Armstrong, C. A. Ross, M. J. Blackwelder, and K. Rajashekara, "Propulsion system component considerations for nasa n3-x turboelectric distributed propulsion system," *SAE International Journal of Aerospace*, vol. 5, no. 2012-01-2165, pp. 344–353, 2012.

[41] J. Freeman, P. Osterkamp, M. Green, A. Gibson, and B. Schiltgen, "Challenges and opportunities for electric aircraft thermal management," *Aircraft Engineering and Aerospace Technology: An International Journal*, vol. 86, no. 6, pp. 519–524, 2014.

[42] F. Meredith, *Note on the Cooling of Aircraft Engines with special reference to Ethylene Glycol Radiators enclosed in Ducts*, 1st ed. London, United Kingdom: British ARC, 1936.

[43] M. Pellegrini and L. Piancastelli, "The bonus of aircraft piston engines, an update of the meredith effect," *International Journal of Heat and Technology*, vol. 25, pp. 51–56, 12 2007.

[44] A. Abdelkefi, "Aeroelastic energy harvesting: A review," *International Journal of Engineering Science*, vol. 100, pp. 112–135, 2016.

[45] J. Thauvin, G. Barraud, X. Roboam, B. Sareni, M. Budinger, and D. Leray, "Hybrid propulsion for regional aircraft: A comparative analysis based on energy efficiency," in *International Conference on Electrical Systems for Aircraft, Railway, Ship Propulsion and Road Vehicles & International Transportation Electrification Conference (ESARS-ITEC)*, Toulouse, France, 2016.

[46] M. Akbar and J. Curiel-Sosa, "Piezoelectric energy harvester composite under dynamic bending with implementation to aircraft wingbox structure," *Composite Structures*, vol. 153, pp. 193–203, 2016.

[47] A. Gohardani, G. Doulgeris, and R. Singh, "Challenges of future aircraft propulsion: A review of distributed propulsion technology and its potential application for the all electric commercial aircraft," *Progress in Aerospace Sciences*, vol. 47, no. 07, pp. 369–391, 2011.

[48] J. A. Schetz, S. Hosder, V. Dippold III, and J. Walker, "Propulsion and aerodynamic performance evaluation of jet-wing distributed propulsion," *Aerospace Science and Technology*, vol. 14, no. 1, pp. 1–10, 2010.

[49] T. Q. Dang and P. R. Bushnell, "Aerodynamics of cross-flow fans and their application to aircraft propulsion and flow control," *Progress in Aerospace Sciences*, vol. 45, no. 1-3, pp. 1–29, 2009.

[50] R. H. Liebeck, "Design of the blended wing body subsonic transport," *Journal of Aircraft*, vol. 41, no. 1, pp. 10–25, 2004.

[51] B. T. Schiltgen and J. Freeman, "Aeropropulsive interaction and thermal system integration within the eco-150: a turboelectric distributed propulsion airliner with conventional electric machines," in *16th AIAA Aviation Technology, Integration, and Operations Conference*, Washington, D.C., United States, 2016.

[52] A. M. Stoll, J. Bevirt, M. D. Moore, W. J. Fredericks, and N. K. Borer, "Drag reduction through distributed electric propulsion," in *14th AIAA Aviation Technology, Integration, and Operations Conference*, Atlanta, GA, United States, 2014.

[53] R. D. Falck, J. Chin, S. L. Schnulo, J. M. Burt, and J. S. Gray, "Trajectory optimization of electric aircraft subject to subsystem thermal constraints," in *18th AIAA/ISSMO Multidisciplinary Analysis and Optimization Conference*, Denver, CO, United States, 2017.

[54] K. J. Karimi, "Future aircraft power systems-integration challenges," BOEING, Tech. Rep., 2007.

[55] F. Berg, J. Palmer, P. Miller, M. Husband, and G. Dodds, "Hts electrical system for a distributed propulsion aircraft," *IEEE Transactions on Applied Superconductivity*, vol. 25, no. 3, pp. 1–5, 2015.

[56] P. Okonkwo and H. Smith, "Review of evolving trends in blended wing body aircraft design," *Progress in Aerospace Sciences*, vol. 82, pp. 1 – 23, 2016.

[57] F. Gern, A. Ko, B. Grossman, R. Haftka, R. Kapania, W. Mason, and J. Schetz, "Transport weight reduction through mdo: The strut-braced wing transonic transport," in *35th AIAA Fluid Dynamics Conference and Exhibit*, Toronto, Canada, 2005.

[58] K. B. Marty and K. D. Christopher, “Subsonic ultra green aircraft research: Phase i final report,” BOEING, Tech. Rep., 2011.

[59] A. Gong and D. Verstraete, “Fuel cell propulsion in small fixed-wing unmanned aerial vehicles: Current status and research needs,” *International Journal of Hydrogen Energy*, vol. 42, no. 33, pp. 21 311–21 333, 2017.

[60] N. S. Brun, “Preliminary design of a fuel cell-battery hybrid propulsion system for a small vtol uav,” Master’s thesis, University of Stavanger, Stavanger, Norway, 2018.

[61] O. Z. Sharaf and M. F. Orhan, “An overview of fuel cell technology: Fundamentals and applications,” *Renewable and Sustainable Energy Reviews*, vol. 32, pp. 810–853, 2014.

[62] J. Larminie, A. Dicks, and M. S. McDonald, *Fuel cell systems explained*, 2nd ed. Chichester, United Kingdom: J. Wiley, 2003.

[63] D. Verstraete, P. Hendrick, P. Pilidis, and K. Ramsden, “Hydrogen fuel tanks for subsonic transport aircraft,” *International journal of hydrogen energy*, vol. 35, no. 20, pp. 11 085–11 098, 2010.

[64] D. Verstraete, L. Cazzato, and G. Romeo, “Preliminary design of a fuel-cell-based hybrid-electrical uav,” in *28th Congress of the International Council of the Aeronautical Sciences*, Brisbane, Australia, 2012.

[65] L. Miguel Gonçalves Machado, “Design and development of a hybrid electric propulsion system for unmanned aerial vehicles,” Master’s thesis, Instituo Superior Tecnico Lisboa, Portugal, 2019.

[66] J. Matlock, S. Warwick, D. J. Richards, and D. A. Suleman, “Performance evaluation of a uav hybrid propulsion system,” CfAR, University of Victoria, Tech. Rep., 2019.

[67] T. C. Corke, *Design of aircraft*, 2nd ed. Englewood Cliffs, NJ, United States: Pearson, 2003.

[68] W. Khan and M. Nahon, “A propeller model for general forward flight conditions,” *International Journal of Intelligent Unmanned Systems*, vol. 3, no. 2, pp. 72–92, 2015.

[69] ACPPropellers, “Propeller performance database,” 2018, https://www.apcprop.com/technical-information/performance-data/, Last accessed on 27.10.2019.

[70] Mathworks, “Implement generic battery model,” 2018, https://www.mathworks.com/help/physmod/sps/powersys/ref/battery.html#bry4req-2, Last accessed on 27.10.2019.

[71] J.-W. Biermann, “Measurement system for cv joint efficiency,” *Journal of Passenger Cars*, vol. 2, pp. 1724–1730, 1999.

[72] L. Kumar and S. Jain, "Electric propulsion system for electric vehicular technology: A review," *Renewable and Sustainable Energy Reviews*, vol. 29, pp. 924–940, 2014.

[73] D. Lundström, K. Amadori, and P. Krus, "Validation of models for small scale electric propulsion systems," in *48th AIAA Aerospace Sciences Meeting Including the New Horizons Forum and Aerospace Exposition*, Orlando, FL, United States, 2010.

[74] M. MOTORS, "Axi 4130/20 gold line v2 technical specification," http://w3techs.com/technologies/overview/content_language/all, Last accessed on 27.10.2019.

[75] C. Green, "Modeling and test of the efficiency of electronic speed controllers for brushless dc motor," Master's thesis, California Polytechnic State University, San Luis Obispo, CA ,United States, 2015.

[76] G. P. Blair, *Design and simulation of two-stroke engines*, 1st ed. Warrendale, PA, United States: Society of Automotive Engineers, 1996.

[77] M. Turesson, "Modelling and simulation of a two-stroke engine," Master's thesis, University in Gothenburg, Gothenburg, Sweden, 2009.

[78] T. Bartz-Beielstein, B. Naujoks, J. Stork, and M. Zaefferer, "Tutorial on surrogate-assisted modelling," Synergy for Smart Multi-Objective Optimisation - HORIZON 2020, Tech. Rep., 2016.

[79] J. D. Martin and T. W. Simpson, "A study on the use of kriging models to approximate deterministic computer models," in *ASME International design engineering technical conferences and computers and information in engineering conference*, Chicago, IL, United States, 2003.

[80] S. N. Lophaven, H. B. Nielsen, J. Sondergaard, and A. Dace, "A matlab kriging toolbox," Technical University of Denmark, Tech. Rep., 2002.

[81] M. A. Bouhlel, N. Bartoli, A. Otsmane, and J. Morlier, "Improving kriging surrogates of high-dimensional design models by partial least squares dimension reduction," *Structural and Multidisciplinary Optimization*, vol. 53, no. 5, pp. 935–952, 2016.

[82] G. B. Wright, "Radial basis function interpolation: numerical and analytical developments," Ph.D. dissertation, University of Colorado, Boulder, CO, United States, 2003.

[83] G. Jekabsons, "Rbf: Radial basis function interpolation for matlab/octave," Riga Technical University, Tech. Rep., 2009.

[84] Z. Reitermanova, "Data splitting," in *Proceedings of the 19th Annual Conference of Doctoral Students*, Prague, Czech Republic, 2010.

[85] S. Geman, E. Bienenstock, and R. Doursat, "Neural networks and the bias/variance dilemma," *Neural computation*, vol. 4, no. 1, pp. 1–58, 1992.

[86] F. A. Viana, R. T. Haftka, and V. Steffen, "Multiple surrogates: how cross-validation errors can help us to obtain the best predictor," *Structural and Multidisciplinary Optimization*, vol. 39, no. 4, pp. 439–457, 2009.

[87] J. G. Bitterly, "Flywheel technology: past, present, and 21st century projections," *IEEE Aerospace and Electronic Systems Magazine*, vol. 13, no. 8, pp. 13–16, 1998.

[88] A. Slocum, "Fundamentals of design, bearings," 2018, https://web.mit.edu/2.75/fundamentals/FUNdaMENTALs%20Book%20pdf/FUNdaMENTALs%20Topic%2010.PDF, Last accessed on 27.10.2019.

[89] H. Wittel, D. Jannasch, J. Voßiek, and C. Spura, *Roloff/Matek Maschinenelemente*, 20th ed. Berlin, Germany: Springer, 2017.

[90] C. M. Greiser, "Implementation of a rule-based open-loop control strategy for a hybrid-electric propulsion system on a small rpa," Master's thesis, Air Force Institute of Technology, Wright-Patterson Air Force Base, OH, United States, 2011.

[91] SAE, "Engine power test code-spark ignition and compression ignition-net power rating," Tech. Rep., 1995.

[92] M. Cavcar, "The international standard atmosphere (isa)," Anadolu University, Tech. Rep., 2000.

[93] K. Chau and Y. Wong, "Overview of power management in hybrid electric vehicles," *Energy conversion and management*, vol. 43, no. 15, pp. 1953–1968, 2002.

[94] T. J. Wall and R. Meyer, "A survey of hybrid electric propulsion for aircraft," in *53rd AIAA/SAE/ASEE Joint Propulsion Conference*, Atlanta, GA, United States, 2017.

[95] Y. Xie, A. Savvaris, and A. Tsourdos, "Fuzzy logic based equivalent consumption optimization of a hybrid electric propulsion system for unmanned aerial vehicles," *Aerospace Science and Technology*, vol. 85, pp. 13–23, 2019.

[96] L. Ming, Y. Ying, L. Liang, L. Yao, and W. Zhou, "Energy management strategy of a plug-in parallel hybrid electric vehicle using fuzzy control," *Energy Procedia*, vol. 105, pp. 2660–2665, 2017.

[97] C.-C. Lin, H. Peng, J. W. Grizzle, and J.-M. Kang, "Power management strategy for a parallel hybrid electric truck," *IEEE transactions on control systems technology*, vol. 11, no. 6, pp. 839–849, 2003.

[98] M. Palman, B. Leizeronok, and B. Cukurel, "Mission Analysis and Operational Optimization of Adaptive Cycle Microturbofan Engine in Surveillance and Firefighting Scenarios," *Journal of Engineering for Gas Turbines and Power*, vol. 141, no. 1, 2018.

[99] M. Arjomandi, S. Agostino, M. Mammone, M. Nelson, and T. Zhou, "Classification of unmanned aerial vehicles," University of Adelaide, Tech. Rep., 2006.

[100] A. Puri, "A survey of unmanned aerial vehicles (uav) for traffic surveillance," University of South Florida, Tech. Rep., 2005.

[101] S. Herwitz, L. Johnson, S. Dunagan, R. Higgins, D. Sullivan, J. Zheng, B. Lobitz, J. Leung, B. Gallmeyer, M. Aoyagi *et al.*, "Imaging from an unmanned aerial vehicle: agricultural surveillance and decision support," *Computers and electronics in agriculture*, vol. 44, no. 1, pp. 49–61, 2004.

[102] J. Anderson, *Introduction to Flight*, 8th ed. New York, NY, United States: McGraw-Hill Education, 2015.

[103] D. Rockwood, N. Parks, and D. Garmire, "A continuously variable transmission for efficient urban transportation," *Sustainable Materials and Technologies*, vol. 1-2, pp. 36 – 41, 2014.

# A

# Simulation Files

Due to page limitations only the MATLAB files for the component models of the hybrid test bench (except the battery) the EM, the ICE and the propeller plus their connected sub-functions are presented.

**Listing A.1:** `PropModel.m`

```
function [rpm,Ct,Cp,time] = PropModel (ThrustReq, rho, diameter,threshold)
% This function predicts the rotational speed of the system based on CT - values
% of the propeller. The minimum and maximum RPM can be adjusted according
% to the operating conditions.

Thrust   = ThrustReq;
dia      = 0.0254*diameter;
error    = 100;
i = 1;
q = 1;
if Thrust == 0
```

```
12      rpm = 0;
13      Ct  = 0;
14      Cp  = 0;
15      return;
16  end
17  %% Stored CT and CP curves
18  load('CtRpmExp.mat')
19  load('CpRpmExp.mat')
20  %% LOOP
21  rpmMin = 500;
22  rpmMax = 10000;
23  rpmVector = rpmMin : 5 : rpmMax;
24  tic
25      while i <= length(rpmVector)
26          rpm = rpmVector(i);
27          Ct = CtRpm(rpm);
28          ThrustCheck = Ct * (rpm/60).^2 * dia.^4 *rho ;
29          error(i) = 1- abs(ThrustCheck/Thrust);
30          if error(i) <= 0.01
31                 time=toc;
32                 Ct = CtRpm(rpm);
33                 Cp = CpRpm(rpm);
34                 return;
35          end
36          i = i +1;
37      end
38      Ct = CtRpm(rpm);
39      Cp = CpRpm(rpm);
40      time = toc;
41  end
```

**Listing A.2:** `EMDatabase.m`

```
1  function [effEM] = EMdatabase(Tshaft,Voltage)
2  % This function determines the efficency of the EM based on the input
3  % torque and two efficicency maps provided by the manufacturer. These maps
4  % depend on the voltage input of the Motor.
5      if ~exist ('Voltage','var')
```

```
6           Voltage = 25.1;                                                 % Max
                voltage for 1st run
7       end
8   load('EffEM20.mat');
9   load('EffEM25.mat');
10
11  Tem = Tshaft;
12  effEm_25 = EM20V.eff(Tem);
13  effEm_20 = EM25V.eff(Tem);
14  V2 = 25.2;
15  V1 = 20;
16  if effEm_20 < effEm_25
17      effEM = (Voltage - V1)/(V2-V1) * (effEm_25 - effEm_20) + effEm_20;
18  else
19      effEM = (Voltage - V1)/(V2-V1) * (effEm_20 - effEm_25) + effEm_25;
20  end
21  end
```

**Listing A.3:** `ElectricPropulsionOnestep.m`

```
1   function [debugData, propulsionOutput, ChargePcntNew, noiseLevel,stopBit]...
2       = ElectricPropulsionOnestep(Thrust, Velocity, rho, ChargePcnt, timeStep,
            motorData, motorDataCSYS, propData, batteryData, payloadPower, state_0 ,
            Voltage,rpm, hybrid,TorqueReq,chargeMode,effMech)
3   % This function presents the  simulation model for the electric Motor
4
5   stopBit = 0;
6   %% RPM prediction
7   dia = diameterInches * 0.0254;
8   if ~exist('rpm','var')
9        [rpm,Ct,Cp] = propModel ( Thrust, rho, propDesign(1));
10       n = rpm / 60;
11  end
12  if Thrust == 0
13      Thrust == 0;
14  end
15  %% Throttle Prediction
16  % Intermediate Steps
```

```
n = rpm / 60;
dia = diameterInches * 0.0254;
    if ~exist('TorqueReq','var')
        if ~exist('Pprop','var')
            Pshaft      =   rho  * n.^3 * dia.^5 * Cp;
            wshaft      =   2*pi/60 * rpm;
            Tshaft      =   Pshaft / wshaft;
        else
            Pshaft      =   Pprop;
            wshaft      =   2*pi/60 * rpm;
            Tshaft      =   Pshaft / wshaft;
        end
    else
        Tshaft = TorqueReq;
        Pshaft = Tshaft * 2 * pi/60 * rpm;
    end

     if ~exist ('Voltage','var') || isempty(Voltage) == 1
         Voltage = 25.2;
     end
     if Voltage < 20
          VoltageRep  =  20;
          muEM        =   EMdatabase(Tshaft,VoltageRep);
     else
          muEM        =   EMdatabase(Tshaft,Voltage);
     end
Tem =   1/(effMech) * Tshaft;
if isnan(Tem)
    Tem = 0;
end
%% Original Solve
% INITIAL GUESS: [Vbattery, Ibattery, ThrottlePcnt]
x0 =[ Voltage , 0.1, 0.01];

if hybrid == 0
    function2minimize      =   @(x0)electricPropulsionEquationsPower(x0, Tem, rpm
        , KV, I0, Ra, ChargePcnt, cells_series, Capacity, timeStep,muEM);
    options                =   optimoptions('fsolve','Display','none','
```

```
        FunctionTolerance',1e-5);
    [x,fval,exitFlag]      =   fsolve( function2minimize, x0, options );
    % PostProcessing
    Vbattery               = x(1);
    Ibattery               = x(2);
    ThrottlePcnt           = x(3);
    Imotor                 = Ibattery*muEM;
elseif hybrid == 1
    if Tem == 0
        Imotor              = 0;
        Ibattery            = 0;
        ThrottlePcnt        = 0;
    else
        Imotor              = (Tem * ( KV * 2 *pi/60) + I0);
        maxEMTorque         = maxTorqueEM(rpm,Voltage);
        ThrottlePcnt        = Tem / maxEMTorque;
        if chargeMode == 0
            Ibattery        = Imotor/muEM;
        else
            Ibattery        = Imotor * muEM;
        end
    end
end
%% Postprocess
[Vbattery, ChargePcntNew, timeRemaining, ~ , ~, ~, ~] = batteryModel( Ibattery,
    ChargePcnt, Capacity, cells_series, timeStep,'batteryType', 'lipo');
estimatedEnd   = ChargePcntNew/100*Capacity/Ibattery*60;
%% Compute Propulsion Mass
MassMotor   = (3.726e+04*KV^(-0.7563)-31.58)/1000;
MassProp    = (diameterInches/20)^3*0.1859729;
MassEsc     = MassMotor/4;
MassBatt    = Vnominal*Capacity/179;
Mass        = MassMotor+MassProp+MassEsc+MassBatt;

%% PROPULSIONOUTPUT
noiseLevel  = 0;
propulsionOutput  = struct('Tem', Tem,'Tshaft',Tshaft,'Thrust', Thrust, '
    chargePcnt', ChargePcntNew, 'noiseLevel', noiseLevel,...
```

```
89      'rpm', rpm,'Throttle',  ThrottlePcnt,'Pshaft', Pshaft, 'Ppayload',
            payloadPower, ...
90      'Vbattery', Vbattery,'Ibattery', Ibattery,'Imotor',Imotor,'operatingMode',
            operatingMode,'EffEm',muEM, 'stopBit',stopBit,'CT',Ct,'CP',Cp,'
            PropulsionMassElectric',Mass);  %[rpm, Pabs, Pshaft, Ppaylaod, Pelectric,
             FF, Ibattery, etaProp, alternatorPower, hybridState]
91  debugData   = table(ThrottlePcnt, Thrust, Velocity, Vbattery, Ibattery, Pshaft,
        rpm, propName, Ct, Cp);
92  end
```

**Listing A.4:** ElectricPropulsionEquationsPower.m

```
1   function [error] = ElectricPropulsionEquationsPower(x0, Tem, rpm, KV, I0, Rm,
        ChargePcnt, cells_series, Capacity, timeStep)
2   % x0 is a guess at the state variable
3   %% System Equations to iterate
4   Vbattery        = x0(1);
5   Ibattery        = x0(2);
6   ThrottlePcnt    = x0(3);
7
8   [Vbattery_calc, ChargePcntNew, timeRemaining, ~ , ~, ~, ~] = batteryModel(
        Ibattery, ChargePcnt, Capacity, cells_series, timeStep,'batteryType', 'lipo')
        ;
9
10          error =[    Vbattery - Vbattery_calc;
11                      rpm - (Vbattery * ThrottlePcnt - Ibattery/ThrottlePcnt * Rm)*
                            KV;
12                      Tem - ((Ibattery *1/ ThrottlePcnt) - I0)/(KV*2*pi/60)];
13  end
```

**Listing A.5:** GasPropulsionOnetStep.m

```
1   function [debugData, propulsionOutput, fuelLoadPctNew, estimatedEnd, emissions,
        noiseLevel, stopBit] =...
2       GasPropulsionOnestep(obj,ThrustReq, Velocity, rho, fuelLoadPcnt, timeStep,
            motorData, motorDataCSYS, propData,...
3       fuelMassStart, payloadPower,rpm, TorqueReq)
4   % This function presents the simulation model for the 2
```

```
5
6  FuelRemaining = fuelMassStart * (fuelLoadPcnt/100);
7  %% ============ Main propeller and engine calculations =====================
8  if strcmp(obj.IOLStrategy, 'on')
9      % do nothing
10 elseif ~exist('rpm','var') | ~exist('Ct','var') | ~exist('Cp','var')
11     [rpm,Ct,Cp] = propModel ( ThrustReq, rho, propDesign(1));
12 end
13 n = rpm / 60;
14 dia = diameterInches * 0.0254;
15 %% Intermediate calculations
16 if ~exist('TorqueReq','var')
17     Pprop         =   rho  * n.^3 * dia.^5 * Cp;
18     PshaftICE     =   Pprop * 1/(mechEff);
19 else
20     TshaftICE     = TorqueReq * 1/(mechEff);                          % Torque @
           ICE
21     PshaftICE     = TshaftICE * 2 * pi /60* rpm;                              %
          Power @ ICE
22 end
23
24 % Computed power needs to be convertered into RAW power
25 % Enviromental Inputs ( Sea level conditions )
26 altitude = obj.altitude;
                                                                    % cfar alitude
27 T = 288.15 - 0.0065 * altitude; %[K]
28 P = 101325 * ( 1- ( 0.0065 * altitude / 288.15)) .^ 5.25588 * 10^-2; %[mb]
29 Cf = 1.180 * [ 990 / P * (( T )/ 298)^0.5] - 0.180;
30 PowerRaw = PshaftICE / Cf;
31
32 %% THROTTLE determination
33 % DataPreperation
34 dataCleanP = motorData.power;
35 nbtrainP   = length(dataCleanP)-1;
36 nbtestP    = 1;
37 rows       = randperm(length(dataCleanP));
38 dataTrainP = dataCleanP(rows(1:nbtrainP),:);
39 dataTestP  = dataCleanP(rows(nbtrainP+1:length(dataCleanP)),:);
```

```
40
41 % Initalization of the iterative process
42 ThrottleVector       =  20 : 0.5 : 100;
43 i                    =  1;
44 Error                =  20;
45 NoPoints             =  round(length(dataTrainP)/2);
46 [TrainError, dmodel] =  CreatePowerModel(dataTrainP, NoPoints);
47
48 while i < length(ThrottleVector)
49     Throttle    = ThrottleVector(i);
50     PowerPre(i) = PowerPrediction(dmodel,Throttle,rpm);
51     Error(i)    = abs(PowerRaw-PowerPre(i));
52     i = i +1;
53 end
54 [MinErrorThrottle, IndexMinError]   = min(Error);
55 Power                              = PowerPre(IndexMinError) *Cf;
56 Tshaft                              = Power / (2*pi/60*rpm);
57 Pprop                               = Power * mechEff;
58 Tprop                               = Tshaft * mechEff;
59 ThrottlePcnt                        = ThrottleVector(IndexMinError);
60 %% BSFC determination
61 dataCleanB  = motorData.bsfc;
62 nbtest      = 1;
63 nbtrainB    = length(dataCleanB)-1;
64 rows        = randperm(length(dataCleanB));
65 dataTrainB  = dataCleanB(rows(1:nbtrainB),:);
66 dataTestB   = dataCleanB(rows(nbtrainB+1:length(dataCleanB)),:);
67 NoPoints               = round(length(dataTrainB)/2);
68 [TrainErrorB, dmodelB] = CreateBSFCModel(dataTrainB, NoPoints);
69 BSFCPre                = BSFCPrediction(dmodelB,ThrottlePcnt,rpm);
70 %% Computation Check
71 if ThrottlePcnt > 100
72     disp('Error in Power Surrogate!')
73 elseif ThrottlePcnt < 20
74     disp('WARNING ! In this Region the accuarcy of the Surrogate is not
         guarenteed')
75 elseif rpm < 2000
76     disp('WARNING ! In this Region the accuarcy of the Surrogate is not
```

```
        guarenteed')
77  end
78  end
79  %% FF  DETERMINATION
80  FF = BSFCPre * Power/1000/3600; %[g/s]
81  fuelLoadPctNew = (abs(FuelRemaining) - FF/1000 * timeStep)/fuelMassStart*100;
82  if fuelLoadPctNew < 0
83      stopBit = 1;
84      disp('The UAV is out of fuel')
85  end
86  endurance    = FuelRemaining/FF;
87  %% Mass Calculations
88  engineWOT_P   = max(motorData.power(:,3));
89  MassMotor     = (engineWOT_P+74.603)/1.0072/1000;
90  MassProp      = (diameterInches/20)^3*0.1859729;
91  [MassFuelTank, ~] = fuelTank_Calculator(fuelMassStart);
92  MassBckBatt   = 0;
93  Mass          = MassMotor+MassProp+MassFuelTank+MassBckBatt;
94  %% Calculate Forces and Mass Properties
95  noiseLevel    = 0;
96  estimatedEnd = endurance;
97  debugData = table(ThrustReq, endurance, Power, BSFCPre, FF, rpm, ThrottlePcnt);
98  propulsionOutput = struct('Thrust', ThrustReq,'BSFC',BSFCPre,'fuelMassStart',
        fuelMassStart,'fuelLoadPcnt', fuelLoadPctNew,'estimatedEnd', estimatedEnd,...
99      'emissions', emissions, 'noiseLevel', noiseLevel,'rpm', rpm,'throttle',
            ThrottlePcnt, 'Pshaft', Power,'Pprop',Pprop,'TorqueProp',Tprop,'TorqueICE
            ',Tshaft,...
100     'FuelFlow', FF, 'operatingMode', operatingMode,'PropulsionMassGasoline',Mass,
             'stopBit',stopBit);
101 end
```

**Listing A.6:** `CreatePowerModel.m`

```
1   function [TrainError,dmodel]= CreatePowerModel(dataTrain, NoPoints)
2   % The function creates the power surrogate model for the input data and
3   % also returns the final train error.
4   for i = 1:NoPoints
5   rng(10)
```

```
[CvTrain(:,i), CvTest(:,i)] = crossvalind('LeaveMOut',NoPoints,5);
Ptrain = dataTrain(CvTrain(:,i),:);
Ptest  = dataTrain(CvTest(:,i),:);
%% DEFINE OPTIONS
%Starting point
theta = [10;10];
% Boundary limits
lob = [0.1 0.1];
upb = [100;20];
%% CREATION OF THE MODEL
[dmodel(i), perf] = dacefit(Ptrain(:,[1 , 2]), Ptrain(:,3),@regpoly1, @correxp,
    theta, lob, upb);
X = gridsamp([2500 24.9 ; 7000 40], 50);
% Prediction function
[YX MSE]=predictor(X, dmodel(i));
X1 = reshape(X(:,1), 50,50);
X2 = reshape(X(:,2), 50,50);
YX = reshape(YX, size(X1));
[PowerPre , dy] = predictor(Ptest(:,[1 2]), dmodel(i));
    for g = 1 : length(PowerPre)
            RelError(i,g)= (1-(PowerPre(g)/Ptest(g,3)))*100;
    end
score(i) = abs(min(RelError(i,:)))+max(RelError(i,:));
end
[TrainErrorFinal, IndexFinal] = min(score);
% Final Check
TrainIndexFinal = CvTrain(:,IndexFinal);
TrainDataFinal  = dataTrain(TrainIndexFinal,:);
TrainError      = RelError(IndexFinal,:);
theta = [10;10];
% Boundary limits
lob = [0.1 0.1];
upb = [100;20];
%% CREATION OF THE MODEL
[dmodel, perf] = dacefit(TrainDataFinal(:,[1 , 2]), TrainDataFinal(:,3),@regpoly1
    , @correxp, theta, lob, upb);
end
```

**Listing A.7:** PowerPrediction.m

```
function [PowerPre]=PowerPrediction(dmodel,Throttle, Rpm)
% This function gets the datapoint and the already built model to predict
% the Power
dataTest = [Rpm, Throttle];
[PowerPre , dy] = predictor(dataTest(:,[1 2]), dmodel);
end
```

**Listing A.8:** IOLEngineInterpolation.m

```
function [rpmEngine,TorqueEngine,PowerEngine,BSFCEngine] = IOLEngineInterpolation
    (powerRequest,mechEff)
% This function uses the power request by the engine obtain the ideal operating
    point. The Function uses interpolation  rather than a fit of the scattered
    data due to their distribution.
load('IOLData.mat')            % stored IOL data points
[rows, columns] = size(Data);
powerRequest = 1/(mechEff) * powerRequest;
for i = 1 : rows
    if powerRequest < Data(i,3)
        Point2    = Data(i,:);
        Point1    = Data((i-1),:);
        break;
    end
end
x1 = Point1(1,1);
x2 = Point2(1,1);
y1 = Point1(1,2);
y2 = Point2(1,2);
coeff = polyfit([x1, x2], [y1, y2], 1);
if x1 > x2
    rpmVector           = x2 : 5 : x1;
else
    rpmVector           = x1 : 5 : x2;
end
error = 1;
for i = 1 : length(rpmVector)
    rpm(i)    = rpmVector(i);
```

```
    torque(i) = coeff(1)*rpm(i)+coeff(2);
    power(i)  = torque(i) * (2*pi/60*rpm(i));
    error(i) = abs(1-power(i)/powerRequest);
    if powerRequest > 20
        threshold = 0.05;
    else
        threshold = 0.07;
    end
    if error(i) < threshold
        x3 = rpm(i);
        y3 = torque(i);
        Point3 = [x3,y3];
        break;
    end
end
distTotal = sqrt((Point2(1,1)-Point1(1,1)).^2+((Point2(1,2)-Point1(1,2)).^2));
distPart  = sqrt((Point3(1,1)-Point1(1,1)).^2+((Point3(1,2)-Point1(1,2)).^2));
Percent    = distPart/distTotal;
    if Point2(1,3) > Point1(1,3)
        Power3 = Percent * (Point2(1,3) - Point1(1,3)) + Point1(1,3);
    else
        Power3 = Percent * (Point1(1,3) - Point2(1,3)) + Point2(1,3);
    end
    if Point2(1,4) > Point1(1,4)
        BSFC3 = Percent * (Point2(1,4) - Point1(1,4)) + Point1(1,4);
    elseif Point2(1,4) == Point1(1,4)
        BSFC3 = Point2(1,4); % In case the points are on the same BSFC contour
    else
        BSFC3 = Percent * (Point1(1,4) - Point2(1,4)) + Point2(1,4);
    end
Point3          =[x3,y3,Power3,BSFC3];
rpmEngine       = Point3(1,1);
TorqueEngine    = Point3(1,2);
PowerEngine     = Point3(1,3);
BSFCEngine      = Point3(1,4);
end
```

# B

# Appendix B

## B.1 Theoretical Information

| Organization | Aircraft | Time Frame | Electric Architecture | Components | Component Performance |
|---|---|---|---|---|---|
| BOEING SUGAR | Single-aisle | N+3 | Parallel Hybrid | Motor | 3-5kW/kg |
| | | | | Battery | 750 kW/kg |
| NASA N3X | Twin-aisle | N+3 | Turboelectric | Generator | $> 10kW/kg$ @ 98% efficiency |
| | | | | Motor | 4MW |
| ESAero | Single-aisle | N+2 | Turboelectric | Generator | 8kW/kg |
| | | | | Motor | 4.5Mw/kg |
| Airbus | General aviation | N+1 | All-electric | Batteries | 250-400 Wh/kg |
| | | | Hybrid | Motor, Generator | Not specified |
| Cambridge | General aviation | N+1 | Parallel Hybrid | Batteries | 150 - 750 kW/kg |
| Georgia Tech | Single-aisle | N+3 | Parallel Hybrid | Motor | 3-5kW/kg |
| | | | | Batteries | 750kW/kg |

**Table B.1:** System Studies of Aircraft with Electric Propulsion adapted from [30]

| |
|---|
| • Complex flight control architecture and allocation, with sever hydraulic requirements |
| • Large auxiliary power requirements |
| • New class of engine installation |
| • Flight behavior beyond stall |
| • High floor angle on take off and approach to landing |
| • Acceptance by the flying public |
| • Performance at long range |
| • Experience and data base for new class of configuration limited to military aircraft |

**Table B.2:** Issues and areas of risk of BWB designs

## B.2 Manufacturer Data

Raw Power[W]

| Throttle\RPM | 1000 | 2000 | 2500 | 3000 | 3500 | 4000 | 4500 | 5000 | 5500 | 6000 | 6500 | 7000 | 8000 |
|---|---|---|---|---|---|---|---|---|---|---|---|---|---|
| 0 | #N/A | #N/A | #N/A | #N/A | #N/A | #N/A | #N/A | #N/A | #N/A | #N/A | #N/A | #N/A | #N/A |
| 4.7 | #N/A | #N/A | #N/A | #N/A | #N/A | #N/A | #N/A | #N/A | #N/A | #N/A | #N/A | #N/A | #N/A |
| 9.8 | #N/A | -8 | #N/A | #N/A | #N/A | #N/A | #N/A | #N/A | #N/A | #N/A | #N/A | #N/A | #N/A |
| 14.9 | #N/A | #N/A | 32 | -20 | 48 | 69 | 83 | 90 | 76 | 71 | 73 | 0 | #N/A |
| 20 | #N/A | #N/A | 102 | 178 | 162 | 196 | 251 | 300 | 341 | 352 | 350 | #N/A | #N/A |
| 24.9 | #N/A | #N/A | 268 | 328 | 384 | 372 | 435 | 517 | 593 | 648 | 654 | #N/A | #N/A |
| 29.8 | #N/A | #N/A | 404 | 499 | 566 | 617 | 669 | 770 | 836 | 812 | 878 | 881 | 928 |
| 34.9 | #N/A | #N/A | 460 | 575 | 673 | 780 | 912 | 1025 | 1145 | 1132 | 1172 | 1267 | 1224 |
| 40 | #N/A | #N/A | 485 | 622 | 736 | 862 | 1040 | 1166 | 1304 | 1341 | 1429 | 1513 | 1565 |
| 49.8 | #N/A | #N/A | 529 | 681 | 821 | 972 | 1209 | 1347 | 1514 | 1592 | 1714 | 1823 | 1984 |
| 59.6 | #N/A | #N/A | 549 | 708 | 855 | 1039 | 1291 | 1461 | 1604 | 1695 | 1844 | 1988 | 2166 |

**Table B.3:** raw power of DA35, provided by manufacturer, depending on throttle and rpm setting

BSFC[g/kW-hr]

| Throttle\RPM | 1000 | 2000 | 2500 | 3000 | 3500 | 4000 | 4500 | 5000 | 5500 | 6000 | 6500 | 7000 | 8000 |
|---|---|---|---|---|---|---|---|---|---|---|---|---|---|
| 0 | #N/A | #N/A | #N/A | #N/A | #N/A | #N/A | #N/A | #N/A | #N/A | #N/A | #N/A | #N/A | #N/A |
| 4.7 | #N/A | #N/A | #N/A | #N/A | #N/A | #N/A | #N/A | #N/A | #N/A | #N/A | #N/A | #N/A | #N/A |
| 9.8 | #N/A | #N/A | #N/A | #N/A | #N/A | #N/A | #N/A | #N/A | #N/A | #N/A | #N/A | #N/A | #N/A |
| 14.9 | #N/A | #N/A | #N/A | #N/A | #N/A | 2351 | 2208 | 1907 | 2677 | 2664 | 2933 | #N/A | #N/A |
| 20 | #N/A | #N/A | 1606 | 1138 | 1287 | 1109 | 1022 | 830 | 835 | 800 | 767 | #N/A | #N/A |
| 24.9 | #N/A | #N/A | 843 | 703 | 696 | 648 | 735 | 633 | 595 | 586 | 592 | #N/A | #N/A |
| 29.8 | #N/A | #N/A | 667 | 564 | 536 | 523 | 523 | 504 | 486 | 521 | 501 | 540 | 539 |
| 34.9 | #N/A | #N/A | 669 | 552 | 530 | 498 | 453 | 452 | 457 | 474 | 453 | 472 | 563 |
| 40 | #N/A | #N/A | 717 | 626 | 544 | 504 | 452 | 453 | 459 | 460 | 465 | 468 | 476 |
| 49.8 | #N/A | #N/A | 762 | 639 | 607 | 540 | 485 | 465 | 503 | 525 | 494 | 483 | 481 |
| 59.6 | #N/A | #N/A | 749 | 662 | 656 | 676 | 524 | 509 | 522 | 534 | 514 | 515 | 517 |
| 80 | #N/A | #N/A | 834 | 705 | 655 | 704 | 598 | 578 | 540 | 571 | 565 | 563 | 576 |
| 100 | #N/A | #N/A | 815 | 805 | 702 | 649 | 625 | 607 | 597 | 635 | 620 | 619 | 634 |

**Table B.4:** BSFC of DA35, provided by manufacturer, depending on throttle and rpm setting

## B.3 Experimental Results

| Throttle [%] | RPM | Torque [Nm] | Current ESC [A] | Current EM [A] | Voltage [V] |
|---|---|---|---|---|---|
| 10 | 753.67 | 0.032 | - | 0.29 | 25.14 |
| 15 | 1062.20 | 0.062 | - | 0.56 | 25.13 |
| 20 | 1352.40 | 0.10 | - | 0.96 | 25.12 |
| 25 | 1666.90 | 0.14 | - | 1.57 | 25.09 |
| 30 | 1981.80 | 0.20 | - | 2.40 | 25.05 |
| 35 | 2295.30 | 0.27 | 0.03 | 3.52 | 25.00 |
| 40 | 2595.50 | 0.35 | 7.61 | 4.90 | 24.94 |
| 45 | 2884.80 | 0.43 | 9.84 | 6.59 | 24.86 |
| 50 | 3163.00 | 0.52 | 12.31 | 8.61 | 24.76 |
| 60 | 3686.70 | 0.70 | 18.99 | 13.56 | 24.55 |
| 65 | 3925.50 | 0.80 | 22.96 | 16.51 | 24.37 |
| 70 | 4151.90 | 0.90 | 27.13 | 19.71 | 24.18 |
| 75 | 4361.40 | 0.99 | 31.96 | 23.14 | 23.97 |
| 80 | 4581.70 | 1.09 | 37.44 | 27.29 | 23.72 |
| 85 | 4773.50 | 1.19 | 43.08 | 31.53 | 23.43 |
| 90 | 4943.10 | 1.28 | 49.04 | 35.84 | 23.11 |
| 95 | 5090.10 | 1.36 | 54.70 | 40.17 | 22.79 |
| 100 | 5169.50 | 1.40 | 56.53 | 42.73 | 22.50 |

**Table B.5:** Experimental results of propeller test rig with EM [65]

| Throttle | Rpm | $Torque_{prop}$ | Current | Voltage |
|---|---|---|---|---|
| 10% | 1077.49 | 0.06 | 0.86 | 25.10 |
| 15% | 1637.59 | 0.14 | 2.00 | 25.04 |
| 20% | 2079.91 | 0.23 | 3.46 | 24.97 |
| 25% | 2481.82 | 0.32 | 5.26 | 24.87 |
| 30% | 2794.67 | 0.41 | 7.24 | 24.77 |
| 35% | 3033.01 | 0.48 | 9.17 | 24.67 |
| 40% | 3296.13 | 0.57 | 11.46 | 24.54 |
| 45% | 3531.59 | 0.65 | 14.11 | 24.40 |
| 50% | 3774.49 | 0.74 | 17.09 | 24.24 |
| 55% | 3979.33 | 0.82 | 20.14 | 24.07 |
| 60% | 4168.70 | 0.90 | 23.54 | 23.87 |
| 65% | 4317.67 | 0.97 | 26.47 | 23.69 |
| 70% | 4485.51 | 1.04 | 29.89 | 23.49 |
| 75% | 4656.80 | 1.12 | 34.09 | 23.26 |
| 80% | 4672.87 | 1.13 | 34.52 | 23.17 |
| 85% | 4679.33 | 1.13 | 34.82 | 23.12 |
| 90% | 4794.72 | 1.19 | 37.76 | 22.97 |

**Table B.6:** Experimental results of the EM only mode for the parallel Hybrid Test Bench [65]

| Throttle | Rpm | Fuel Flow [g/hr] | Power [W] |
|---|---|---|---|
| 15 | 4543 | 304.4 | 531 |
| 20 | 5415 | 630.2 | 894 |
| 25 | 5781 | 742.5 | 1085 |
| 30 | 6115 | 791.1 | 1281 |
| 35 | 6319 | 820.3 | 1412 |
| 40 | 6503 | 1024.6 | 1537 |

**Table B.7:** Averaged results over 10 minutes performed at CfAR with the DA35 engine in the Hybrid Test Bench setup

| Throttle ICE | Throttle EM | Rpm | Torque$_{prop}[Nm]$ | Current [A] | Voltage$_{Bat}[V]$ |
|---|---|---|---|---|---|
| 40% | 0% | 4625 | 1.13 | -0.0026 | 24.93 |
| | 10% | 4661 | 1.13 | 2.93 | 24.84 |
| | 20% | 4815 | 1.20 | 7.26 | 24.68 |
| | 30% | 5151 | 1.37 | 12.55 | 24.44 |
| | 40% | 5568 | 1.60 | 17.48 | 24.19 |
| | 50% | 5728 | 1.70 | 19.87 | 24.03 |
| | 60% | 5741 | 1.71 | 19.06 | 24.00 |

**Table B.8:** Experimental results for the *Dash* mode of parallel hybrid Test Bench [65]

| Throttle ICE | Throttle EM | Rpm | Torque$_{prop}[Nm]$ | Current [A] | Voltage$_{Bat}[V]$ |
|---|---|---|---|---|---|
| 60% | 0% | 6629.834 | 2.27 | -0.003 | 24.17 |
| | -10% | 6666.666 | 2.29 | -0.91 | 24.18 |
| | -20% | 6629.834 | 2.25 | -2.49 | 24.25 |
| | -30% | 6575.391 | 2.23 | -4.33 | 24.31 |
| | -40% | 6451.612 | 2.15 | -6.56 | 24.40 |
| | -50% | 6315.789 | 2.06 | -8.45 | 24.48 |
| | -60% | 6217.616 | 1.99 | -9.43 | 24.54 |
| | -70% | 5769.23 | 1.72 | -10.55 | 24.60 |
| | -80% | 5581.395 | 1.61 | -11.71 | 24.67 |
| | -90% | 5555.555 | 1.60 | -12.84 | 24.74 |

**Table B.9:** Experimental results for the *Regenerative Brake* mode of parallel hybrid Test Bench [65]

## B.4 Simulation Results

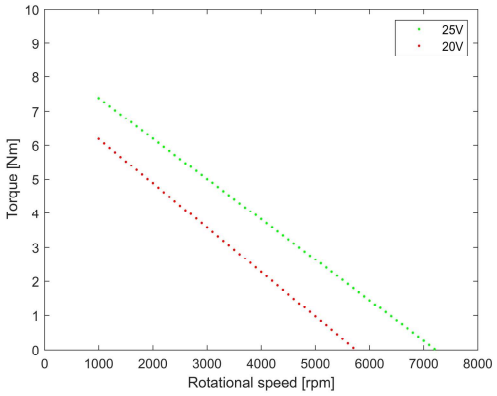


**Figure B.1:** Maximum torque of the EM depending on rotational speed and voltage level

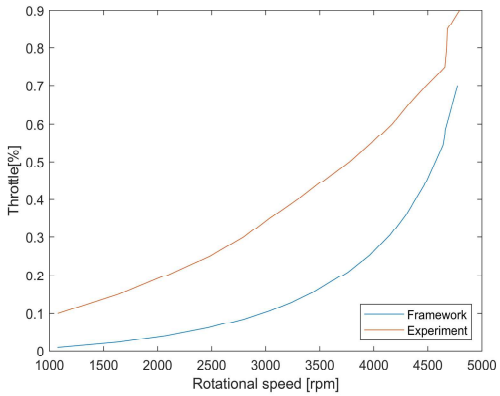


**Figure B.2:** Throttle setting of the EM, according to the *max torque* method, over the rotational speed for the *EM only* mode